The Dissertation Committee for Aya Ishihara
certifies that this is the approved version of the following dissertation:

Large-Scale Two-Particle Correlation Structures in Au-Au Collisions at $\sqrt{s_{NN}} = 130$ GeV

Committee:

Gerald W. Hoffmann, Supervisor

C. Fred Moore, Supervisor

Robert L. Ray

Thomas A. Trainor

Takeshi Udagawa

Klaus R. Bichteler

Large-Scale Two-Particle Correlation Structures in Au-Au Collisions at $\sqrt{s_{NN}} = 130$ GeV

by

Aya Ishihara, B.S.

DISSERTATION

Presented to the Faculty of the Graduate School of

The University of Texas at Austin

in Partial Fulfillment

of the Requirements

for the Degree of

DOCTOR OF PHILOSOPHY

THE UNIVERSITY OF TEXAS AT AUSTIN

May 2004

To my family and friends

Large-Scale Two-Particle Correlation Structures in Au-Au Collisions at $\sqrt{s_{NN}} = 130$ GeV

Publication No. ____________________

Aya Ishihara, Ph.D.
The University of Texas at Austin, 2004

Supervisors: Gerald W. Hoffmann
C. Fred Moore

The first measurements of surviving correlation structures in the final-state charged hadron distributions produced in collisions of gold nuclei at $\sqrt{s_{NN}}$ = 130 GeV are presented. An abundance of correlation structures reflecting relativistic heavy ion collision dynamics is observed over a large momentum acceptance, transverse momentum range $0.15 \leq p_t \leq 2.0$ GeV/c, pseudorapidity range $-1.3 \leq \eta \leq 1.3$ and full azimuth angle $-\pi \leq \phi \leq \pi$ among primary hadrons measured by the STAR detector at the Relativistic Heavy Ion Collider (RHIC). Correlation structures are measured by means of two-particle number-density ratios in transverse and axial momentum spaces. Isoscalar and isovector correlations are studied separately by examining pair-charge dependent (CD) and independent (CI) correlation components. Observed correlation structures are consistent with the picture that particle production from color-string fragmentation and fragmentation of partons from initial state parton

scattering in p-p collisions is strongly modified by a dissipative color medium created in central heavy ion collisions.

Table of Contents

List of Tables

List of Figures

Chapter 1

Introduction

The properties of matter which we see even in everyday life have provided us important information about how our world is constructed. However, studies also showed us that our knowledge about matter is quite limited by conditions which can exist on the Earth. The heavy ion (HI) collision experiment described in this dissertation aims to explore the equation of state of matter at extreme conditions which people have never experienced but strongly believe to exist abundantly in the universe, such as in cores of high-density stars. The properties of matter in such extreme condition are not simply predictable by extrapolating our limited knowledge of ordinary matter, but require different theoretical and experimental treatments. The relativistic heavy ion collision, the high energy collision of large nuclei which drives matter to an extreme condition, is quite different from general experiments which propose to explore the properties of matter, especially in the sense that the created system is not stable, but dynamically evolving and decaying into ordinary matter before it is observed.

For this reason we do not have control of the basic statistical parameters of the matter, such as volume, pressure or temperature, nor control on time for the system to be independent of initial conditions. Consequently, in this experiment simultaneous consistent measurements of many observables from different directions are required to get a picture of heavy ion collision dynamics and created matter. None of observables can provide a satisfactory picture of the system by itself, and the difficulty in measuring multiple observables in a consistent way has caused this heavy ion experiment to be large international efforts.

Among the various approaches to describe heavy ion collision dynamics and the properties of matter in extreme condition, analysis of fluctuations and correlations reveals the dynamics which exceed statistical expectation models. Correlations among particles indicate dynamical sources of particle production. Source identification and characterization of correlation structure in heavy ion collisions provide information about particle production mechanisms and transport (diffusion) properties of the system which are closely related to the description of the equilibration process. The tool to achieve this purpose must be very precise and generally multi-dimensional, as its connectivity to other observables is critical in heavy ion physics.

My work described in this dissertation intends to provide a quantitative description of correlation structure which accesses the dynamics of the collision system or the transport properties of matter created in the relativistic heavy ion collisions in a general way.

In the following section, we review why the physics associated with the matter created in heavy ion collisions is expected be different from that of ordinary matter and the expected scenario of heavy ion collision evolution.

1.1 Heavy Ion Collisions and QCD Expectation

The interaction among color-charged particles such as quarks and gluons, called the strong interaction, has been studied within the framework of Quantum Chromodynamics (QCD) [1]. At large momentum transfer QCD predictions have been successfully tested in many experiments [2, 3]. QCD was introduced as an analogue of Quantum Electrodynamics (QED). As a consequence of different transformation properties of the fields (Abelian to non-Abelian) the symmetries associated with QCD describe the interaction of color-charged quarks by the exchanges of gluons which also carry color charges, while the electromagnetic interaction is described by exchanges of chargeless photons. This is a fundamental difference between the theories.

There are two characteristic properties of the strong interaction most distinguishable from other interactions. One, called *asymptotic freedom* implies that current quarks can move almost freely within a typical hadron radius, which led to the success of bag models where the properties of hadrons are described by confined quarks moving freely within a hadron bag [4, 5]. The other is *quark confinement*, where the interaction among quarks becomes so strong at large distance that quarks are confined within hadrons, consequences of which are the large QCD coupling constant at large distance and the fact that we have never observed free quarks outside hadron radii. Hadrons are particles formed by combining constituent colored quarks in colorless combinations, with a cloud of virtual quarks and gluons which are together called partons. These features of QCD interaction, that all the quarks observed in nature are bound within hadrons or that the long-range interaction can only be treated non-perturbatively because of the large coupling constant, make it difficult to study the nature of this fundamental interaction at distances larger than the hadron radius ($\sim$ 1-5 fm).

Relativistic heavy ion collisions are proposed to study the long-range nature of the strong interaction experimentally by creating an extreme condition of very high temperature and energy-density. The QCD interaction in such extreme thermodynamic conditions is predicted to be so much weaker than that in cold nuclear matter, such as in our ordinarily world, that bound quarks are released and may obtain new degree of freedom [6, 7]. This new state of matter is called the deconfined phase, or quark-gluon plasma (QGP). The QGP is an idealized thermodynamically equilibriated state of strongly (color force) interacting matter, and the question whether these conditions are satisfied in heavy ion collisions is the subject of this study. Lattice QCD calculations predict that the transition to the deconfined phase is associated with a rapid energy-density increase with temperature and a more gradual increase in pressure indicating the existence of a phase transition at the critical temperature T_c of 150 $\sim$ 170 MeV at zero net baryon density [8, 9].

What we expect in heavy ion collisions and not in collisions of elementary particles for such a study is formation and development of thermodynamical properties, such as temperature, pressure, entropy, volume and energy-density in at least local equilibrium. The highest temperatures that have been created in collisions of gold nuclei accelerated by the Relativistic Heavy Ion Collider (RHIC) at Brookhaven National Laboratory (BNL) are expected to be above the lattice prediction values of critical temperature/energy-density. Heavy ion collisions represent an extraordinary opportunity to explore the question of phase transitions and QCD interactions. The experimental observation of properties of matter in the extremes of temperature and pressure will significantly extend our understanding of one of the most fundamental interactions and the equation of state of nuclear matter.

RHIC collisions provide us an opportunity to study QCD at finite temperature and very high energy density. However, in an actual heavy ion collision which evolves as a dynamical system, the sufficient condition for matter to exist as a QGP may only be partially achieved. In this dissertation, we establish a general analysis method for measurement of correlations at large momentum scale by which detailed studies of the created dynamical system become possible.

1.2 Space-Time Evolution of Collisions

The system around the collision point induced by the colliding nuclei is a dynamically evolving system in time and space. It has been recognized that the dynamics of heavy ion collisions are not simple but a complicated mixture of different physical aspects. In Fig 1.1, the expected space-time evolution of the interaction dynamics of heavy ion collisions is shown schematically. This

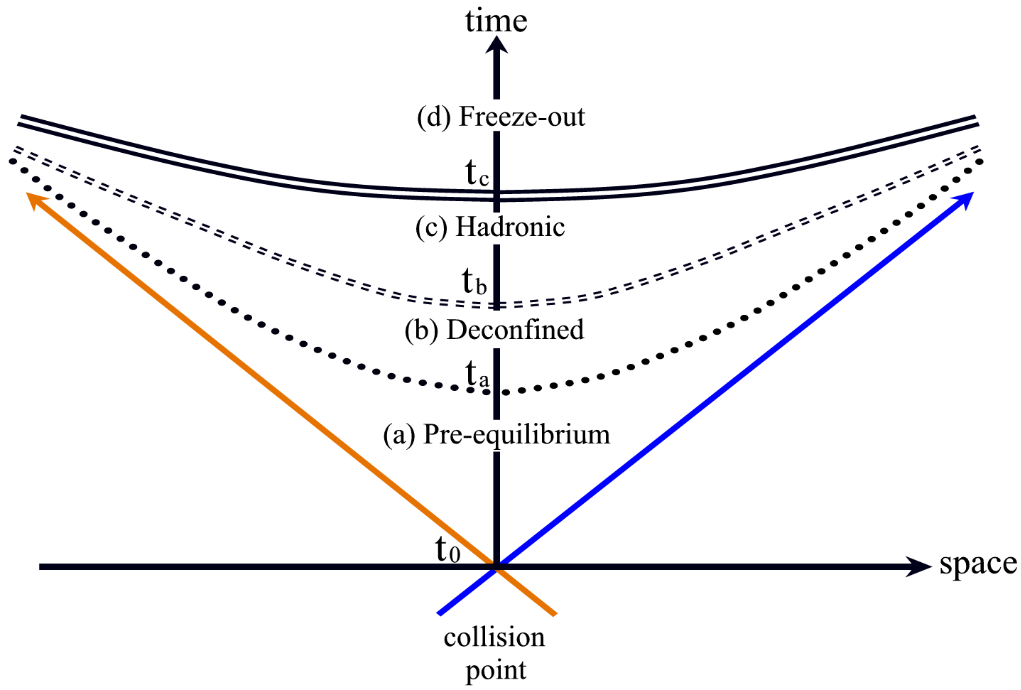

Figure 1.1: A schematic view of space-time evolution of collisions

figure shows that space-time evolution of the heavy ion collision is initiated by a scattering of composite nucleons or partons in the colliding nuclei at time t_0. Such initial scattering and associated energy transformations should be similar to that observed in elementary collisions such as proton-proton (p-p) collisions. It has been observed in p-p collisions that the total cross-section has elastic and inelastic components. The kinetic energies of colliding nucleons are kept in elastic reactions. In inelastic scattering, a certain amount of the kinetic energy is converted into production of primary particles, particles directly produced from the interaction region and not from decays of short life-time particles. Because the initial colliding beams carry only longitudinal kinetic energies, the energy-momentum of particles in the transverse direction is of particular interest and transverse dynamics is expected to be different from that along the beam direction. In general, precise information about equilibration processes is only accessible through transverse variables. This is due to the fact that there is a large collective flow or velocity component dominating in the longitudinal direction, and thermal aspects of the axial momenta of particles is primarily affected.

For this reasons, the vector-momentum of particles is effectively expressed in terms of longitudinal component p_z and transverse component p_t which is the projection of three-vector momentum $\vec{p}$ onto the transverse plane perpendicular to the beam (z-)axis. The longitudinal component of momentum is expressed in terms of (longitudinal) rapidity variable y_z, *i.e.*,

$$y_z = \frac{1}{2} \ln \left(\frac{E + p_z}{E - p_z}\right), \tag{1.1}$$

and the direction of momentum around the beam axis is expressed by an azimuth angle ϕ.

The rapidity variable has the advantage of a constant additive property under Lorentz transformation. The transformation from rapidity y_z in the center of mass frame to rapidity y_{z1} in the frame moving with relative velocity v in the z-direction can be expressed as $y_{z1} = y_z - \frac{1}{2} \ln \frac{1+v}{1-v}$. In high energy experiments, because rapidity requires the measurement of two kinematic variables, mass and p_z of the particle for example, the pseudorapidity variable is often preferred over rapidity because it requires only one kinematic variable, the polar angle θ between the beam axis and the particle momentum. Pseudorapidity η is defined as,

$$\eta = -\ln(\tan\frac{\theta}{2}). \tag{1.2}$$

When the energy of the particle is large compared to its mass, the pseudorapidity and the rapidity of a particle are approximately the same, $\eta \simeq y_z$.

Phase (a) in Fig. 1.1, the pre-equilibrium phase of the time interval between t_0 and t_a and the region near the colliding point, corresponds to the phase in which a series of parton scatterings occurs and the nature of the scatterings is expected to be similar to that in p-p collisions. The parton scattering in the p-p collisions is treated in part by perturbative QCD (pQCD), or QCD associated with the small coupling constant, as a reasonable approximation.

During the period of initial parton scattering, a certain amount of energy is deposited into a small interaction volume. The rapidity distribution of primary particles produced in p-p collision experiments [10] show an approximate trapezoidal distribution on longitudinal rapidity y_z. The leading baryons, which represent most of the net baryon number initially carried by the colliding nuclei, are observed in the large rapidity region in the center of mass frame. These observations are consistent with the picture that each nucleon in the beam may experience several scatterings as it encounters other nucleons or partons. From experimental observations in p-p collisions, the picture that some degree of symmetry along the beam axis (boost invariance) in the cylindrical region at mid-rapidity and near the beam axis may exist and the longitudinal expansion of such a region with respect to the beam axis has been proposed [11]. However, the particle production mechanism near mid-rapidity is considered to be a mixture of soft and hard processes, and the Lorentz invariance picture may only be applicable to the soft particles.

A particle produced via soft process is called a soft particle. The soft process belongs to QCD of small momentum transfer, and this non-perturbative QCD process with a large coupling constant can only be studied phenomenologically. A hard process involve QCD with large momentum transfers, for which the coupling constant is small and pQCD may be applicable [12, 13]. In consequence, the average hard-particle transverse momentum is larger than that for soft particles. The different transferred-momentum regions of particle production correspond to different particle distributions and subsequent histories of particles. Particle transverse-momentum spectra are dependent on soft-to-hard particle ratios, and in general the regions of spectra in which soft or hard particles are dominated are described by power-law distributions with different slope parameters. Although those distribution of particles of different origins are not strictly distinguishable by the single-particle distribution and the high transverse momentum in phase (a), the early era of collision, does not imply high-p_t particles at later times, it is observed from high energy p-p collisions that hard particles dominant for $p_t \geq 1$ GeV/c, and soft particles dominate for relatively low transverse momentum, typically $\leq$1 GeV/c. Because the particle distribution falls exponentially with transverse momentum, more than 80 % of particles are included in the soft-momentum region in Au-Au collisions at $\sqrt{s_{NN}} = 130$ GeV.

With a sufficient number of initial nucleon and parton multiple scatterings, a certain degree of local thermalization is expected to be achieved at phase (b) of Fig. 1.1. But the degree of achieved equilibrium in this phase is still an unrevealed quantity, and an important topic of study in heavy ion physics. If the energy density achieved in this phase is high enough, parton-parton scatterings of mean free path shorter than that for nucleon degrees of freedom are considered to further accelerate the equilibration process. This expectation motivated the study of matter in extreme condition using heavy ion collisions. The temperature achieved in this equilibrium phase is expected to be higher than the temperature necessary to deconfine quarks, and the phase transition to a QGP may occur in this phase. A large pressure and associated expansion are expected with such a high energy density and matter density.

As the incident nuclear pancakes pass through and fly away from the collision point and the distance between them exceeds their diameter, created high energy-density matter expands transversely and axially, and eventually the energy density crosses the QCD phase boundary again. Quarks are re-confined within hadrons or hadrons are fragmented from the color field in phase (c) of Fig. 1.1. As the hadronization process probably does not occur all at once, some parts in space and time of this phase may exist as mixtures of hadrons and color-deconfined matter. Hadron density is still high in phase (c) and it is considered to be a strongly-interacting hadron gas. As the hadrons still undergo radial expansion, the scattering among hadrons ceases at the kinetic freeze-out (decoupling) time t_{last}. The momentum distribution of particles actually measured by our detectors is considered to be unchanged from freeze-out time, excepting small distortions by the final state (long-range Coulomb and nuclear) interaction among particles between kinetic freeze-out and the time of observation, which are the subjects of systematic corrections.

Although our interest is mostly in the properties of QCD interaction in phase (b), all effects from interactions in phase (a), (b), (c) are contributing to the observed quantities, and some are expected to dilute the signals created in the deconfined phase. The investigation of statistical properties of produced strongly-interacting matter and its dynamical evolution with measured quantities observed at the final state is one of the most challenging tasks in the heavy ion program. There has been a number of possible signatures proposed to study the dynamics of heavy ion collision which are sensitive to the space-time region of possible QGP formation. Each quantity is constructed to reflect some properties of the inter-phase [14], and measured quantities are compared with expected values contributed from (a) and from the hadronic final state, which are obtained from hadron-hadron and hadron-nucleus collision experiments. By comparing these results of elementary interactions with heavy ion collisions, we indirectly investigate the interaction in the space-time region of (b) and (c).

Because of this indirect observational nature of heavy ion collisions, the expectations that we derived from elementary collisions play a major role in the relativistic heavy ion experiments. In this study, results are compared with correlation structure observed in p-p collisions and these elementary collisions have exhibited many interesting correlation structures. In p-p collisions, soft particle production was phenomenologically described in terms of a color-string parallel to the beam axis with partons at each end of the string. As the string is stretched along the axis, it fragments to produces other partons at each end of the fragments. The high transverse momentum part of p-p collision spectra are well matched to the description that high-p_t partons resulted from hard parton-parton scattering are fragmented into a cluster of particle in which particles are correlated in momentum. Those pictures of particle production are obtained from correlation structures which result from local conservation of momentum and/or charges. How these particle experiences different histories in Au-Au collisions and carry correlation information to the final state is an important study which may lead to a better understanding of particle production in heavy ion collisions.

Hard particles were expected to 'remember' the early stages of the collision more then soft particles but we find that soft particles also remember the earlier phase, which is then to be accessible from final state correlations. Because soft particles mainly fragment from the deconfined color medium, soft-particle correlations are expected to strongly reflect the properties of the color medium.

1.3 Fluctuation and Correlation Analysis

The dynamics of heavy ion collisions produce correlations among particles; thus equivalently the correlation measurements tell us about heavy ion dynamics, and correlations are sometime measured as a fluctuation beyond statistical expectation (non-statistical fluctuation). The *event-by-event* analysis of global fluctuations has been developed as a precise tool in the search for non-statistical fluctuations of event-wise quantities [15]. Fluctuations in the final state may be related to the statistical properties of the hot matter at the freeze-out time; examples of such connections are shown as the relation of fluctuation of the slope parameter of transverse momentum to temperature fluctuations [16–18] and thus the heat capacity [19], multiplicity and entropy [20, 21] or the hadronic matter compressibility [22], and particle species fluctuations such as the fluctuations of kaon-to-pion number ratio or positive-to-negative charged-particle ratios may gives information about earlier times [23–25]. Possible observation of critical fluctuations associated with the phase transition would give direct information about the order of the transition and the effective degrees of freedom in the earlier phase [26].

However, fluctuation analysis in a fixed acceptance cannot determine the mechanism of the fluctuation production by itself but requires additional work to track down the sources of fluctuations. As correlation structure corresponds to the source of dynamical fluctuation, a careful study of correlations in a general way and form relatable to fluctuation analysis will open up new paths to understanding fluctuations.

The two-particle correlation analysis presented in this dissertation serves such a role and gives further understanding on underlying correlation and particle production mechanisms in relativistic heavy ion collisions, thus the regime of non-perturbative QCD.

1.4 Overview

The purpose of the study described in this dissertations is the qualitative evaluation in a model independent way of surviving correlation structure in the hadronic final state produced in ultra relativistic heavy ion collisions. The sampled collisions used in this analysis are created by RHIC and recorded with the STAR detector. In Chapter 2, an overview of the collider and experimental setup used for the first-year data taking is presented. The appropriate forms of correlation analysis for a system which involves complex dynamical evolution is considered in Chapter 3. The relation between correlation analysis and the study of fluctuations of the event-by-event global observables such as event-wise average p_t is also studied. Detailed particle production mechanisms in heavy ion collisions are investigated by comparison of the obtained correlation structure with the known correlation context from elementary collisions, such as cluster/string fragmentation or mini-jets. In Chapter 4, physics involved in the two-particle analysis and expected correlation structure from elementary collisions are discussed. Data are selected so as to exclude effects from online and offline systematics. In Chapter 5 detailed event, track and particle pair selections are described. Finally, analytic results for transverse and axial momentum spaces are presented and discussed in Chapters 6 - 8.

Chapter 2

Experiment

The data analysis presented in this dissertation is based on event samples of Au-Au collisions at center of mass energy of 130 GeV per nucleon pair ($\sqrt{s_{NN}} = 130$ GeV) produced by the Relativistic Heavy-Ion Collider (RHIC) at the Brookhaven National Laboratory (BNL) and measured by the Solenoidal Tracker at RHIC (STAR) detector during Summer of year 2000, the first-year RHIC run.

RHIC is designed to accelerate various kinds of ions and collide them at the top energy ranging from 200 GeV to 500 GeV depending on the ion species [27]. The heaviest nuclei to be accelerated is gold nuclei (atomic mass 197) which can be accelerated up to $\sqrt{s_{NN}} = 200$ GeV. While the energy achieved during the first-year run was not full designed energy, the energy increase from past experiments is very large. Past, present and future heavy-ion accelerators and their achieved (planned) energies are listed in Table 2.1. Although the ion species flexibility of the RHIC is notable and crucial for the other important physics purposes, in the following only the RHIC operation in the case with gold ions is described.

Accelerator	Ion species	$\sqrt{s_{NN}}$ (GeV)	Starting year
AGS, BNL	O, Si	5.4	1986
	Au	4.9	1992
SPS, CERN	O, S	19.4	1986
	Pb	17.3	1994
RHIC, BNL	Au	130	2000
	Au	200	2001
	Au	62	2004
LHC, CERN	Pb	5500	2007 (planned)

Table 2.1: Accelerators for relativistic heavy-ion collision experiments

2.1 RHIC Facility

The main components of the RHIC are two intersecting rings of superconducting synchrotrons. RHIC has the capability to make collisions at six intersection positions in its 3,843 m circumference. The important components of the synchrotron rings are 1760 superconducting magnets kept at a temperature of < 4.6 K to bend and control tracks of ion beams, and 4 rf cavities. The basic RHIC parameters are listed in Table 2.2.

Basic Parameters	
No. of bunches/ring	57
No. of ions/bunch	1×10^9
bunch separation (m)	67
bunch separation (ns)	213
No. of crossing points	6
average luminosity(cm^{-2}sec-1)	$\sim 2 \times 10^{36}$
lifetime of beam (hour)	10

Table 2.2: Basic parameters for the RHIC

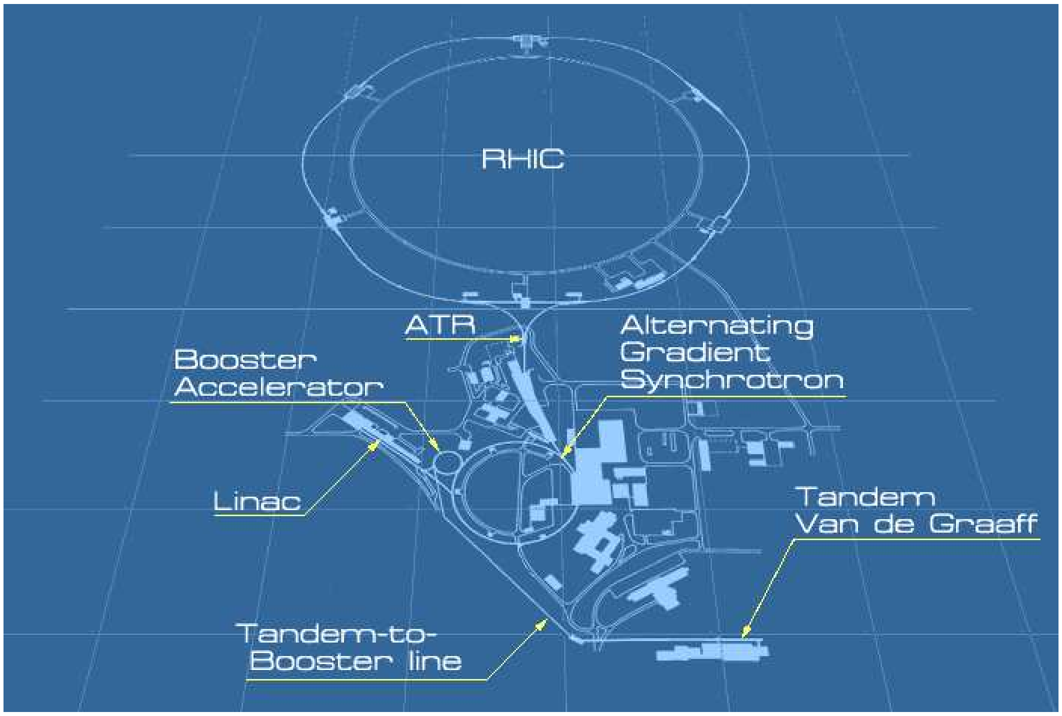

Figure 2.1: Layout of the RHIC complex

Before ion beams are injected into the RHIC rings, the ions are pre-accelerated and bunched. The injectors consist of three accelerators, the Alternating Gradient Synchrotron (AGS), the Booster synchrotron and Tandem Van de Graaff accelerators. The layout for the RHIC collider and injectors are shown in Fig. 2.1.

The gold ions emitted from ion source are initially with charge -1 and accelerated by Tandem Van de Graaff. At the middle of Tandem Van de Graaff the ions pass gold foils and are positively ionized to charge +14. The ions with kinetic energy of 1 MeV/u are transferred to the Booster synchrotron to be accelerated to 72 MeV/u. At the end of the Booster acceleration these ions

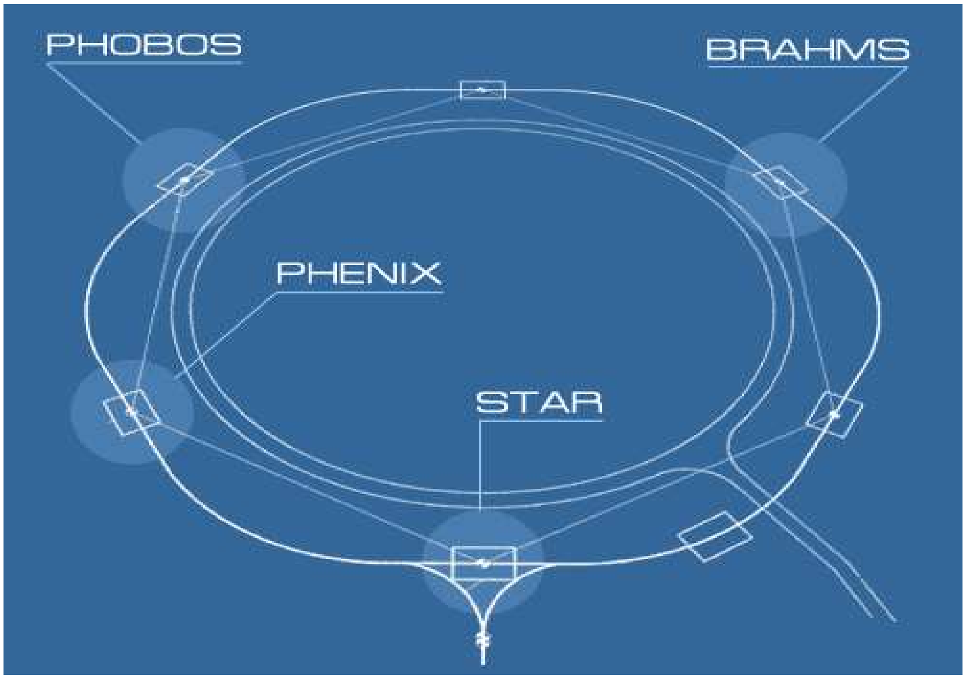

Figure 2.2: Position of four experiments around the RHIC ring

are further stripped to be charged to +77 and the ion beams are contracted as bunches and enter the AGS. The AGS accelerates the ions to the kinetic energy of 10.8 GeV/u. Then the last two electrons are finally stripped and the ions are to be charged to +79. These ion bunches are injected to the RHIC and accelerated to the full RHIC energy.

2.2 STAR Experiment in Year 2000

There are four experiments at the RHIC ring and the STAR (Solenoidal Tracker At RHIC) experiment is located at 6 o'clock insertion position (Fig. 2.2).

The main devices of the first-year configuration of the STAR experiment are a large-cylinder Time Projection Chamber (TPC) and a solenoidal magnet. The STAR TPC covers the 6 o'clock collision point of the RHIC ring over the length of 4 m in the beam direction and 4 m in diameter, and the solenoidal magnet surrounding TPC is capable of maximum magnetic field strength of 0.5 T, although during the first-year run the magnet was operated at 0.25 T. In addition to the detectors used for event reconstruction, two Zero-Degree Calorimeters (ZDCs) and a Central Trigger Barrel (CTB) are used for event triggering. A layout of the sub-systems of the STAR detector is shown in Fig. 2.3.

There were other STAR subsystems for year 2000, but they were not used for the analysis described in this dissertation. These include a Ring Imaging Cherenkov detector (RICH) of $|\Delta\eta| < 0.3$ and $|\Delta\phi| < 20°$ in acceptance which corresponds to 2% of TPC acceptance [28] and a prototype ladder of Silicon Vertex Tracker (SVT) of 6.3 cm width and 44.1 cm length in beam direction laid at 10.16 cm above the beam line [29].

2.3 Magnet

A large solenoidal magnet weighing over 1100 tons surrounded all the subsystems which existed in year 2000 except ZDCs. It is essential for the momentum determination of produced particles. The magnet is designed to provide a nearly uniform field of range $0.25 < |B_z| < 0.5$ T parallel to the beam direction (z-direction) over the entire TPC volume. This requirement is important since uniformity of magnetic field simplifies tracking of particle tra-

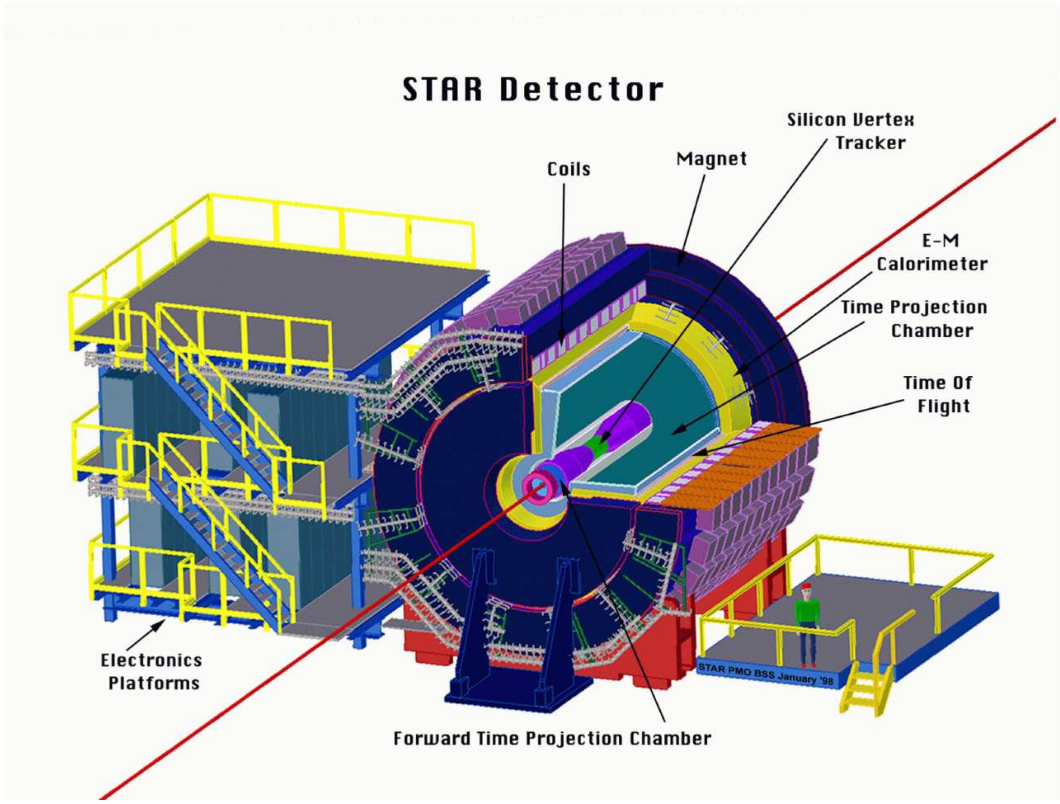

Figure 2.3: the STAR detector

jectories and the inhomogeneity results in drift distortions of trajectories, and introduces systematic uncertainties in momentum. Knowledge of the magnetic filed inside the TPC is critical for momentum analysis. Magnetic-field mapping was performed before the TPC installation. The radial component of magnetic field (B_r) is measured at both ends of the TPC ($z = \pm 2.1$ m) and the obtained value is approximately ± 25 Gauss for the half-field ($|B_z|$=0.25 T) operation. The azimuthal component (B_ϕ) is less than ± 1.5 Gauss over the TPC volume [30]. The inaccuracy of hit positions associated with magnet-field distortion is corrected by the STAR reconstruction software and systematic uncertainty due to obtained momentum resolution by the event reconstruction is negligible in this analysis.

2.4 Time Projection Chamber

In the most-central Au-Au collisions at the full RHIC energy, there are approximately two thousands charged particles observed over the acceptance of this study. The Time Projection Chamber (TPC) [31], the STAR's main tracking detector, is designed to record low-multiplicity to high-multiplicity collision events in which more than 2000 charged particles per event could be produced over its large acceptance by storing sufficient information to reconstruct 3-dimensional images of charged-particle trajectories.

A schematic layout of TPC components is shown in Fig. 2.4. The main components of the TPC are the outer and inner field-cage cylinders. The volume between the two cylinders filled with gas corresponds to the active tracking volume for the TPC. The high-voltage Central Membrane (CM) is at the center of the TPC (z = 0 cm), and Multi-Wire Proportional Chambers (MWPC) are at both end-caps ($z = \pm 210$ cm).

A charged particle passing through gas produces ion pairs left along its trajectory, and then the electric field applied parallel to the beam axis accelerates the electron ion pairs toward the end-cap. Drifting electron clusters are amplified by high electric field near the anode wires on the readout pad which induces image charges on the pad plane. The 3-dimensional coordinates

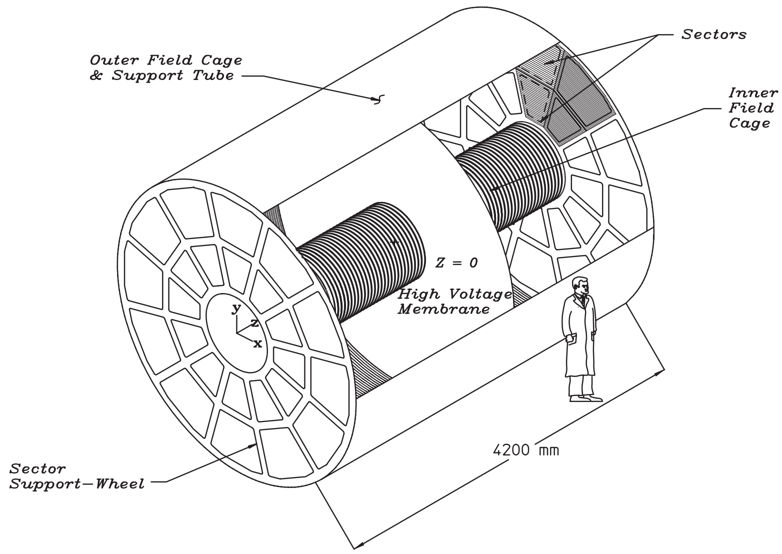

Figure 2.4: Schematic layout of Time Projection Chamber

and sizes of the image charges are stored as raw data of time sequences of ADC values from each pad. For reduction of the data volume, the background noise is calculated as data average without collisions and subtracted before the data is stored.

2.4.1 Drift Gas and Field

The dimension of active TPC tracking volume is defined by the outer radius of the IFC (50 cm), the inner radius of OFC (200 cm), the two end caps at z = ± 210 cm and the CM dividing whole TPC volume into two parts. The volume is filled with the P10 gas, a mixture of 90% of argon and 10% of methane. The P10 drift gas is chosen to satisfy several simultane-

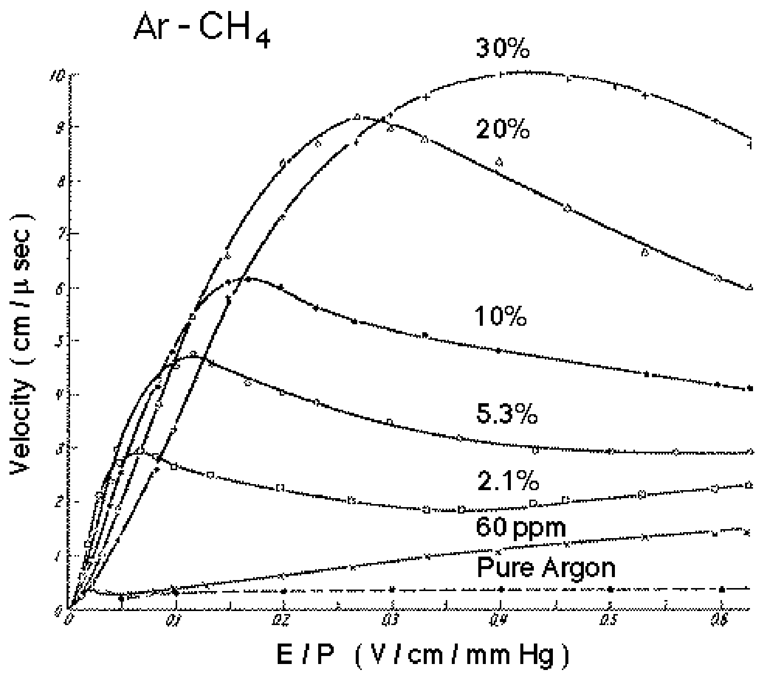

Figure 2.5: Electron drift velocity in various $Ar + CH_4$ mixture vs. electric field

ous requirements from tracking accuracy and experimental treatment. These requirements set limits on several conditions; for example, the multiple scattering frequency, the puerility of the gas, the drift velocity change under different electric field, the hazardousness to the other detector system in the STAR and/or to the environment and the cost.

The choice of P10 drift gas sets the TPC drift electric field at 148 V/cm for year 2000. In Fig. 2.5, the drift velocities of electron in the P10 gas labeled by 10% is shown as a function of electric field. The STAR TPC drift field corresponds to slightly offset from the peak of the P10 drift-velocity curvature at 0.16 V/cm/mm-Hg at normal pressure and temperature, such that the drift velocity is the less sensitive to small changes in gas pressure and/or temperature but the change still gives information about the parameter changes. The drift field is provided by the CM held at -31 kV, the end cap pad planes held at the virtual ground and the inner and outer field cages which are set to give constant gradient from the CM to both ends of the TPC with its 363 equipotential metal-coated Kapton rings and 366 resistors for each cages.

2.4.2 Multi-Wire Proportional Chamber

When the drifting electrons are close to either ends of the TPC, the MWPC amplifies the cluster of electrons by the avalanche process in the high electric field and induces the image charges on the readout pad plane.

Each of the MWPC is divided into 12 sectors as shown in Fig. 2.6 and each sector consists of inner and outer sectors. The geometry of one full sector is shown in Fig. 2.7. The MWPC consists of three layers of wire planes and one pad plane at each end of the TPC as shown in Fig. 2.8. The planes consist of the gating grid at z = ± 208.7 cm, the ground grid at z = ± 209.3 cm, the anode grid at z = ± 209.5 cm for inner sectors and at z = ± 2097 mm for outer sectors and the pad plane at z = ± 209.7 cm for inner sectors and at z = ± 210.1 cm for outer sectors from the center of TPC.

The gating grid consists of 75 μm wires with 1 mm pitch which close and open the 'gate' to the amplifier-readout region and controls the electrons and positive ions in and out by changing the voltages. The ground grid 75 μm

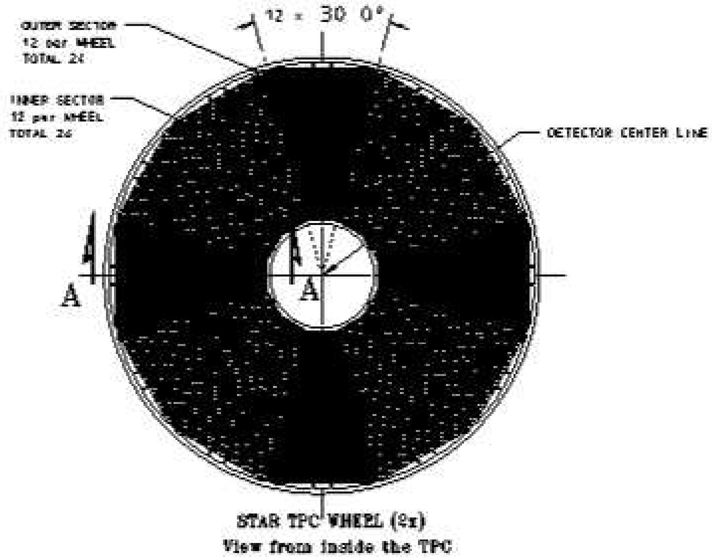

Figure 2.6: End view of the TPC from its center, each end cap consists of 12 sectors each of which are subsequently divided into outer and inner subsectors.

wires with 1 mm pitch terminate the electric field in the amplifier region and serves as a shielding for the pad plane from the noise due to voltage changing of the gating grid. The anode grid of 20 μm wires with 4 mm pitch provides the high voltages for the avalanche process. The pad plane is connected to the front end electronics for readout.

The centers of sectors are along the lines from beam axis to 1-12 o'clock positions, and the wires of three grid layers are perpendicular to them such that the measurement of the highest-p_t track curvatures can be determined with the best resolution. One inner-sector pad plane consists of 13 pad rows. Each rectangle pad has the size of 2.85 mm in wire direction and 11.5 mm in the radial direction with 0.5 mm isolation gap in both directions. The spacing

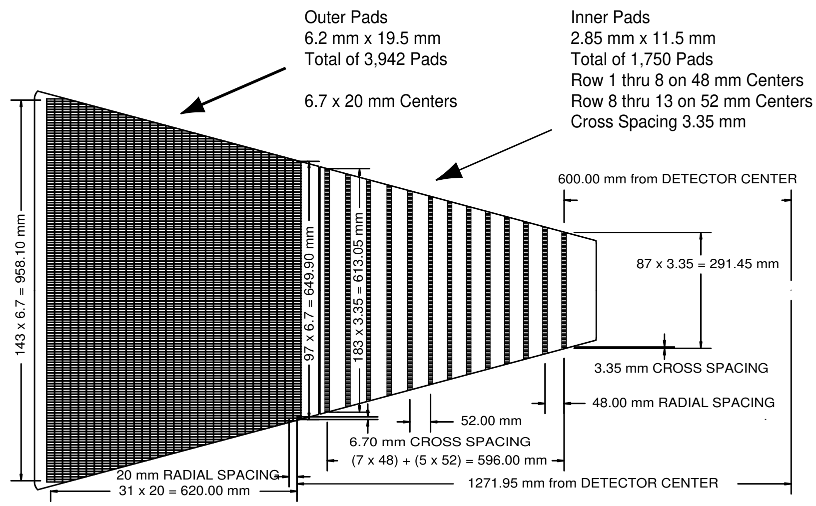

Figure 2.7: Schematical view of a TPC pad plane for one full sector. Each sector consists of outer and inner sectors.

between each pad row from 1st to 8th pad rows are 36 mm, and 40 mm from 8th to 13th rows in the radial direction, and no spacing in the wire direction. The basic configuration for the outer sectors are similar to that of inner sectors but there is a small difference in geometry. One outer-sector pad plane consists of 32 pad rows. Each pad dimension is 6.2 mm in the wire direction and 19.5 mm in the radial direction. There are 0.5 mm isolation gaps between pads in both wire and radial directions and no spacing between rows. The inner sector anode plane are at 2 mm above the pad plane and outer sector anode plane are at 4 mm above the pad plane.

The difference in pad size and pad row spacing for the inner and outer sectors is due to different optimizations. For the inner sectors, the smaller pad size is chosen such that it gives good two-hit resolution in the higher density

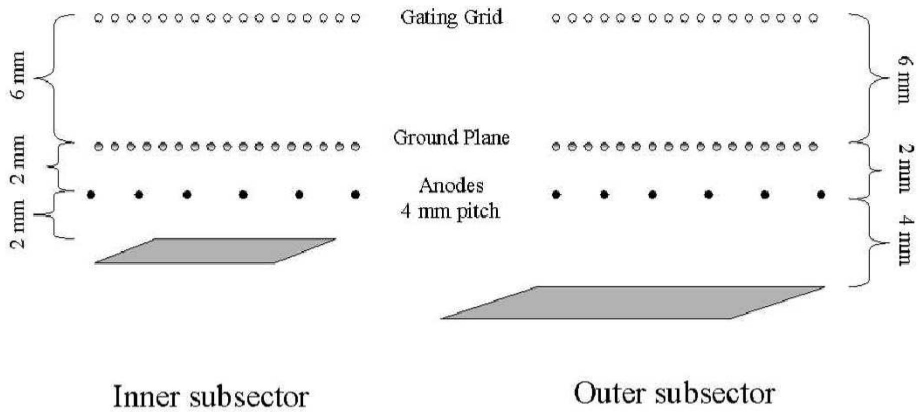

Figure 2.8: A sketch of the plane geometry of MWPC; the beam direction is perpendicular to these planes.

region with continuous pad coverage. For the outer sectors, the size is designed such that it gives good dE/dx energy loss information for particle identification in the lower track-density region. The total number of pads is limited by the space required for the TPC electronics. The distance between the anode-wire plane and pad plane is determined from the pad sizes. Given anode-pad plane spacing and pad sizes, the gas gain can be controlled by anode voltages. To set the signal-to-noise ratio to about 20:1 for both inner and outer sectors, the anode voltages for inner sector of 1170 V and 1390 V for outer sector are chosen. The total of 136,608 pads are used for the measurements of transverse coordinate of ionized electron clusters. For the longitudinal direction, image charges on the pad planes are sampled with the rate of 9.4 MHz by filling 380 time buckets typically out of the maximum possible number of 512. The total pixel occupancy was $\sim 10\%$ of total available pixels in an event.

The readout of induced pad plane signals and segmentation in the time (longitudinal) direction is performed by the TPC front-end electronics (FEE) [32] initiated by a trigger word from Level-0 trigger system. There are 181 FEE cards and 6 supporting readout boards per sector. Each FEE card holds 2 of two types of chips, the SAS preamplifer/shaper chip and the SCA switched capacitor array chip, which correspond to 32 TPC-pad readout channels. The SAS chip contains 16 channels of integrating preamplifier and shaper, and the SCA chip holds a 16 channel-wide, 512 time-bin switched-capacitor array together with a 12-bit ADC. Details about the chip are found in [33]. The readout board provides power to the FEE cards, accepts signals from the FEE cards and transmits it via a 1.2 Gbit/s fiber optical link to the data acquisition system (DAQ) which compresses data volume and sends data to storage system unless the event is rejected by the higher-level (Level-1 and 3 for year 2000) trigger systems.

2.5 Trigger

Effective online event selection is important for the STAR experiment, because the RHIC beam-crossing rate is about 9.4 MHz and with high-luminosity ion beams, the interaction rate is close to the beam-crossing rate, while the maximum data readout-storage rate for the STAR experiment is about 100 Hz. For the year 2000, the collider was operated with about 10% of the design luminosity, the interaction rate of about 144 Hz was achieved by the RHIC and average STAR data readout rate was about 5 Hz.

During the first-year run, two general event trigger settings were used

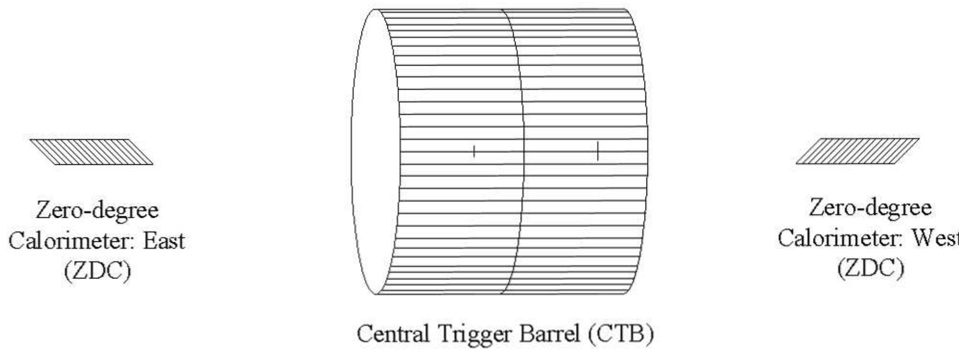

Figure 2.9: A sketch of the trigger detectors used during the first year data taking. The central trigger barrel is surrounding the TPC and zero degree calorimeters are at ± 18 m from the center of TPC near beam line.

such that various physics analysis can be done on the data. One setting is called 'hadronic minimum-bias' and the other is 'central'. These data were triggered using the Central Trigger Barrel (CTB) and two Zero-Degree Calorimeters (ZDCs) shown in Fig. 2.9 [34]. The ZDCs are located at ± 18 m from the center of the TPC (east and west from the STAR). The ZDCs are the standard triggering detectors and the configuration of the ZDCs relative to crossing point is common to all four other experiments around RHIC [35]. Each ZDC is a small transverse-region hadron calorimeter which measures energies of neutrons in the fragments of ion beams within a cone of 2 milliradians. The trajectories of electrically-charged nucleons (protons) are curved by the DX dipole magnets which control the ion beams. The positions of the dipoles are shown in the lower panel in Fig. 2.10.

The *minimum-bias trigger* requires signals from both ZDCs that exceed a threshold value which is typically about 40% of the single neutron peak. This

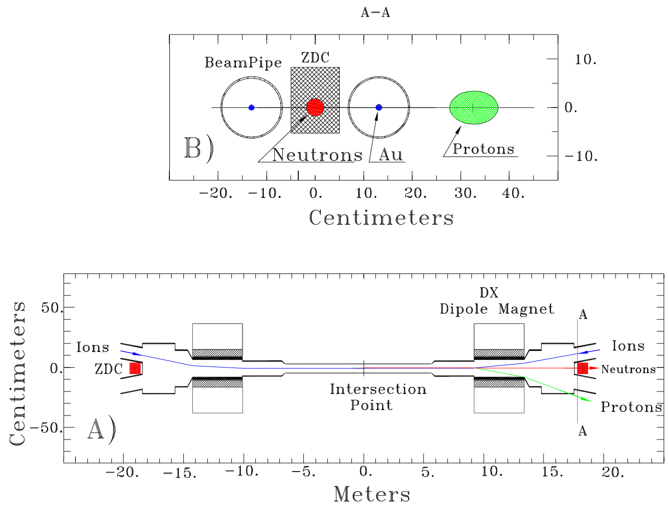

Figure 2.10: Geometry of the Zero Degree Calorimeters relative to RHIC beam lines from [35]. (A) horizontal cutaway view and (B) transverse cutaway view. Neutrons are deposited into the ZDCs while protons are curved away from it.

requirement avoids triggering on beam-gas interactions and ion interactions at far from the center of the TPC. The CTB is an array of 240 scintillator slats cylindrically placed on the aluminum support rails attached to the outermost shell of the TPC. The CTB measures charged-particle multiplicity over the coverage of full azimuth angle and $|\eta| < 1.0$. The main component of each slat is a scintillation radiator made of BC408 plastic photomultiplier tube which amplifies the signal and is shown in Fig. 2.12. The correlation of CTB and ZDC signals is shown in Fig. 2.11. The *'central' events* are triggered by requiring the CTB signals above a threshold in addition to the ZDC coincidence signal which gives a set of events with high multiplicity only.

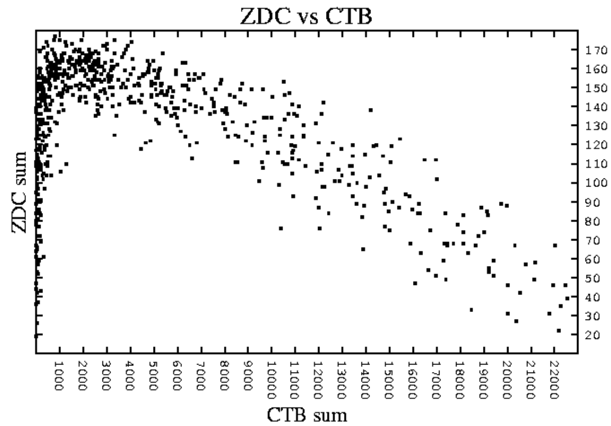

Figure 2.11: The correlation between ZDC and CTB signals [34]

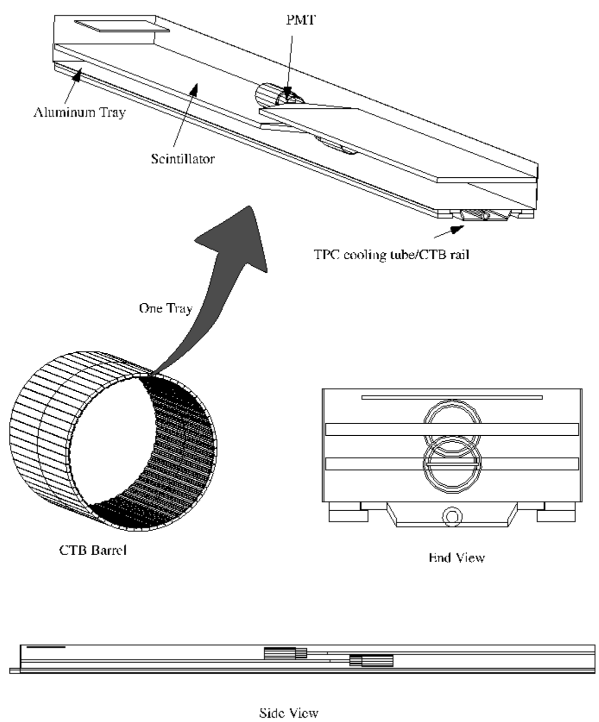

Figure 2.12: The configuration of the Central Trigger Barrel [34]

Chapter 3

Two-particle Correlation Analysis Methods

This study is the first two-particle correlation analysis of all three momentum components for particles produced at the RHIC energy. In this chapter, we consider the appropriate forms of correlation analysis suitable for such study, and of the most general forms because correlation mechanisms in heavy ion collisions at this energy are still unknown. After sufficient general study, identification of correlations which belong to different physical mechanisms and specific correlation study focusing on each mechanism may become possible. We elicit correlation contents from two-particle density ρ_2 which contains all two-particle correlations. The extraction of the interesting correlation contents is performed by comparing ρ_2 and a two-particle reference density distribution. In the last section we show the connection between correlation analysis and fluctuation analysis, and thus demonstrate that this work reveals the dynamical origins of excess event-by-event fluctuations.

3.1 Two-particle Densities

Two-particle density $\rho_2(p_{t1}, \eta_1, \phi_1, p_{t2}, \eta_2, \phi_2)$ is the pair-number distribution normalized by dividing by the total number of pairs in the two-particle momentum space and is obtained by counting numbers of pairs in each of $N_{bin,1} \cdot N_{bin,2}$ bins of size $\delta p_1 \cdot \delta p_2$ defined in the 6-dimensional two-particle momentum space. The size of 6-dimensional two-particle momentum space under study is written as a product of 3-dimensional single-particle momentum acceptances $\Delta p_1 \cdot \Delta p_2$, where $\Delta p_i \equiv (\Delta p_{ti}, \Delta\eta_i, \Delta\phi_i)$ indicates the momentum acceptance of the i_{th} particle in a pair, defined by the acceptance of transverse momentum Δp_{ti}, pseudorapidity $\Delta\eta_i$ and azimuth angle $\Delta\phi_i$.

A two-particle density can be formed for any observable quantity. In this study, two-particle number densities ρ_2 are formed for pairs with like-sign (LS) and unlike-sign (US) charge-combinations, motivated by the correlation structures observed in p-p collisions. The LS and US two-particle densities are constructed with the assumption of charge symmetry of two-particle distributions: *i.e.*, $n_2^{++}(\vec{p_1}, \vec{p_2}) \simeq n_2^{--}(\vec{p_1}, \vec{p_2})$ and $n_2^{+-}(\vec{p_1}, \vec{p_2}) \simeq n_2^{-+}(\vec{p_1}, \vec{p_2})$, where $n_2^{ab}(\vec{p_1}, \vec{p_2})$ denotes the number distribution of pairs in which one particle has momentum $\vec{p_1}$ with its charge sign a and the other has $\vec{p_2}$ and b. The LS and US two-particle density distributions are written as,

$$\rho_2^{\substack{LS \\ US}}(\vec{p_1}, \vec{p_2}) = \frac{n_2^{\substack{++ \\ -+}}(\vec{p_1}, \vec{p_2}) + n_2^{\substack{-- \\ +-}}(\vec{p_1}, \vec{p_2})}{\int_{\Delta p_1} \int_{\Delta p_2} n_2^{\substack{++ \\ +-}}(\vec{p_1}, \vec{p_2}) + n_2^{\substack{-- \\ -+}}(\vec{p_1}, \vec{p_2}) \;\; d\vec{p_1} d\vec{p_2}}. \tag{3.1}$$

The total numbers of LS and US pairs including double-counting pairs in an event are simply related to the total number of positive (negative) charged particles $N^{+(-)}$ in the event by $\int_{\Delta p_1} \int_{\Delta p_2} n_2^{\pm\pm}(\vec{p_1}, \vec{p_2}) d\vec{p_1} d\vec{p_2} = N^{\pm}(N^{\pm} - 1)$ for LS and $\int_{\Delta p_1} \int_{\Delta p_2} n_2^{\pm\mp}(\vec{p_1}, \vec{p_2}) d\vec{p_1} d\vec{p_2} = N^{\pm} \cdot N^{\mp}$ for US before the pair-wise cuts (Sec. 5.3) are applied.

The dimensionality of two-particle distributions can be reduced by integrating over variables other than those of interest, for visualization and further analysis. For example, the two-particle transverse-momentum distribution is obtained by integrating the 6-dimensional function Eq. 3.1 over two-particle axial momenta (η_1,η_2,ϕ_1,ϕ_2) as,

$$\rho_2(p_{t1}, p_{t2}) = \int_{\Delta\eta_1} \int_{\Delta\eta_2} \int_{\Delta\phi_1} \int_{\Delta\phi_2} \rho_2(\vec{p_1}, \vec{p_2}) d\eta_1 d\eta_2 d\phi_1 d\phi_2. \tag{3.2}$$

To obtain the correlation contents of interest, the two-particle distributions are compared with reference distributions which include all correlations except those under study, by taking differences or ratios. Experimentally, the mixed-pair distribution $\rho_{2,mix}$ serves as such a reference. Mixed pairs are pairs whose constituent particles belong to different events selected to have the same single-particle distribution as the distribution of pairs from the same events but which do not contain two-particle correlations. The details of such mixed-pair construction are discussed in Sec. 5.5.

The correlation function C_2 is defined as a difference between two-particle object distribution ρ_2 and reference distribution $\rho_{2,mix}$,

$$C_2(\vec{p_1}, \vec{p_2}) \equiv \rho_2(\vec{p_1}, \vec{p_2}) - \rho_{2,mix}(\vec{p_1}, \vec{p_2}). \tag{3.3}$$

The comparison may also be obtained by taking ratios instead of differences. Because both numerator and denominator have the same single-particle efficiency distributions, by taking the ratios, effects from the detector acceptance and efficiency distribution cancel at the single-particle level. Thus, we can study the two-particle correlation avoiding difficulties arising from the correction of single-particle efficiency changes in two-particle distributions, which would require a model of the associated two-particle correlations. For this reason, the *two-particle density ratio* $R(\vec{p_1}, \vec{p_2})$ is measured in this study, defined by

$$R(\vec{p_1}, \vec{p_2}) \equiv \frac{\rho_{2,sib}(\vec{p_1}, \vec{p_2})}{\rho_{2,mix}(\vec{p_1}, \vec{p_2})} = \frac{C_2(\vec{p_1}, \vec{p_2})}{\rho_{2,mix}(\vec{p_1}, \vec{p_2})} + 1, \tag{3.4}$$

where $\rho_{2,sib}$ denotes the two-particle density of same-event pairs (sibling-pairs).

In terms of R, correlations are expressed as deviations from 1, and thus the deviation quantity $R-1$ is often plotted. As the construction procedure of two-particle density ratios includes binning of continuous momentum variables, what the momentum variables indicate in the following is the central value of the momentum bin with indices i, j, *i.e.* p_i indicates the central value of the i_{th} momentum bin, and R_{ij} indicates the two-particle density ratio in momentum bin of p_i and p_j, although indices are normally omitted if there is no confusions.

3.2 Autocorrelations and Joint Autocorrelations

The *autocorrelation function* is generally defined as the cross-correlation of a signal at x with the signal itself at different points $x + x_\Delta$ [36, 37] which can be expressed as one-dimensional correlation histograms on pair difference variables. This form is useful when correlation structures have small dependence on sum variables and are then approximately expressed as a function of

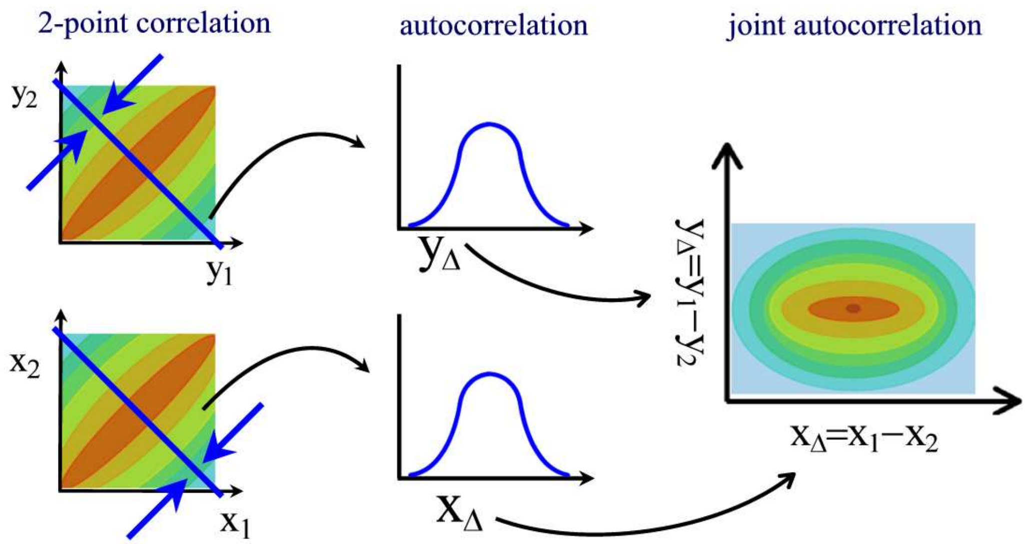

Figure 3.1: Sketch of relation of autocorrelation function, joint autocorrelation and two-particle distribution ratio. The autocorrelation is obtained by taking the average of two-particle density ratio contents over pair sum variables.

difference variables only.

In this analysis, the autocorrelation function $A(p_\Delta)$ of pair momentum difference variables ($p_{t\Delta} \equiv p_{t1} - p_{t2}$, $\eta_\Delta \equiv \eta_1 - \eta_2$ and $\phi_\Delta \equiv \phi_1 - \phi_2$) is constructed from a two-particle density ratio by taking an average over pair sum variables ($p_{t\Sigma} \equiv p_{t1} + p_{t2}$, $\eta_\Sigma \equiv \eta_1 + \eta_2$, $\phi_\Sigma \equiv \phi_1 + \phi_2$) or in other words the average of slices of the two-particle density ratio at different pair-sum variables. Thus the autocorrelation function is related to the two-particle density ratio R by

$$A(p_{\Delta,j}) \equiv \frac{1}{N_{bin,\Sigma}} \sum_{i=1}^{N_{bin,\Sigma}} \left[R(p_{\Sigma,i}, p_{\Delta,j}) - 1\right], \tag{3.5}$$

where $N_{bin,\Sigma}$ is the number of bins along constant $p_{\Delta,j}$ diagonals. If the two-particle density ratio has small dependence on the sum variables, the dimension of two-particle density ratios can thus be reduced *without relevant information loss* of the correlation structure. The correspondence between autocorrelation functions of two difference variables can be investigated with *joint autocorrelations* of different momentum combinations, for examples, $p_{t\Delta} \otimes \phi_\Delta$, $\eta_\Delta \otimes \phi_\Delta$ or $\eta_\Delta \otimes p_{t\Delta}$. The joint autocorrelations are obtained by changing the integrating variable in Eq. 3.2 by the difference or sum variables excepting the two of interest. An illustrative comparison of the autocorrelation to the two-particle density ratio is shown in Fig. 3.1.

3.3 Inclusive and Semi-inclusive Distributions

The two-particle correlations studied in this dissertation are obtained inclusively from sets of events in the multiplicity range $N_{min} < N_j < N_{max}$. The relation between inclusive C_2 obtained from the total number of N_E events and semi-inclusive correlation C_2^j from N_E^j events with multiplicity N_j and pair multiplicity n_2^j is written as

$$\begin{aligned}
&C_2(\vec{p_1}, \vec{p_2}) = \rho_2(\vec{p_1}, \vec{p_2}) - \rho_{2,mix}(\vec{p_1}, \vec{p_2}) \\
&= \frac{\sum_{N_j} N_E^j n_2^j \rho_2^j(\vec{p_1}, \vec{p_2})}{\sum_{N_j} N_E^j n_2^j} - \frac{\sum_{n_{j,mix}} N_{E,mix}^j n_{2,mix}^j \rho_{2,mix}^j(\vec{p_1}, \vec{p_2})}{\sum_{n_{j,mix}} N_{E,mix}^j n_{2,mix}^j} \\
&= \frac{\sum_{N_j} N_E^j n_2^j \left[C_2^j(\vec{p_1}, \vec{p_2}) + \rho_{2,mix}^j(\vec{p_1}, \vec{p_2})\right]}{\sum_{N_j} N_E^j n_2^j} - \frac{\sum_{n_{j,mix}} N_{E,mix}^j n_{2,mix}^j \rho_{2,mix}^j(\vec{p_1}, \vec{p_2})}{\sum_{n_{j,mix}} N_{E,mix}^j n_{2,mix}^j} \\
&= \frac{\overline{n_2^j C_2^j}}{\overline{n_2^j}} + \mathcal{C}' \qquad (3.6)
\end{aligned}$$

where the semi-inclusive correlation is defined as $C_2^j(\vec{p_1}, \vec{p_2}) \equiv \rho_2^j(\vec{p_1}, \vec{p_2}) - \rho_1^j(\vec{p_1})\rho_1^j(\vec{p_2})$ and $\mathcal{C}' = \frac{\sum_{N_j} N_E^j n_2^j \rho_{2,mix}^j}{\sum_{N_j} N_E^j n_2^j} - \frac{\sum_{n_{j,mix}} N_{E,mix}^j n_{2,mix}^j \rho_{2,mix}^j}{\sum_{n_{j,mix}} N_{E,mix}^j n_{2,mix}^j}$. The first term is the pair-number-weighted semi-inclusive correlation function averaged over the multiplicity class, and the second term $\mathcal{C}'$ is the contribution from the statistical reference distribution, which is negligible for the current study provided there is proper statistical reference construction: $C_2(\vec{p_1}, \vec{p_2}) \simeq \frac{\overline{n_2^j C_2^j(\vec{p_1}, \vec{p_2})}}{\overline{n_2^j}}$.

3.4 Multiplicity Dependence of Model Correlations

Inclusive correlation functions obtained from the different multiplicity classes are compared in a search of the correlation production/propagation mechanisms and their modifications with centrality variation of heavy ion collisions. For this purpose any trivial multiplicity dependencies of correlation function should be understood. Appropriate normalizations for the comparison of two-particle correlations from different multiplicity classes are considered in this section.

The correlation function defined in Eq. 3.3 reflects the ratio of pairs correlated within events, which can be observed by comparing correlation functions of given width and form in which all the pairs are correlated (C_2) and where a fraction f of pairs are correlated (C_2^f). In the latter case, the two-particle density ρ_2^f is written as the sum of the fraction f pairs which are different from the reference and the fraction $(1-f)$ of reference (uncorrelated) pairs. Thus,

$$
\begin{aligned}
C_2^f(\vec{p_1}, \vec{p_2}) &= \rho_2^f(\vec{p_1}, \vec{p_2}) - \rho_{2,mix}(\vec{p_1}, \vec{p_2}) \\
&= f\rho_2(\vec{p_1}, \vec{p_2}) + (1-f)\rho_{2,mix}(\vec{p_1}, \vec{p_2}) - \rho_{2,mix}(\vec{p_1}, \vec{p_2}) \\
&= fC_2(\vec{p_1}, \vec{p_2}), \qquad (3.7)
\end{aligned}
$$

we see that the amplitude of the correlation function is proportional to f corresponding to dilution by uncorrelated pairs.

However, considering the nature of correlations, it is natural to scale with the fraction of *particles* correlated in events rather than the fraction of correlated pairs, *i.e.* the amplitude should be proportional to the number of particles correlated with a test particle. As seen from the relation between fluctuation measurements and two-particle correlations (Eq. 3.16), the normalization is approximately obtained by multiplying the correlation function by the event multiplicity. Thus, the normalized two-particle density ratio assuming approximate factorization of correlation contents is written as $(\overline{N_j}-1)\ (R-1)$.

3.5 Fluctuations and Two-Particle Correlations

A way to examine the role of two-particle correlations in heavy ion collisions is to consider their relation to fluctuations of event-wise averages, namely mean-p_t fluctuations, which provided initial motivation to the study of two-particle correlation in transverse-momentum space.

Event-by-event fluctuation analysis of event-wise p_t average has been recognized as a sensitive tool to study the dynamics of heavy ion collisions

[15, 16, 26]. Theoretical models have predicted the behavior of nonstatistical fluctuations associated with the phase transition in heavy ion collisions, including enhancement *and* reduction of fluctuation due to the presence of critical phenomena associated with the phase transition, event-by-event fluctuation of equilibration process and the memory effect from the phase with partonic degrees of freedom in final state hadrons due to rapid expansion of the system [23, 24]. Given these possibilities of interesting physics, the collision energy/ion species and centrality (multiplicity) dependence of fluctuations become most important, with the expectation of observing irregular enhancement or reduction of fluctuations as functions of collision properties, and the search for sources of such non-statistical fluctuations.

There are several proposed observables to look for multiplicity or participant number dependencies of the dynamically-induced fluctuations [38–40]. Variable $\Delta\sigma^2_{p_t}$ was constructed as a p_t variance-difference measure to have the least contribution from multiplicity fluctuations in a set of events. It is suitable for careful study of event ensembles in which different numbers of particles are involved. For this reason $\Delta\sigma^2_{p_t}$ has been measured in the STAR experiment [41].

$\Delta\sigma^2_{p_t}$ measures $< p_t >$ variance beyond the statistically independent reference inferred from the central limit theorem (CLT) [39] and is defined by

$$\Delta\sigma^2_{p_t} = \overline{N_j \sigma^2_{<p_t>,j}} - \sigma^2_{\hat{p_t}}, \tag{3.8}$$

where event-wise mean of quantity a_{ji} of i_{th} particle over j_{th} event with multiplicity N_j denoted as $< a >_j$, an inclusive average written as $\hat{a}$ and an average of event-wise quantity a_j over given multiplicity class of the total number of N_E events, $\overline{a}$ are defined as,

$$
\begin{aligned}
< a >_j &\equiv \frac{1}{N_j} \sum_{i=1}^{N_j} a_{ji}, && (3.9) \\
\hat{a} &\equiv \frac{1}{\sum_{j=1}^{N_E} N_j} \sum_{j=1}^{N_E} \sum_{i=1}^{N_j} a_{ji}, && (3.10) \\
\overline{a} &\equiv \frac{1}{N_E} \sum_{j=1}^{N_E} a_j. && (3.11)
\end{aligned}
$$

Event-wise mean p_t variance of j_{th} event defined as $\sigma^2_{<p_t>,j} = (< p_t >_j -\hat{p}_t)^2$ and $\sigma^2_{\hat{p}_t}$ is the variance of inclusive p_t distribution.

By decomposing Eq. 3.8 by particle-wise quantities, the first term can be expressed as,

$$
\begin{aligned}
&\overline{N_j \sigma^2_{<p_t>,j}} \\
&= \frac{1}{N_E} \sum_{j=1}^{N_E} N_j (< p_t >_j -\hat{p}_t)^2 \\
&= \frac{1}{N_E} \sum_{j=1}^{N_E} \left[\frac{\sum_{i \neq l}^{N_j} p_{t,ji} p_{t,jl}}{N_j} + \frac{\sum_{i=1}^{N_j} p^2_{t,ji}}{N_j} - 2\hat{p}_t \sum_{i=1}^{N_j} p_{t,ji} + N_j \hat{p}_t{}^2 \right], \quad (3.12)
\end{aligned}
$$

and the inclusive variance in the second term is

$$
\begin{aligned}
\sigma^2_{\hat{p}_t} &= \frac{1}{\bar{n} N_E} \sum_{j=1}^{N_E} \sum_{i=1}^{N_j} (p_{t,ji} - \hat{p}_t)^2 \\
&= \hat{p^2_t} - \hat{p}_t{}^2. \quad (3.13)
\end{aligned}
$$

We get the differences as,

$$
\begin{aligned}
&\Delta\sigma^2_{p_t} \\
&= \frac{1}{N_E}\sum_{j=1}^{N_E}\left\{(N_j-1)\frac{\sum_{i\neq l}^{N_j} p_{t,ji}p_{t,jl}}{N_j(N_j-1)} + \left[< p_t^2 >_j - \hat{p_t^2}\right] + \left[(1+N_j)\hat{p_t}^2 - 2\hat{p}_t\sum_{i=1}^{N_j} p_{ji}\right]\right\} \\
&= \frac{1}{N_E}\sum_{j=1}^{N_E}\left\{\frac{(N_j-1)\sum_{i\neq l}^{N_j} p_{t,ji}p_{t,jl}}{N_j(N_j-1)} + \left[\delta < p_t^2 >_j\right] + \left[(1-N_j)\hat{p}_t - 2\hat{p}_t N_j \delta < p_t >_j\right]\right\} \\
&= \frac{1}{N_E}\sum_{j=1}^{N_E}\left\{(N_j-1)\left[< p_{t,i}\cdot p_{t,l} >_j - \hat{p_t}^2\right]\right\} \\
&= \overline{N_j - 1}\ \overline{\left[< p_{t,i}\cdot p_{t,l} >_j - \hat{p_t}^2\right]}.
\end{aligned}
\tag{3.14}
$$

Where δa_j is the event-wise deviation from inclusive mean $\delta a_j \equiv a_j - \hat{a}$ and $< p_{t,i} \cdot p_{t,l} >_j = \frac{\sum_{i\neq l}^{N_j} p_{t,ji}p_{t,jl}}{N_j(N_j-1)}$ denotes the pair-wise average of product of pair p_t in j_{th} event. From the second line to the third line, the linear term in δ which vanishes when average were taken is eliminated. In the last line, an approximate factorization is assumed.

In the continuum limit, the event-wise quantity inside square brackets in Eq. 3.14 can be expressed with an integral as,

$$
\begin{aligned}
&< p_{t,i}\cdot p_{t,l} >_j - \hat{p_t}^2 \\
&= \frac{\sum_{i\neq l}^{N_j} p_{t,ji}p_{t,jl}}{N_j(N_j-1)} - \left[\frac{\sum_{j=1}^{N_E}\sum_{i=1}^{N_j} p_{t,ji}}{\sum_{j=1}^{N_E} N_j}\right]^2 \\
&\simeq \int p_{t1}p_{t2}\left[\rho_2^j(p_{t1},p_{t2}) - \rho_1^j(p_{t1})\rho_1^j(p_{t2})\right] dp_{t1}dp_{t2},
\end{aligned}
\tag{3.15}
$$

and thus

$$
\Delta\sigma^2_{p_t} \simeq \overline{(N_j-1)}\ \overline{\int p_{t1}\ p_{t2}\ [\rho_2^j(p_{t1};p_{t2}) - \rho_{2,stat}^j(p_{t1};p_{t2})]\ dp_{t1}dp_{t2}}, \tag{3.16}
$$

where ρ_1^j, ρ_2^j and $\rho_{2,stat}^j$ are single-particle, two-particle and two-particle statistical reference probability distribution of j_{th} event with N_j multiplicity respectively. This relation shows that the mean p_t fluctuation measure $\Delta\sigma_{p_t}^2$ corresponds to the average of the two-particle transverse momentum integral, or in the other words, this two-particle analysis corresponds to the differential study of fluctuation measures.

The result of $< p_t >$ fluctuation study on its centrality dependence in the form of $\Delta\sigma_{p_t}^2$ divided by a factor of $2\sigma_{\hat{p}_t}$ has been obtained by Jeff Reid (University of Washington) [41, 42] at $\sqrt{s_{NN}} = 130$ GeV and shown in Fig. 3.2. The evidence for the existence of dynamical $< p_t >$ fluctuation beyond statistical CLT reference and its characteristic and smooth centrality dependence has been observed. With some sacrifice of the statistical power of fluctuation analysis, two-particle correlation analysis reveals a new dimension with the integral/differential relation to the fluctuation measure of Eq. 3.16 which provides for us further insights into the dynamics associated with nonstatistical fluctuation in heavy ion collisions.

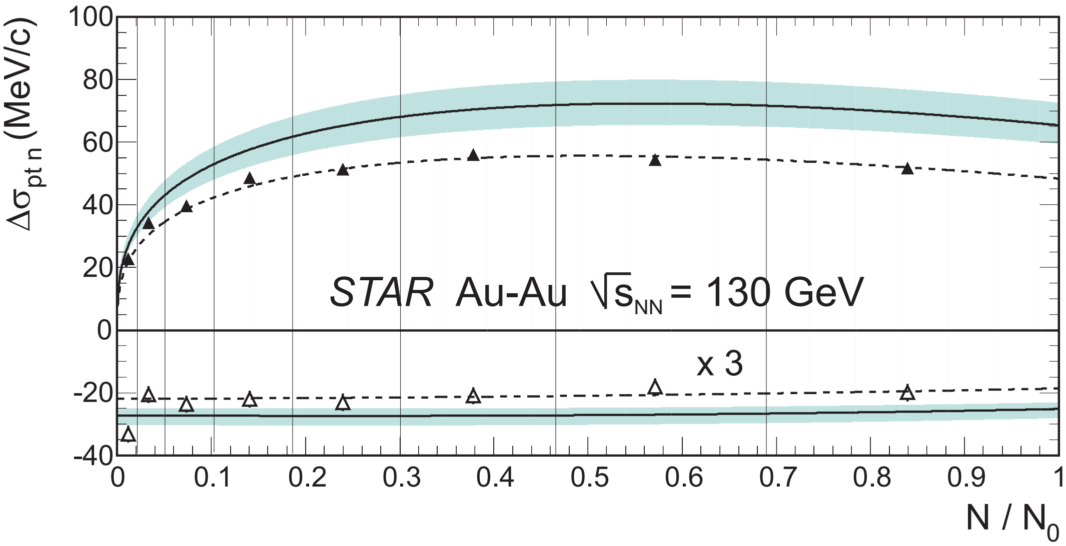

Figure 3.2: Centrality dependence of $\Delta\sigma_{p_t} = \frac{\Delta\sigma^2_{p_t}}{2\sigma_{\hat{p_t}}}$ at $\sqrt{s_{NN}}$ from [41, 42] are shown. The centrality is defined as the ratio of event multiplicities and the endpoint multiplicity N_0. The detail of analysis can be found in the references. The closed triangle shows the non-statistical fluctuation of all the charged particles (charge-independent). Charge-dependent fluctuation contributions multiplied by 3 for clarity are shown as open points. Quantities with background correction and extrapolation to 100% tracking efficiency are represented by solid lines with ±12% systematic uncertainties and statistical error distribution shown as bands discussed in the references. Smooth but non-monotonic increase of charge-independent fluctuations with centrality are observed. Charge-dependent contribution exhibits approximate constant behavior with centrality.

Chapter 4

Expected Sources of Correlations

There are several expected sources of large-momentum-scale two-particle correlations in relativistic heavy ion collisions. These correlations may appear as modifications of correlations observed in p-p collisions or as specific to heavy ion collisions. Correlation structure in elementary collisions suggests the asymptotic behavior to be expected in very peripheral heavy ion collisions and provides a reference model in search of the characteristic behavior in more central heavy ion collisions. Some of the correlation structure expected to appear in heavy ion two-particle momentum spaces relevant to this study are described in this chapter. The large-momentum-scale two-particle correlation structures we observe in Au-Au collisions are quantitatively described with these models in Chapters 6 - 8.

4.1 Temperature Fluctuations in Transverse-Momentum Space

High temperature corresponds to some characteristic energy is considered to be one of the most essential conditions for the existence of a phase transition. Thus, (at least local) temperature equilibrium is assumed in most heavy ion collision models which involve a color-deconfined phase. Because the degree of achieved equilibrium is not directly observable, the expected degree depends on assumptions made in each model.

In this section, we consider a two-particle transverse-momentum distribution in the generic case that particles are emitted from small spacial regions in local equilibrium but that (local) temperatures may fluctuate from point to point in each collision (local fluctuations) and/or from event to event (global fluctuations). The case that each event is fully equilibrated but the mean temperature varies event by event is treated as a limiting case. The assumed temperature distribution model in this section, with local or global temperature fluctuations, follows a generic Langevin equation and is represented by gamma distribution. In this model, the experimentally observed power-law or the Lévy single-particle p_t distribution is derived from the Maxwell-Boltzmann distribution by folding with the gamma temperature distribution. The temperature distribution is also represented in a two-particle space by assuming two-point temperature correlation models, and the two-point temperature distribution is then reflected in the two-particle transverse momentum space. Comparison with a hypothetical model of two-particle transverse momentum correlations arising from event local/global temperature fluctuations and experimentally observed data may give insight into the equilibration process in heavy ion collisions, and thus may test the applicability of equilibrium models. It should be noted that for the present study with unidentified charged particles, the 'temperature' discussed in this section includes not only thermal random motion but also contributions from collective motion of particles, both of which may fluctuate locally and/or globally.

The assumption of thermodynamical equilibrium in heavy ion collisions is based on the fact that single-particle distributions are approximately described by Maxwell-Boltzmann (MB) distributions in the soft-p_t region. However, with recent observations of deviations from equilibrium expectations such as nonstatistical fluctuations [41] and mixing of soft and hard particle distributions [43], it is natural to consider that some degree of temperature variation exists in a set of heavy ion collisions at the RHIC energy. Thus, we consider the possible form of temperature fluctuations included in single-particle distributions based on the generic Langevin equation [44] describing stochastic temperature variable T with mean temperature $\overline{T}$. The equation describes temperature variation of a small selected region next to a large heat bath and is represented by

$$\frac{dT}{dt} = -\frac{T}{\kappa} - \xi(t)T + \frac{\overline{T}}{\kappa}, \tag{4.1}$$

where $\xi(t)$ is a random gaussian white noise defined by $< \xi(t) >= 0$ and $< \xi(t)\xi(t + \Delta t) >= 2D\delta(\Delta t)$. Coefficient D is a constant which indicates the amplitude of the random noise and κ is a damping constant. The Langevin eq. (Eq. 4.1) is different from the Langevin equation of Brownian motion in that (1) the noise from random temperature fluctuations, the second term in the right-hand side, is proportional to the temperature itself and (2) there is a constant source term $\overline{T}/\kappa$.

4.1.1 Single-Point Temperature Distributions

The single-point temperature probability distribution function (pdf) τ which satisfies Eq. 4.1 is represented by a gamma distribution g of inverse-temperature $\beta = 1/T$ as,

$$\tau(\beta; \overline{\beta}, n) = g(\beta; \overline{\beta}, n) \equiv \frac{n}{\overline{\beta}\Gamma(n)} (\frac{n\beta}{\overline{\beta}})^{n-1} e^{-n\frac{\beta}{\overline{\beta}}}, \tag{4.2}$$

where $\overline{\beta} = 1/\overline{T}$ denotes the mean inverse-temperature and $n = 1/\kappa D$. $\tau(\beta)$ denotes the general form of temperature distributions and $g(\beta)$ denotes a gamma-function model temperature distribution. With the normalization $\int_0^\infty g(\beta; \beta_0, n) d\beta = 1$, the relative variance is related to n by

$$\frac{\sigma_\beta^2}{\overline{\beta}^2} = \frac{< (\beta - \overline{\beta})^2 >}{\overline{\beta}^2} = \frac{1}{n}. \tag{4.3}$$

The finite-width temperature pdf (Eq. 4.2) results in a modification of the inclusive single-particle MB distribution of a static thermal source as,

$$\begin{aligned} \frac{1}{m_t}\frac{dN(m_t)}{dm_t} &= B \int_0^\infty g(\beta; \overline{\beta}, n) \; e^{-\beta m_t} d\beta \\ &= \frac{B}{(1 + \frac{\overline{\beta}}{n})^n} = F_{Lévy}(m_t; \overline{\beta}, n). \end{aligned} \tag{4.4}$$

The inclusive single-particle distribution with relative temperature variance $1/n$ is written as a Lévy distribution $F_{Lévy}(m_t; \overline{\beta}, n)$ and the non-zero variance may arise from local and/or event-wise temperature fluctuations. For the case of $\frac{1}{n} \to 0$, $g(\beta; \overline{\beta}, \infty) = \delta(\beta - \overline{\beta})$, and the Lévy distribution (Eq. 4.4) becomes the MB exponential distribution.

It has been observed that the Lévy distribution gives good agreement with the single-particle p_t distribution in the heavy ion collisions [45]. Most of the difference between the MB and data distribution is in general considered to be due to a mixture of collective radial motion of particles and particles originating from semi-hard scattering. However, the fraction of contribution arising from difference sources is still an open question. It relates to an essential question of heavy ion physics, the relation between single-point temperature distribution $\tau(\beta)$ and inverse-temperature parameter $\beta \equiv 1/T$. In the following, given the assumed single-point gamma temperature distribution $\tau(\beta) = g(\beta)$, two-point temperature distributions are considered.

4.1.2 Two-Point Temperature Distributions

The concept of temperature distribution is also applicable in a two-particle space. For the simplest case, the *two-point temperature distribution* τ_2 of a statistical reference or a factorized distribution is written as a product of two single-point temperature distributions (Eq. 4.2) as,

$$\tau_{2,stat}(\beta_1, \beta_2; \overline{\beta}, n) = \tau(\beta_1; \overline{\beta}, n) \cdot \tau(\beta_2; \overline{\beta}, n). \tag{4.5}$$

The non-factorized two-point temperature distribution $\tau_2(\beta_1, \beta_2; \overline{\beta}, n'(\Delta e), n(\Sigma e))$ for a set of events characterized by inclusive mean inverse temperature $\overline{\beta}$, local-temperature-fluctuation parameter $n'(\Delta e)$ and global-temperature-fluctuation parameter $n(\Sigma e)$, may be expressed similly to a single-particle distribution (Eq. 4.2) by two-point temperature distribution of which local inverse-temperature

β_0 weighted by a mean temperature distribution $\tau(\beta_0)$ as,

$$\begin{aligned} & \tau_2(\beta_1, \beta_2; \overline{\beta}, n'(\Delta e), n(\Sigma e)) \\ & \quad = \int \tau_2(\beta_1, \beta_2; \beta_0, n'(\Delta e)) \cdot \tau(\beta_0; \overline{\beta}, n(\Sigma e)) \, d\beta_0, \end{aligned} \tag{4.6}$$

where Δe denotes the size of one event with defined acceptance and Σe indicates an event ensemble. $n'(\Delta e)$ and $n(\Sigma e)$ denote variance parameters belonging to the different scales and are related to the inverses of relative variance at the two scales. The two-point temperature distribution for each event $\tau_2(\beta_1, \beta_2; \beta_0, n'(\Delta e))$ is represented by the local mean inverse-temperature β_0 and event-internal variance parameter $n'(\Delta e)$. $\tau(\beta_0; \overline{\beta}, n(\Sigma e))$ indicates the distribution of event-wise mean temperatures.

The event-wise two-point temperature distribution $\tau_2(\beta_1, \beta_2; \beta_0, n'(\Delta e))$ may be expressed as a combination of uncorrelated and correlated two-point temperature distributions. The former, $\tau_{2,uncorr}$, is expressed as a simple product of the single-particle event-internal temperature distributions according to a factorization assumption,

$$\tau_{2,uncorr}(\beta_1, \beta_2; \beta_0, n'(\Delta e)) \;\; = \;\; \tau(\beta_1; \beta_0, n'(\Delta e)) \cdot \tau(\beta_2; \beta_0, n'(\Delta e)). \tag{4.7}$$

The model for the uncorrelated event-internal two-point temperature distribution is obtained by inserting the gamma pdf (Eq. 4.2) for the single-point temperature distributions in Eq. 4.7 as,

$$\begin{aligned}
&\tau_{2,uncorr}(\beta_1,\beta_2;\beta_0,n') = g(\beta_1;\beta_0,n')\cdot g(\beta_2;\beta_0,n') \\
&= (\frac{n'}{\beta_0\Gamma(n')})^2(\frac{n'^2\beta_1\beta_2}{\beta_0^2})^{n'-1}e^{-\frac{n'}{\beta_0}(\beta_1+\beta_2)} \\
&= \left[(\frac{2n'}{\beta_0\Gamma(2n')})(\frac{n'\beta_\Sigma}{\beta_0})^{2n'-1}e^{-\frac{n'\beta_\Sigma}{\beta_0}}\right]\cdot\frac{\Gamma(2n')}{2^{2n'-1}\Gamma(n')^2}\frac{1}{\beta_\Sigma}(1-\frac{\beta_\Delta^2}{\beta_\Sigma^2})^{n'-1} \\
&\equiv g(\beta_\Sigma;2\beta_0,2n')\cdot f(\beta_\Delta;\beta_\Sigma,n'),
\end{aligned} \tag{4.8}$$

where $n' \equiv n'(\Delta e)$ and $\beta_\Sigma \equiv \beta_1+\beta_2$, $\beta_\Delta \equiv \beta_1-\beta_2$ are the sum and difference of two-point temperatures. $g(\beta_\Sigma;2\beta_0,2n')$ is a 2-fold convolution of the gamma pdf with mean β_0 and variance parameter n' which is simply the gamma pdf of β_Σ with mean $2\beta_0$ and variance parameter $2n'$, and $f(\beta_\Delta;\beta_\Sigma,n') \equiv \frac{\Gamma(2n')}{2^{2n'-1}\Gamma(n')^2}\frac{1}{\beta_\Sigma}(1-\frac{\beta_\Delta^2}{\beta_\Sigma^2})^{n'-1}$. These distributions are normalized as $\int_{-\beta_\Sigma}^{\beta_\Sigma} f(\beta_\Delta;\beta_\Sigma,n')d\beta_\Delta = 1$ and $\int_0^\infty g(\beta_\Sigma;2\beta_0,2n')d\beta_\Sigma = 2$. The inclusive two-point temperature distribution (Eq. 4.6) is then written as,

$$\begin{aligned}
&\tau_2(\beta_1,\beta_2;\overline{\beta},n'(\Delta e),n(\Sigma e)) \\
&= \left[\int g(\beta_\Sigma;2\beta_0,2n')\cdot g(\beta_0;\overline{\beta},n(\Sigma e))d\beta_0\right]\cdot f(\beta_\Delta;\beta_\Sigma,n') \\
&\simeq g(\beta_\Sigma;2\overline{\beta},2n_\Sigma)\cdot f(\beta_\Delta;\beta_\Sigma,n'),
\end{aligned} \tag{4.9}$$

where from second to third line the integral inside the square brackets is approximated as a gamma pdf with a new variance parameter n_Σ which includes the contribution from both event-internal and event-wise temperature fluctuations as

$$g(\beta_\Sigma;2\overline{\beta},2n_\Sigma) \simeq \int g(\beta_\Sigma;2\beta_0,2n')\cdot g(\beta_0;\overline{\beta},n(\Sigma e))d\beta_0. \tag{4.10}$$

This result may be compared with the case of the single-point temperature distribution in which both event-internal temperature fluctuation parameter $n'(\Delta e)$ and event-wise temperature fluctuation parameter $n(\Sigma e)$ are reflected in the single-particle inclusive temperature fluctuation parameter n as

$$g(\beta;\overline{\beta},n) \simeq \int g(\beta;\beta_0,n'(\Delta e)) \cdot g(\beta_0;\overline{\beta},n(\Sigma e))d\beta_0. \tag{4.11}$$

Note that $f(\beta_\Delta;\beta_\Sigma,n')$ in Eq. 4.9 only reflects the event-internal two-point temperature distribution and is thus independent of the event-wise mean-temperature distribution.

4.1.3 Modeling Event-Internal Temperature Structure

Similarly the case of a distribution with event-internal or local temperature correlations is considered by picturing an event in which there are several subsets of particles, and the particles within each subset are uncorrelated, *i.e.*, the two-point temperature distribution of a single subset can be expressed similar to Eq. 4.7, except $n' \to n_\Delta$, where n_Δ represent the variance parameter belonging to that subset. For local temperature fluctuations which are fluctuations of the mean temperatures of each subset, of size $1/n_\Sigma(\Delta e)$, the two-point temperature distribution of single event can be written as for Eq. 4.9,

$$\tau_2(\beta_1,\beta_2;\beta_0,n_\Delta,n'_\Sigma) \equiv g(\beta_\Sigma;2\beta_0,2n'_\Sigma) \cdot f(\beta_\Delta;\beta_\Sigma,n_\Delta), \tag{4.12}$$

where n'_Σ is related to n_Δ and n_Σ by

$$g(\beta_\Sigma;2\beta_0,2n'_\Sigma) \simeq \int g(\beta_\Sigma;2\beta'_0,2n_\Delta) \cdot g(\beta'_0;\beta_0,n_\Sigma(\Delta e))d\beta'_0. \tag{4.13}$$

In this case, $1/n_\Delta$ denotes the size of fluctuations of subsets in which particles are minimally correlated (or expressed by a factorized distribution). It indicates that for the extreme case $\frac{1}{n_\Delta} \to 0$, *i.e.*, the number of subsets in a single event equals the event multiplicity, the two-point temperature distribution is maximally correlated. For the case $n_\Delta = n'$ the number of subsets in single event equals 1, indicate two-point temperature is minimally correlated in each event. The inclusive two-point temperature distribution of Eq. 4.9 and 4.10 are changed to include the event-internal temperature correlation by replacing $n' \to n_\Delta$ and n_Σ giving $g(\beta_\Sigma; 2\overline{\beta}, 2n_\Sigma) \equiv \int\int g(\beta_\Sigma; 2\beta_0', 2n_\Delta) \cdot g(\beta_0'; \beta_0, n_\Sigma(\Delta e)) \cdot g(\beta_0; \overline{\beta}, n(\Sigma e)) d\beta_0 d\beta_0'$. The final expression of a two-point temperature distribution which includes local and global temperature fluctuations, and local temperature correlations is obtained as,

$$\tau_2(\beta_1, \beta_2; \overline{\beta}, n_\Delta, n_\Sigma) = g(\beta_\Sigma; 2\overline{\beta}, 2n_\Sigma) \cdot f(\beta_\Delta; \beta_\Sigma, n_\Delta), \tag{4.14}$$

a product of a gamma distribution g of β_Σ and a function $f(\beta_\Delta; \beta_\Sigma, n_\Delta) \equiv \frac{\Gamma(2n_\Delta)}{2^{2n_\Delta - 1}\Gamma(n_\Delta)^2} \frac{1}{\beta_\Sigma}(1 - \frac{\beta_\Delta^2}{\beta_\Sigma^2})^{n_\Delta - 1}$. Note that n_Σ includes contributions from event-internal and event-wise temperature fluctuations, and n_Δ includes contributions only from event-internal temperature fluctuations.

4.1.4 Two-Particle p_t Distributions

The structure of two-point temperature distributions has been discussed so far; however the temperature itself is not direct observable. In the following, the manifestation of two-point temperature distributions in two-particle transverse momentum space is considered.

Information about temperature distributions in heavy ion collisions is obtained through the relation between the inverse-slope parameter in the observed m_t or p_t distribution and the temperature parameter in the MB distribution. In other words, the temperature distribution $\tau(\beta; n)$ may be obtained as a function which describes experimentally-obtained single-particle distribution $\rho(m_t; n) \equiv \frac{1}{m_t}\frac{dN(m_t)}{dm_t}$ similar to Eq. 4.4 as,

$$\rho(m_t; n) = \int_0^\infty \tau(\beta; n)\ \rho(m_t; \beta)\ d\beta. \tag{4.15}$$

where $\rho(m_t; \beta)$ is the MB m_t distribution with a given temperature β. Similarly, in two-particle spaces the observed two-particle transverse-mass distribution $\rho_2(m_{t1}, m_{t2}; n_\Delta, n_\Sigma)$ and two-point temperature distribution $\tau_2(\beta_1, \beta_2; n_\Delta, n_\Sigma)$ can be related as,

$$\begin{aligned} &\rho_2(m_{t1}, m_{t2}; n_\Delta, n_\Sigma) \\ &= \int_0^\infty \tau_2(\beta_1, \beta_2; n_\Delta, n_\Sigma)\rho_2(m_{t1}, m_{t2}; \beta_1, \beta_2) d\beta_1 d\beta_2, \end{aligned} \tag{4.16}$$

where $\rho_2(m_{t1}, m_{t2}; \beta_1, \beta_2)$ is the uncorrelated two-particle m_t distribution with given temperatures β_1 and β_2 written as a product of two MB distributions $\rho_2(m_{t1}, m_{t2}; \beta_1, \beta_2) = e^{-\beta_1 m_{t1}} e^{-\beta_2 m_{t2}} = e^{-\frac{m_{t\Sigma}\beta_\Sigma + m_{t\Delta}\beta_\Delta}{2}}$, with the difference and sum of pair transverse mass variables $m_{t\Delta} \equiv m_1 - m_2$ and $m_{t\Delta} \equiv m_{t1} + m_{t2} - (m_1 + m_2)$, and m_1 and m_2 indicating the mass of particles to which the pion mass is assigned in this study.

By inserting the two-point temperature distributions from Eq. 4.9 and the statistical reference from Eq. 4.5 into Eq. 4.16 as two-point temperature model distributions we obtain final representations of two-particle m_t distributions which include event local/global temperature fluctuations. For pairs correlated through two-point temperature distributions, the two-particle m_t distribution is then expressed as

$$
\begin{aligned}
&\rho_2(m_{t1}, m_{t2}; \overline{\beta}, n_\Delta, n_\Sigma) \\
&= \int_0^\infty d\beta_\Sigma \int_{-\beta_\Sigma}^{\beta_\Sigma} d\beta_\Delta \Big[\tau_2(\beta_\Sigma, \beta_\Delta; \overline{\beta}, n_\Delta, n_\Sigma)\; e^{-\frac{m_{t\Sigma}\beta_\Sigma + m_{t\Delta}\beta_\Delta}{2}}\Big] \\
&= \int_0^\infty d\beta_\Sigma\; g(\beta_\Sigma; 2\overline{\beta}, 2n_\Sigma)\; e^{-\frac{m_{t\Sigma}\beta_\Sigma}{2}} \int_{-\beta_\Sigma}^{\beta_\Sigma} d\beta_\Delta f(\beta_\Delta; n_\Delta)\; e^{-\frac{m_{t\Delta}\beta_\Delta}{2}} \\
&= \frac{1}{(1+\frac{\overline{\beta}m_{t\Sigma}}{2n_\Sigma})^{2n_\Sigma}} \frac{\Gamma(2n_\Delta)}{\Gamma(2n_\Sigma)} \frac{1}{\Gamma^2(n_\Delta)2^{2n_\Delta-1}} \int_0^\infty dt t^{2n_\Sigma-1} e^{-t} \int_{-1}^{1} dx (1-x^2)^{n_\Delta-1} e^{-(\frac{\overline{\beta}m_{t\Delta}}{2n_\Sigma+\overline{\beta}m_{t\Sigma}})tx} \\
&= \frac{1}{(1+\frac{\overline{\beta}m_{t\Sigma}}{2n_\Sigma})^{2n_\Sigma}} \sum_{a=0}^{\infty} \left(\frac{\Gamma(2n_\Sigma+2a)}{\Gamma(2n_\Delta+2a)}\right) \left(\frac{(n_\Delta+a-1)!}{(n_\Delta-1)!}\right) \frac{(\frac{\overline{\beta}m_{t\Delta}}{2n_\Sigma+\overline{\beta}m_{t\Sigma}})^{2a}}{a!} \\
&\simeq \frac{1}{(1+\frac{\overline{\beta}m_{t\Sigma}}{2n_\Sigma})^{2n_\Sigma}} \frac{1}{(1-(\frac{\overline{\beta}m_{t\Delta}}{2n_\Delta+\overline{\beta}m_{t\Sigma}})^2)^{n_\Delta}},
\end{aligned} \tag{4.17}
$$

and the statistical reference distribution is written as

$$
\begin{aligned}
&\rho_{2,stat}(m_{t1}, m_{t2}; \overline{\beta}, n) \\
&= \int_0^\infty d\beta_1\; g(\beta_1; n) \int_0^\infty d\beta_2\; g(\beta_2; n)\; e^{-\beta_1 m_{t2} - \beta_2 m_{t2}} \\
&= \frac{1}{(1+\frac{\overline{\beta}m_{t1}}{n})^n (1+\frac{\overline{\beta}m_{t2}}{n})^n} \\
&= \int_0^\infty d\beta_\Sigma \left[g(\beta_\Sigma; 2\overline{\beta}, 2n)\; e^{-\frac{m_{t\Sigma}\beta_\Sigma}{2}} \left(\int_{-\beta_\Sigma}^{\beta_\Sigma} d\beta_\Delta\; \tau(\Delta_\beta; \beta_\Sigma, n)\;\; e^{-\frac{m_{t\Delta}\beta_\Delta}{2}}\right)\right] \\
&= \frac{1}{(1+\frac{\overline{\beta}m_{t\Sigma}}{2n})^{2n}} \sum_{a=0}^{\infty} \frac{(n+a-1)!}{(n-1)!} \frac{(\frac{\overline{\beta}m_{t\Delta}}{2n+\overline{\beta}m_{t\Sigma}})^{2a}}{a!} \\
&= \frac{1}{(1+\frac{\overline{\beta}m_{t\Sigma}}{2n})^{2n}} \frac{1}{(1-(\frac{\overline{\beta}m_{t\Delta}}{2n+\overline{\beta}m_{t\Sigma}})^2)^n}.
\end{aligned} \tag{4.18}
$$

Approximation $\sum_{a=0}^{\infty} \left(\frac{\Gamma(2n_\Sigma+2a)}{\Gamma(2n_\Delta+2a)}\right) \left(\frac{(n_\Delta+a-1)!}{(n_\Delta-1)!}\right) \frac{(\frac{\overline{\beta} m_{t\Delta}}{2n_\Sigma+\overline{\beta} m_{t\Sigma}})^{2a}}{a!} \simeq 1/(1-(\frac{\overline{\beta} m_{t\Delta}}{2n_\Delta+\overline{\beta} m_{t\Sigma}})^2)^{n_\Delta}$ is used to obtain the last line of Eq. 4.17, which is constructed such that the curvatures along difference and sum variable axes are expressed by the two parameters n_Δ and n_Σ.

We will make use of this model for parameterizations of data from heavy ion collisions (Chap. 6), with the relations between temperature fluctuations and parameters n_Δ, n_Σ and n which characterize fluctuations at different scales (Eq. 4.3). Results are summarized with two observables of relative variance differences, $\Delta(1/n)_\Delta \equiv (\frac{1}{n_\Delta} - \frac{1}{n})$ and $\Delta(1/n)_\Sigma \equiv (\frac{1}{n_\Sigma} - \frac{1}{n})$ and a covariance parameter $\Delta(1/n)_{tot} \equiv (\frac{1}{n_\Sigma} - \frac{1}{n_\Delta})$. The variance differences measure the curvatures on the two-particle transverse momentum space in m_Δ and m_Σ directions, which is seen from the lower-order approximation for small variables by expanding the correlation function model $C_2 = \rho_2 - \rho_{2,stat}$ with Eq. 4.17 and 4.18 as, $C_2(m_\Sigma = 0, m_\Delta \sim 0) \simeq 1 + \frac{1}{4}\Delta(1/n)_\Delta\ m_\Delta^2$ and $C_2(m_\Delta = 0, m_\Sigma \sim 0) \simeq 1 + \frac{1}{4}\Delta(1/n)_\Sigma\ m_\Sigma^2$.

With the concept of two-point temperature distributions, each variance difference carries information about temperature distributions, for example: (1) $\Delta(1/n)_\Delta$ is not dependent on event-by-event global temperature fluctuations but depends only on the size of fluctuations of a subset of particles for which the two-point temperature distribution is expressed as a factorization. Fluctuations could depend on the statistical properties of matter such as pressure, spacial volume of subsets, energy density, chemical composition or the heat capacity of matter. However, such concepts may not be applicable in this case because the number of particles in each event is not sufficiently large and other statistical conditions are unknown. (2) $\Delta(1/n)_\Sigma$ includes contributions from both local and global temperature fluctuations. If there are no global temperature fluctuations nor event-internal temperature correlations $n_\Sigma \rightarrow n_\Delta$. Thus, (3) $\Delta(1/n)_{tot}$, the covariance of two-point temperature distributions on sum (average) and difference directions measures deviations from statistical equilibrium models in which neither global temperature fluctuations nor event-internal temperature correlations are included.

4.2 Color-String Fragmentation — Charge Ordering and Local Momentum Conservation on Axial-Momentum Space

Two-particle correlations among particles created in elementary collisions have been studied and well described by phenomenological models. Such models serve as references for two-particle correlation structure in heavy ion collisions. They describe the expected asymptotic behavior of two-particle correlations in the most peripheral heavy ion collisions or the form of two-particle correlations in the case that A-A collisions are merely superpositions of N-N collisions.

Two-particle correlations for axial momentum variables (η, ϕ) in p-p collisions were studied for like-sign (LS) and unlike-sign (US) charged-pairs as well as charge independent (CI = like-sign + unlike-sign) pairs [46–52]. The CI two-particle correlations in light-nucleus collisions [53] or in heavy ion

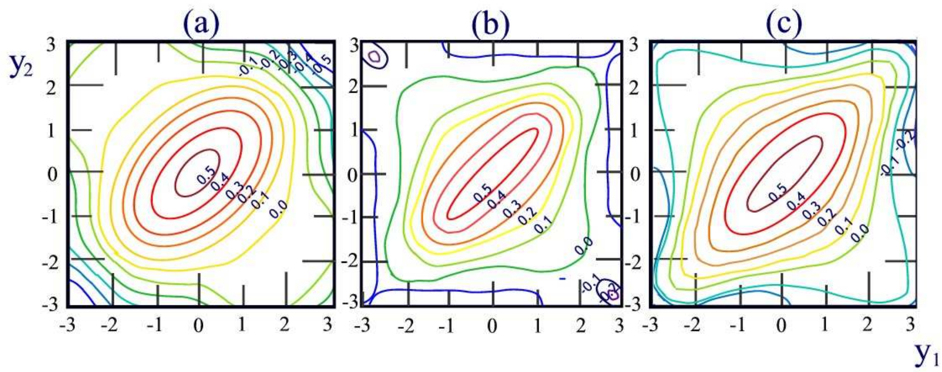

Figure 4.1: Charge-independent rapidity two-particle correlations in p-p collisions from Ref. [46] (a, c) and Ref. [48] (b) at FNAL. The beam momenta are (a) 100 GeV/c, (b) 205 GeV/c and (c) 400 GeV/c ($\sqrt{s} \sim 10$, 14 and 20 GeV respectively).

collisions at lower energies [54] also exhibited similar correlation structures to those in p-p collisions.

The most prominent feature of the two-particle correlation structure observed in p-p collisions is the large-momentum-scale correlation (LSC) of (pseudo-)rapidity differences as shown in the form of two-particle density ratio $R = \frac{\rho(y_1,y_2)}{\rho_{stat}(y_1,y_2)} - 1$ (described in Sec. 3.1) for three different collision energies in Fig. 4.1. The LSC are approximately described as functions of rapidity difference $y_\Delta \equiv y_1 - y_2$. The amplitude and shape of the correlations have small dependence on the collision energy, except that the shape is more extended along the sum diagonal at higher energies. Separate correlation structures for LS ($++$ and $--$) and US ($+-$ and $-+$) charge-pair combinations are shown in Fig. 4.2. LSC correlations are clearly observed for US pairs; small-momentum-scale correlations (SSC) with correlation length shorter than for

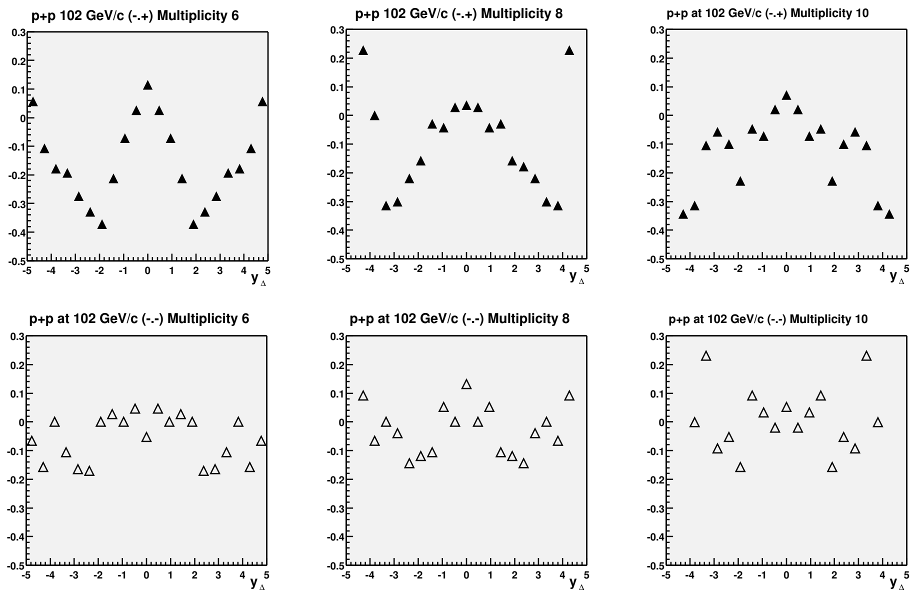

Figure 4.2: Multiplicity dependence of unlike-sign ($-.+$, upper panels) and like-sign ($-.-$, lower panels) rapidity autocorrelations from p-p collisions at beam momentum 102 GeV/c ($\sqrt{s} \sim 10$ GeV). Data points are taken from Ref. [46] at FNAL. Large-momentum-scale correlations on y_Δ are observed for the unlike-sign pairs.

US pairs are also observed in LS pairs. The SSC were interpreted as due to quantum statistics (Bose-Einstein correlation). The LSC unlike-sign rapidity correlations are described by a model in which the clusters decay into two or more particles and interpreted as a consequence of local measure (charge) conservation of the clusters or the 1-D string system along the beam-axis [55, 56].

This description is confirmed by observations made of two-particle η_Δ and ϕ_Δ joint autocorrelations in p-p collisions (Fig. 4.3). The study of azimuth angle dependence of the correlation structure showed that unlike-sign two-

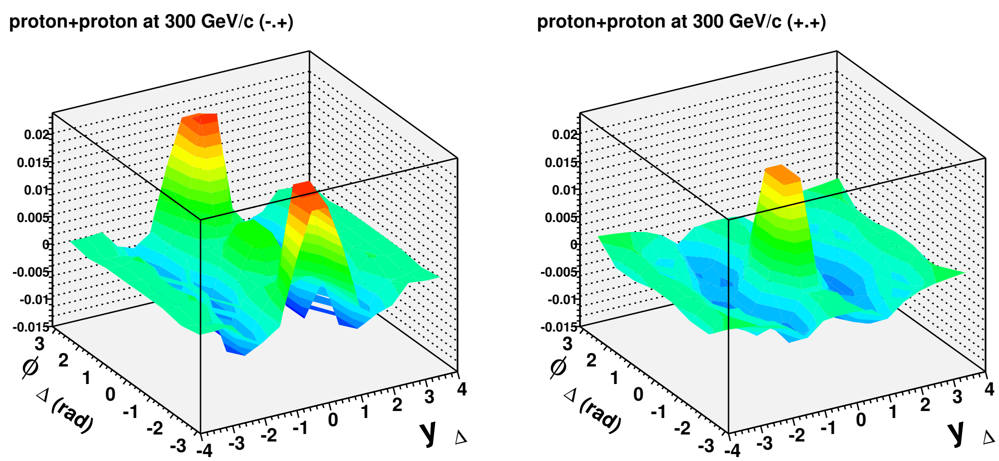

Figure 4.3: Two-particle joint autocorrelation on $y_\Delta \otimes \phi_\Delta$ from p-p collisions at beam momentum 300 GeV/c at FNAL. Plots are recreated using the data points in Ref. [47], for unlike-sign pair $(-.+)$ (left panel) and like-sign pair $(+.+)$ (right panel)

particle correlations can be decomposed into an away-side peak at $\phi_\Delta \approx \pi$ and a near-side component with peak at $|\phi_\Delta| \approx 0$. The former structure is due to momentum conservation, and latter is described by a model that clusters are decaying along η_Δ. That model, representing local charge conservation, describes the inclination to find unlike-sign charged particles close together on η (or z) and is referred to as the string charge-ordering model.

If heavy ion collisions were merely superpositions of p-p collisions, similar correlation structure from color strings decaying along the beam direction and distributed over a space is expected. In other words, deviations of the two-particle correlation structure in heavy ion collisions from p-p charge-ordering models indicate the existence of dynamical mechanisms which modify the correlation structure in heavy ion collisions, and which are the object of this study. Expected sources of deviations are for example large-amplitude collective flows (radial, longitudinal Bjorken expansion or azimuthally anisotropic collective motion), incomplete integration of conserved quantities (energy-momentum, charge), initial-state multiple scattering, hadronization geometry and/or the color-string melting in the bulk medium of high energy-density matter, all of which make heavy ion collisions very interesting. Identification and characterization of these mechanisms requires the careful study of two-particle correlation structures, with emphasis on centrality and scale dependencies.

4.3 Anisotropic Flow and Charge-Independent Axial-Momentum Correlations

In heavy ion collisions the incident nuclei have relatively large cross sections compare to elementary particles and there is a variation of the impact parameter $\vec{b}$ defined by the relative transverse positions of the colliding nuclei (Fig. 4.4). In events with non-zero impact parameter (non-central events), it has been observed that anisotropy of the initial collision geometry leads to event-by-event anisotropic final-state particle distributions on azimuth angle ϕ. The anisotropic particle distribution is often parameterized by Fourier coefficients v_n of the relative azimuth angle with respect to the reaction-plane angle Ψ defined by the vector angle of impact parameter $\vec{b}$, as shown in Fig. 4.4. The single particle azimuthal distribution is then expressed as,

$$\rho(\phi;\Psi) \propto 1 + \sum_{n=1}^{\infty} 2v_n cos(n(\phi - \Psi)). \tag{4.19}$$

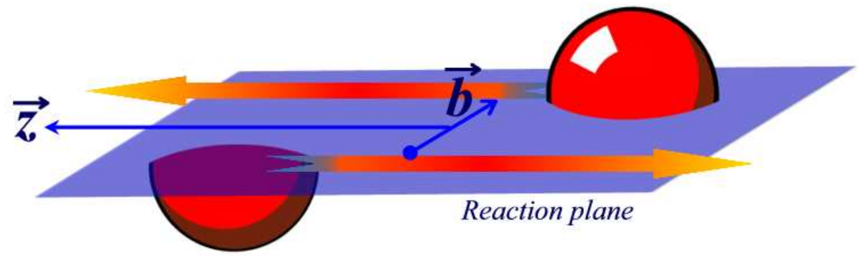

Figure 4.4: Impact parameter, overlap region and reaction plane.

The second harmonic coefficient v_2, often called elliptic flow coefficient, is the dominant component in Au-Au collisions and has been measured by several experiments at RHIC energies [57–60]. In the two-particle azimuth correlation space v_2 structure due to event-wise variation of the impact parameter is observed as a function of the two-particle azimuthal difference $\phi_\Delta \equiv \phi_1 - \phi_2$ as

$$\begin{aligned}\rho_{v_2}(\phi_1, \phi_2) &= \int_{\pi}^{-\pi} [1 + 2v_2 cos(2(\phi_1 - \Psi))][1 + 2v_2 cos(2(\phi_2 - \Psi))] d\Psi \\ &= 1 + 2v_2^2 cos(2(\phi_1 - \phi_2)). \qquad (4.20)\end{aligned}$$

The second-harmonic coefficient v_2 carries information about heavy ion collision dynamics because the conversion of initial-state geometrical anisotropy to final-state momentum anisotropy involves multiple scattering early in the collision. The relation between measured v_2 and the equation of state at early times has been extensively discussed. The increased v_2 values at RHIC compared to lower-energy collisions are believed to indicate the increased applicability of hydrodynamical models at RHIC [61]. However, the dynamical mechanism of two-particle correlations contributing to v_2 as measured only by projection onto azimuth angle is still unclear. For a better understanding of two-particle azimuth correlations explicit study of the charge-independent and charge-dependent *joint* autocorrelations of axial momentum difference variables, ϕ_Δ and η_Δ, is expected to play a major role, because a mixture of correlations from different origin in the two-particle correlation space is expected, and the distinction and characterization of each correlation mechanism requires new dimension in the correlation analysis.

4.4 Mini-jet Production and Charge-Independent Axial-Momentum Correlations

Particle production associated with parton scattering with large momentum-transfer (high-p_t hard-process) has been observed in elementary collisions. The cross-sections and high-p_t part of single-particle spectra are described by models based on perturbative QCD (pQCD) [2, 12, 13]. In Au-Au collisions partons, dynamical constituents of nucleons in incident nucleon beams, experience initial hard-scatterings which are expected to be similar to those in elementary collisions and should also produce high-p_t scattered partons. Each high-p_t parton then fragments to a cluster of particles, with average momentum expected to be higher than that of soft particles (string fragments). Correlated hadron groups (jets) produced in the fragmentation of *minimum-bias* partons with no high-p_t trigger imposed are called here minijets.

Because the momentum of parent partons is carried by the daughter minijet hadrons [62], particles in a minijet have a strong angular correlation with the jet thrust-axis, which is the momentum direction of the scattered parton, as well as a correlation between the parent parton momentum and the total momentum of particles in the minijet. Thus, it can be expected that minijets display characteristic angular and p_t correlation structure in two-particle correlation spaces.

Although in this work the correlation of particles with $p_t < 2$ GeV/c is studied, a significant contribution from hard-process particles (minijets), is observed with axial and transverse momentum correlation measurements. Observations of the suppression of single-particle hadron-spectra at high-p_t ($p_t > 2$ GeV/c) [63, 64] and the disappearance of back-to-back jets [43] are indicative of correlation modifications in central heavy ion collisions. Such modification may be resulted from a dense medium created in heavy ion collisions which may reduce parton transverse momentum [65–67] and modify minijet transverse momentum distributions, or may affect parton fragmentation processes. Minijets may possibly be distinguished by their characteristic two-particle correlation structure. Current study of correlation structure and centrality dependence reveal particle production mechanisms and detailed information about the dense medium created in heavy ion collisions.

Chapter 5

Analysis Details

The event samples of Au-Au collisions at $\sqrt{s_{NN}} = 130$ GeV obtained with two sets of trigger settings may include some artificial effects due to a limit of hardware and offline softwares. In this chapter, selections of events, track-wise and pair-wise cuts applied to data to reduce the effects not relevant to current study are described. These selections are applied before two-particle number-density distributions are constructed.

5.1 Event Selections

Stored TPC ADC (Analog to Digital Convertor) values, several millions of numbers per event are transformed into physically meaningful quantities by the STAR offline-reconstruction software. Three of the most basic tasks of the event-reconstruction software are the *hit finding* by which three-dimensional coordinates of hit positions where charged particles crossed in the TPC are obtained, the *tracking of the reconstructed hit positions* with the best knowledge of calibration parameters and the *collision vertex finding.* A reconstructed track provides vector-momentum and charge-sign of the particle from shape of the track vend in the uniform magnetic field and loosing some of its kinetic energy. Collision-vertex position is determined by extrapolating tracks toward the beam line and a set of tracks associated with the collision-vertex characterizes the event. The vertex positions were varied event by event over TPC length $z = \pm 2$ m along the beam-axis during the first-year physics run. When collision points are largely offset from the center of TPC, because of the finite size of the TPC, not enough hits are reconstructed to perform precise tracking in both positive and negative pseudorapidity regions. For this reason events with vertex positions in the range -75 cm $< V_z <$ $+75$ cm along the beam axis and -3 cm $< V_{x,y} <$ $+3$ cm in x-y (transverse) direction are selected in this analysis (Fig. 5.1 (a)).

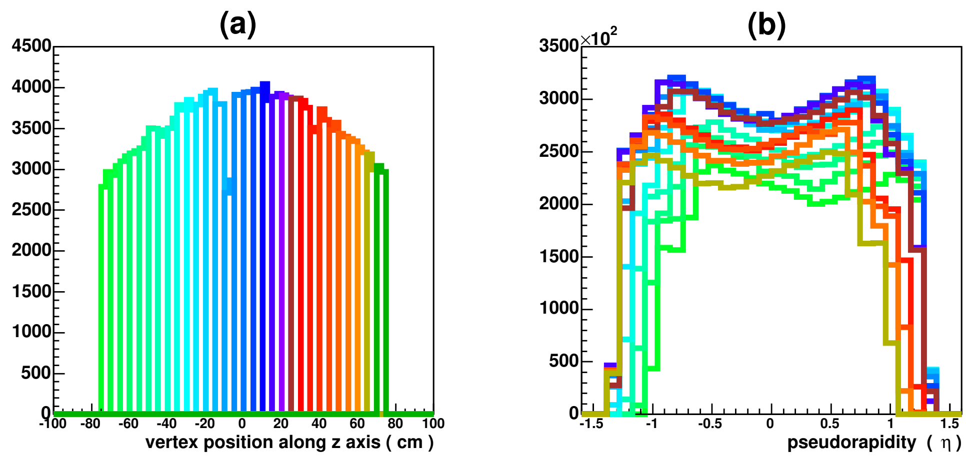

Figure 5.1: Collision vertex position distribution and corresponding pseudorapidity distributions. Right panel: (a) event distribution of vertex positions along the beam-axis, left panel: (b) pseudorapidity distributions for events with different vertex z-coordinate, the colors correspond to the vertex positions shown in (a).

5.2 Track Selections

Tracks in the transverse momentum range $0.15 < p_t < 2.0$ GeV/c are selected in this analysis. The upper p_t limit matches to the selection used in the first single-particle spectra analysis by the STAR collaboration [68]. This selection allows us to apply the study on the single-particle background contribution and tracking efficiency estimation for the spectra analysis directly to this study. In the spectra analysis which requires improved momentum resolution, the upper p_t limit is set by the resolution condition, because the resolution is determined from track helix curvatures and the curvatures are less sensitive for high p_t particles. The lower limit is set to avoid the large contributions from electron backgrounds from photon conversions which exponentially increase with decreasing p_t [69].

The reconstruction efficiency variations associated with vertex-position distribution limit on pseudorapidity range of tracks by $-1.3 < \eta < 1.3$. The right panel in Fig. 5.1 shows the pseudorapidity distributions for events with different vertex z-positions. The event-wise efficiency changes with different vertex positions require the construction of mixed-pair reference from events with close vertex positions (Sec. 5.5). The contribution from short-lived particles which decay within several cm from the reconstructed collision vertexes such as Λ and K_s^0 are reduced by choosing tracks of which distance to closest approach (DCA) to the collision vertex is less than 3 cm. Tracks of bad tracking qualities for example a track which has a large number of fit iterations to obtain a converged value or has many outlier removal and eliminated points, are rejected. In addition to the requirement which requests at least 10 hit points for the tracking of each particle, the number of hit points is requested to be larger than the half of the total possible number of reconstruction points for the track. This conditions are applied for tracking accuracy and to avoid the situation that a true particle trajectory is segmented into two or more pieces and each segment is reconstructed as a track.

5.3 Pair Selections

Pair-wise mis-reconstruction effect results in different two-particle reconstruction efficiency distributions for sibling pairs in which both particles are from the same event and for mixed pairs in which particles are from different events. Thus, when sibling-to-mixed pair ratio is taken, the effect is not canceled. This effect resembles as (anti-)correlations in two-particle space and pair-wise correction is required to eliminate them. The basic correction procedure for the pair-tracking effects is to apply the same pair-wise cuts on both sibling-pair and mixed-pair distributions, by which sibling- and mixed-pair efficiency distributions are corrected to have the same distributions. For this reason, study of sufficient condition which excludes the region of momentum space in which pair efficiencies differs for sibling- and mixed-pairs but still retains sufficient number of pairs is an important issue in this analysis.

Geometrical conditions which lead to incorrect reconstructions can be categorized into two by appearance of effects in two-particle space. One is *track-splitting* which is caused by one particle reconstructed as two or more tracks, appears as positive correlation on two-particle space, and the other is *pair-merging* which is caused by two or more tracks reconstructed as one track, resembles negative correlation.

Track-splittings are removed by the track-wise requirement that tracks should have the number of hit points used for tracking larger than the half of the total number of possible reconstruction points for the track (hit-ratio cut). By this hit-ratio cut, when a single particle trajectory is reconstructed as more than one track and none of the pieces have greater than 50% of the estimated maximum number of possible hits, then all segments are lost and then this loss is another form of single-particle tracking inefficiency and cancels when sibling- to mixed-pair ratio is taken. However, there is two-track inefficiency aspects, if the loss is not randomly occurred but induced with some pair-wise conditions. The effect induced by the track-splitting are studied based on track separations in TPC active volume. Pair separations are calculated separately at the inner radius of the TPC ($r = 50$ cm) $d^{in}_{t,z}$, at between the inner and outer pad-sectors ($r = 127$ cm) $d^{mid}_{t,z}$ and at the TPC outer radius ($r = 200$ cm) $d^{out}_{t,z}$, where the indices t and z indicate the projected distances onto transverse and z directions respectively. The separations are calculated as linear distances between tracks at different radii and is illustrated in the Fig. 5.2.

In Fig. 5.4, pair-ratio distributions of separation at mid-TPC radius for only positive azimuth angle difference pairs are shown. Pairs with positive (blue points) and negative (red points) transverse-momentum differences for each charge-pair combinations are independently plotted and the differ-

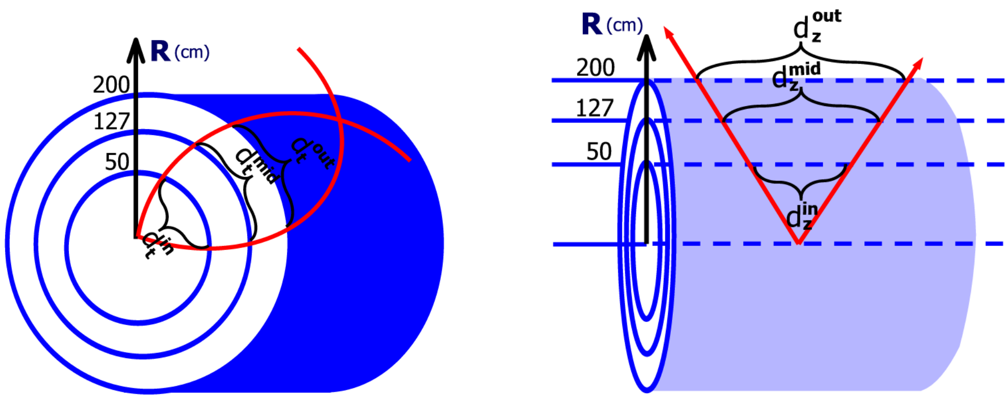

(i) Transverse separations (ii) Longitudinal separations

Figure 5.2: Sketch of the TPC entrance, middle and exit separations for merging-pair and splitting-track corrections. The separations are calculated liner distances at different radii.

ence in the distributions are clearly observed. This observation indicates that track-splitting are induced by *pair-crossing* near the mid-TPC radius as illustrated Fig. 5.3, because only pairs which can have pair-crossing geometries as illustrated in left panels (a) and (b) are suffered from the negative peak and pairs which are free from pair-crossing geometries have positive peak which is consistent with the Bose-Einstein correlation expectation for LS pairs. After the hit-ratio cut, the negative correlation induced by pair-crossing are distinguished from that induced by pair-merging by contrasting their azimuth angle difference and p_t difference dependencies.

Fig. 5.4 shows that the negative correlation induced by pair-crossing is well confined within small mid-TPC pair separations, and the upper panels (i)

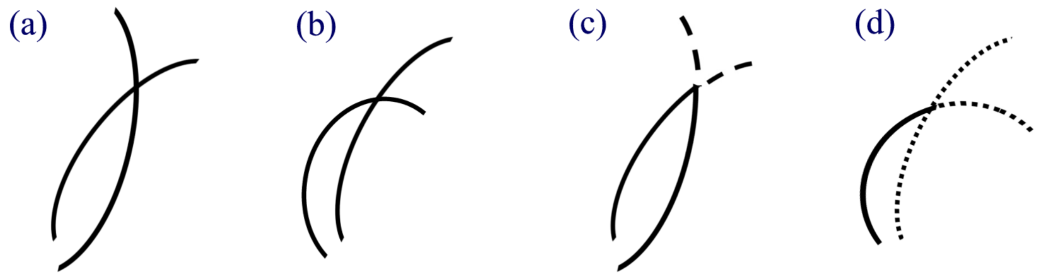

Figure 5.3: Sketch of possible pair-crossing for (a) US and (b) LS. Track-splitting are induced by pair-crossing. In (c), splitting track is correctly removed and in (d) segments are incorrectly removed and resembles as negative correlations.

Thus, sibling- and mixed-pairs with $d_t^{mid} < 30$ cm, $d_{\tilde{z}}^{mid} < 10$ cm for the pair combinations which can have pair-crossing geometry are removed from this analysis. Possibility for a pair to have pair-crossing geometry depends on its charge-pair combination, sign of azimuth angle difference and transverse momentum difference, *i.e.*, by explicitly writing the mid-TPC separation cut is applied for $(+.+)$ pairs which have $\phi_1 - \phi_2 > 0$ and $p_{t1} - p_{t2} < 0$, $(-.-)$ pairs with $\phi_1 - \phi_2 \lesseqgtr 0$ and $p_{t1} - p_{t2} \lesseqgtr 0$, $(-.+)$ pairs with $\phi_1 - \phi_2 < 0$ and $(+.-)$ with $\phi_1 - \phi_2 < 0$.

in Fig. 5.5 show that this negative correlation distributes over relatively large momentum differences and indicate that the mid-TPC radius separation cut need to be applied for the pairs of up to large transverse momentum differences.

After the mid-TPC separation cut, the pair-merging effect which appears as negative correlation in two-particle spaces is treated. The negative correlation induced by pair-merging *i.e.* two or more tracks are reconstructed as one track, is expected to have relatively small pair separations over TPC volume. This expectation indicates that the average pair separations at 9 radii within TPC radius for those pairs are sensitive to the pair-merging effect. The pair-ratio distributions of average pair separations are shown in the lower panels (ii) of Fig. 5.5. The red points and the lower right panel indicate

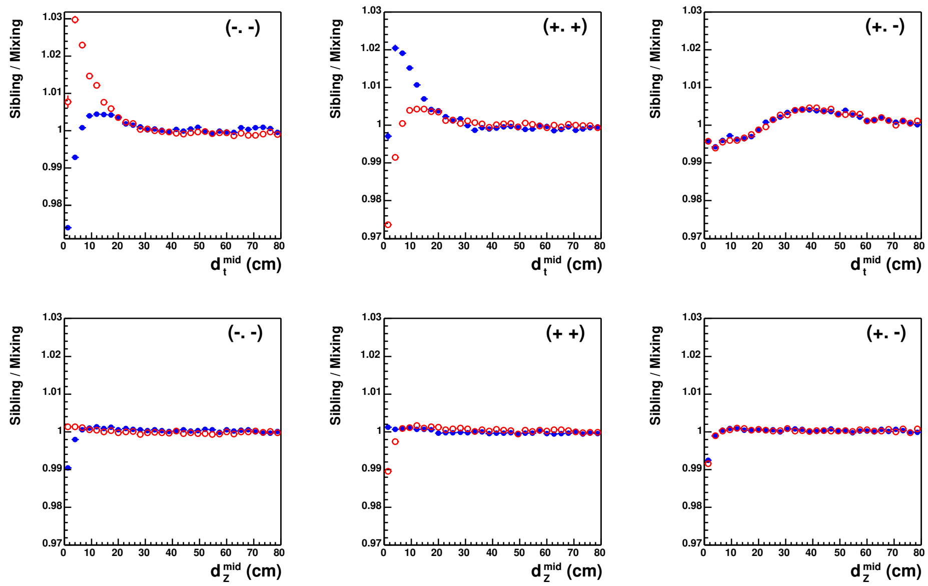

Figure 5.4: Pair distributions as functions of pair separations at the mid-TPC radius for positive azimuth angle difference pairs are shown. Pair separations for positive (blue, closed circle) and negative (red, open circle) p_t difference pairs are compared for each negative-negative (left-hand panel), positive-positive (middle panel) and positive-negative (right-hand panel) charge combinations.

the average pair separation in transverse and longitudinal directions *after* the mid-TPC separation cut. The blue points and the upper right panel indicate the average pair separation in transverse and longitudinal directions *before* the mid-TPC separation cut. It is observed that the pair-merging effect (and may be some contribution from track-splitting which could not be removed by mid-TPC separation cut) is concentrated on small average separations. Thus, pairs with the average separation smaller than 10 cm in both longitudinal and transverse direction are excluded from this analysis.

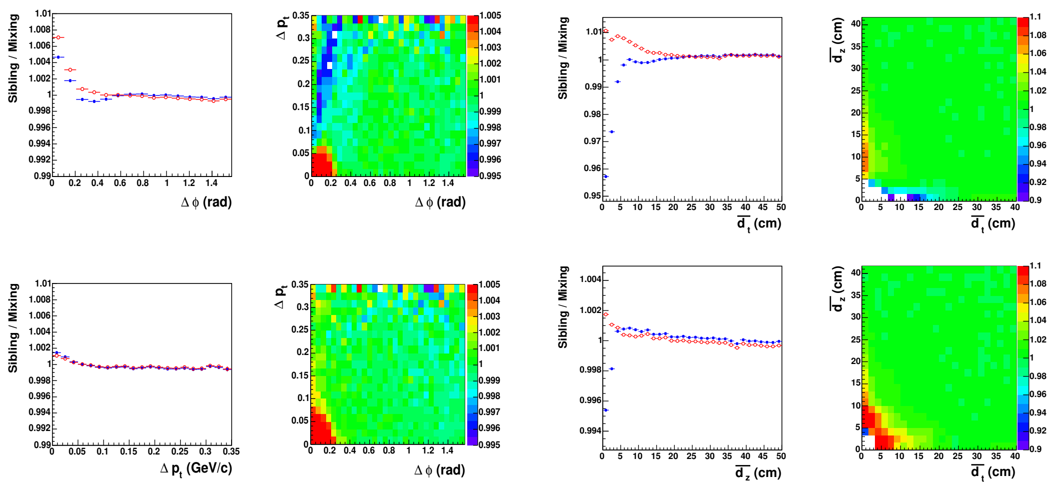

(i) Pair ratios of azimuth (upper left) and p_t differences (lower left). Joint ratios are shown in the right-hand for before the mid-TPC cut (upper) and for after the mid-TPC cut (lower).

(ii) Pair ratios of average separations in transverse (upper left) and longitudinal (lower left) directions. Joint ratios are shown in the right-hand for before the mid-TPC cut (upper) and for after the mid-TPC cut (lower).

Figure 5.5: Two-particle ratios on (i) momentum differences and (ii) average separations before (blue points in the left plots and upper right plot) and after (red points in the left plots and lower right plot) the mid-TPC separation cut.

The final two-particle ratio distributions of average separations before pair-merging cut (blue, upper right panel) and after pair-merging cut in addition to pair-crossing cut (red, lower right panel) are shown in Fig. 5.6.

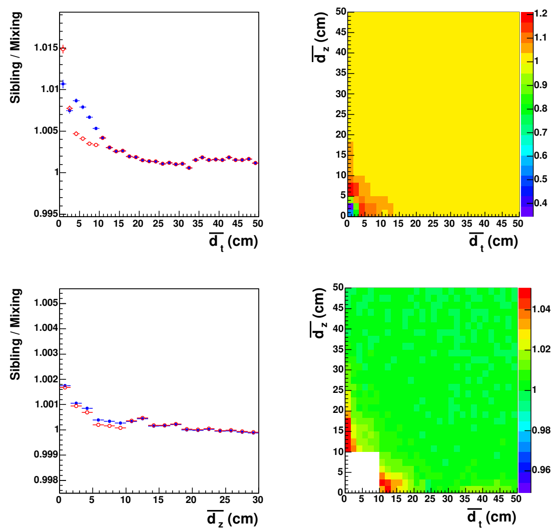

Figure 5.6: Two-particle ratios of average pair separations in transverse (upper left) and longitudinal (lower left) directions before pair-merging cuts (blue points) and after pair-merging cuts (red points) are shown. Joint ratios are shown in the right-hand panels before pair-merging cuts (upper right panel) and after pair-merging cuts (lower right panel) are also presented.

5.4 Centrality Definition

In A-A collisions, there is a variation in impact parameters $\vec{b}$ defined by the relative transverse positions of the colliding nuclei (Fig. 4.4). For the most central $b = 0$ events, the number of nucleons involved in collisions are expected to be the maximum, or the larger b the less number of nucleon participate to collisions and thus collision dynamics and particle production mechanisms in heavy ion collisions with large b become closer to that of elementary collisions. Collision-centrality dependencies of observable quantities is important in heavy ion collision physics for studies of heavy ion specific phenomena. However, direct measurement of impact parameter is not possible and instead we make use of a strong correlation between impact parameters and multiplicities, because the more number of nucleons contribute in the more central collision and the more energy is deposited into the interaction region, which results in the more number of particle produced.

In this analysis the event samples are divided into 4 centrality classes according to the number of charged tracks N_{track} within the pseudorapidity range $1.3 < \eta < 1.3$. From the higher centrality events, 'most-central', 'mid-central', 'mid-peripheral' and 'peripheral bins correspond to the event multiplicity ranges $1350 \leq N_{track} < 1650$, $950 \leq N_{track} < 1350$ $350 \leq N_{track} < 950$ and $50 \leq N_{track} < 350$ respectively. The number of good events in each centrality bin are 58k, 158k, 55k and 68k respectively from the higher centrality bins. The multiplicity distributions of lower two bins which are taken with minimum-bias trigger and upper two bins which are taken with central trigger are shown in Fig. 5.7.

Normalization of correlation amplitudes from different centrality classes are obtained by multiplying the obtained two-particle density ratios by the mean number of tracks in each centrality class (Sec. 3.4). In actual exper-

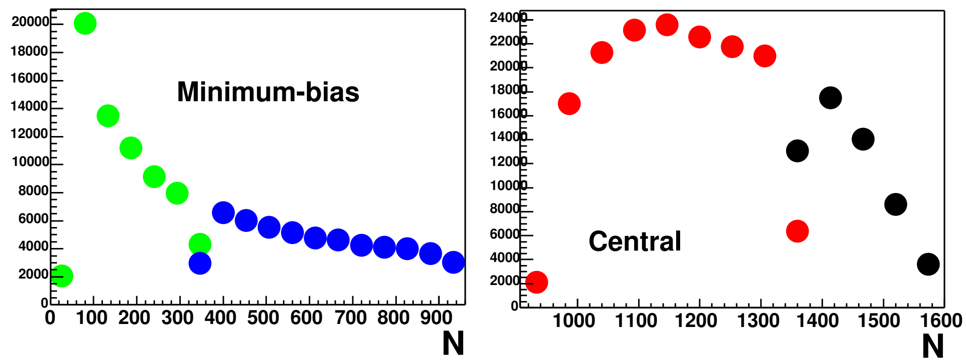

Figure 5.7: Multiplicity distributions for four centrality classes. Left panel: minimum-bias sample, green region is peripheral and blue region is mid-peripheral bin, right panel: central 15% sample, red region is mid-central and black region is most-central bin.

iments, incomplete single-particle efficiencies result a reduction of the normalized correlation amplitude and it is corrected by normalizing with the extrapolation factor $\mathcal{S}$ which corrects the single-particle inefficiencies. Extrapolation factor $\mathcal{S}$ is obtained by Monte Carlo simulations assuming random tracking loss or random reduction of total correlations for each centrality bin and corresponds to the mean multiplicity correction factor which is obtained by extrapolated to $p_t = 0$ based on spectra analysis. $\mathcal{S}$ are obtained to be 1.19, 1.22, 1.25 and 1.27 with associated 8% systematic uncertainty from peripheral to most-central classes respectively.

5.5 Mixed Pair Construction

Mixed-pairs reference distributions are constructed to have the same single-particle distributions as the sibling-pair distributions but which do not contain two-particle correlations. Mixed-pair reference from different event properties and thus different single-particle distributions may result an artificial fluctuation in the reference distributions [70]. Because single-particle efficiency distributions of pseudorapidity highly depend on collision-vertex positions along the beam axis and event properties change with collision centrality thus event multiplicity, mixed-pairs are constructed from the events of which vertex position difference along the beam axis within 7.5 and 5.0 cm and multiplicity differences 100 and 50 for the minimum-bias triggered sample and central triggered sample respectively.

In Fig. 5.8, the multiplicity difference (upper panels) and collision vertex position deference (lower-panels) distributions of the events mixed are shown as black closed triangles for peripheral (left-hand panels) and most-central (right-hand panels) classes. The results using different (tighten) selections for events to be mixed shown as red open triangles in Fig. 5.8. Those values are used to check the stability of mixed-event selection and the verification of the selection are presented in Sec. 6.4.6 and 7.3.6 for the two-particle transverse and axial-momentum spaces respectively.

5.6 Flattening Method for Transverse-Momentum Space

For analysis of large-scale correlation structures, it is essential to have statistical error approximately constant to evaluate the correlation structures fairly over the momentum scales under study. In particular, a method to avoid the large statistical error differences is required in the transverse momentum

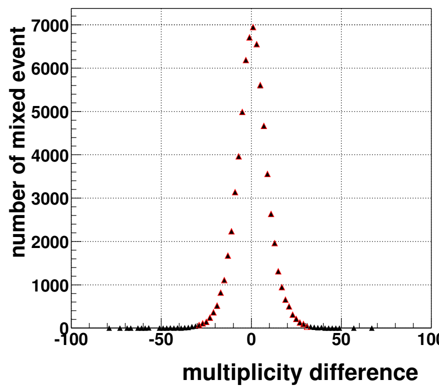

(i) Peripheral centrality class

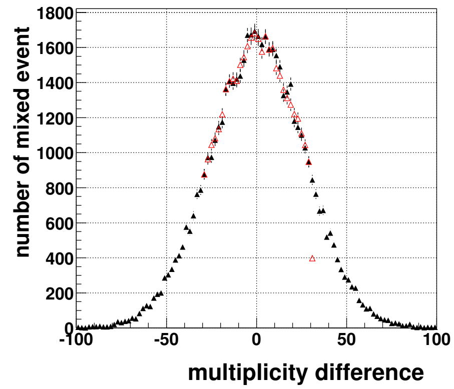

(ii) Most-central class

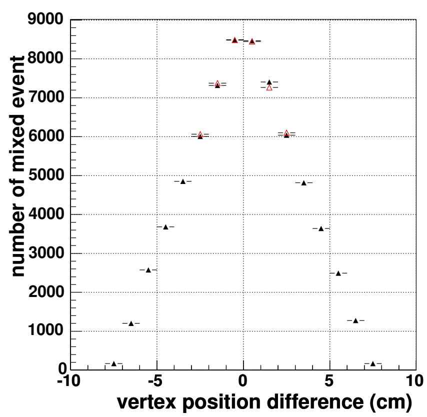

(iii) Peripheral centrality class

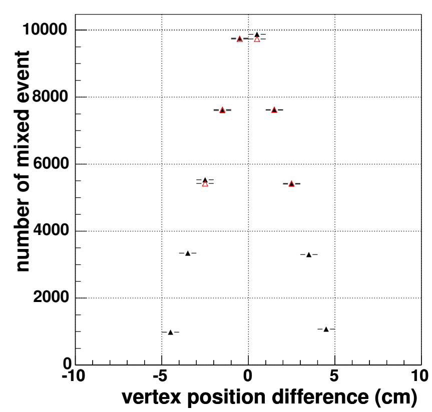

(iv) Most-central class

Figure 5.8: Multiplicity difference (a, b) and collision vertex position difference (c, d) distributions for the events mixed (from which mixed-pairs are constructed) are shown. Black triangles indicate the distribution used in this analysis.

space because the single-particle p_t distribution is approximately expressed by Maxwell-Boltzmann distribution, *i.e.* the distribution decreases exponentially with p_t. For this reason a non-linear binning in p_t is used to achieve approximate uniform statistics. This is implemented by p_t-to-$x(p_t)$ transformation defined by Eq. 5.6, *i.e.* analysis is performed based on an uniform binning on $x(p_t)$. This transformation is defined as,

$$x(p_t) \equiv 1 - \exp(-\frac{m_t - m_\pi}{Y}), \tag{5.1}$$

or transverse mass $m_t \equiv \sqrt{{p_t}^2 + {m_\pi}^2}$ is expressed in terms of x as,

$$m_t - m_\pi = -Y \ln(1 - x), \tag{5.2}$$

where $Y = 0.4$ GeV/c is a transformation parameter chosen to provide an approximate constant single-particle distribution. This transformation corresponds to changing the bin-sizes in p_t space to include approximately the same number of tracks in each bin. The correspond bin-sizes in transverse-momentum space and in transformed space are shown in Fig. 5.9. Note that the transformation function used for similar analysis at lower energy were different and an optimized function at the energy was used [42, 71]. Although selections of the transformation function is independent from interpretations of results, further studies may provide a general form of the function which can be used for the study at different collision energy and event properties.

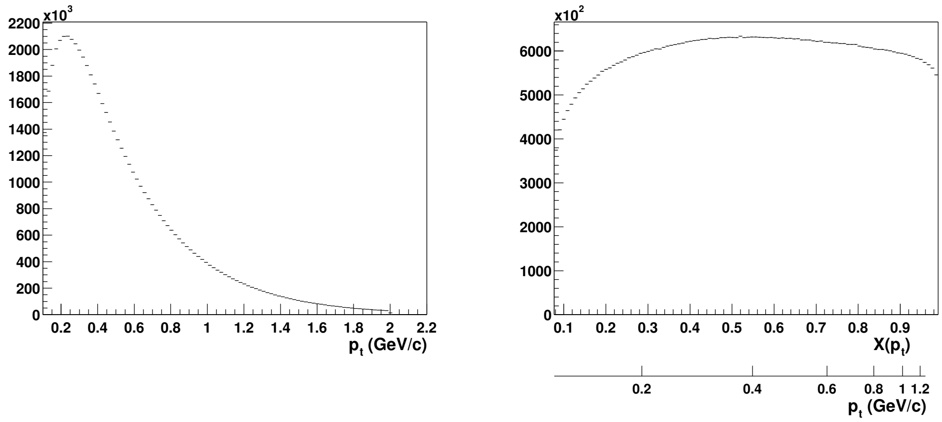

(i) Single particle p_t distribution

(ii) Single particle $x(p_t)$ distribution with corresponding p_t axis

Figure 5.9: Flattening function in transverse momentum space

5.7 Bose-Einstein and Coulomb Correlation Cut

Strong peaks of small-momentum-scale correlations arising from the Bose-Einstein statistical interference for LS pairs and from the Coulomb interactions for both LS and US pairs are observed. For studies of large-scale two-particle correlation structures, the contribution from such known short-momentum-scale correlations should be estimated or eliminated. These short-momentum-scale correlations have been extensively studied in the applications of the HBT (Hanbury Brown and Twiss) interferometry analysis [72, 73]. Pairs affected by such correlations are well confirmed in small-momentum-scale and the effect is eliminated by excluding small-momentum-scale pairs for sibling and mixed distributions. The conditions to remove such pairs are studied using Monte Carlo simulations [74] shown in Fig. 6.21 and 7.13. The pairs with pseudorapidity difference $|\eta_\Delta| < 0.3$, azimuth angle difference $|\phi_\Delta| < \pi/6 = 0.5236$ rad, transverse momentum difference $|p_{t\Delta}| < 0.15$ GeV/c and transverse momentum of at least one of the pair particles $p_{t1}, p_{t2} < 0.8$ GeV/c for CI correlations in which most of the Coulomb correlation are canceled. For studies of CD correlation, the conditions are extended to pseudorapidity difference $|\eta_\Delta| < 1.0$, azimuth angle difference $|\phi_\Delta| < \pi/3 = 1.0472$ rad, transverse momentum difference $|p_{t\Delta}| < 0.2$ GeV/c and transverse momentum of at least one of the pair particles $p_{t1}, p_{t2} < 0.8$ GeV/c to take into account of the Coulomb correlations.

The systematic uncertainties associated with data selections described in this chapter are estimated for each momentum space following results in Sec. 6.4 for transverse-momentum two-particle space and in Sec. 7.3 for axial-momentum two-particle space.

Chapter 6

Two-particle Transverse-Momentum Correlations

Results from two-particle transverse momentum correlation analysis of Au-Au collisions at 130 GeV per nucleon pair are presented in this chapter. Results are divided into charge-independent (CI) and charge-dependent (CD) parts of correlation structures. Observations of substantial nonstatistical fluctuations in event-wise mean transverse momentum $< p_t >$ of charged particles (CI) $[41, 75, 76]$ and charge dependent (CD) part of fluctuations [41] from Au-Au collisions at RHIC energies ($\sqrt{s_{NN}} = 130$, 200 GeV) suggest corresponding correlation structures in transverse-momentum two-particle space.

Events, tracks and particle pairs are selected according to Sec. 5.1 - 5.3 of which justification and associated systematic uncertainties follow the results. In this study, total of 340k events (217k central and 123k minimum-bias triggered event samples) are analyzed and divided into four centrality bins defined in Sec. 5.4 according to event multiplicities. The small-momentum-scale (the Bose-Einstein and Coulomb) correlations are eliminated according to Sec. 5.7 unless noted.

6.1 Charge Independent (CI) Correlations

In Fig. 6.1, charge-independent (CI) transverse two-particle density ratios $R(x(p_{t1}), x(p_{t2})) - 1$ for four centrality classes are shown as functions of x (transformed p_t, see Sec. 5.6). Dominant correlation feature of 'saddle-shaped' structure is observed in the CI transverse two-particle density ratios common to all four centrality bins.

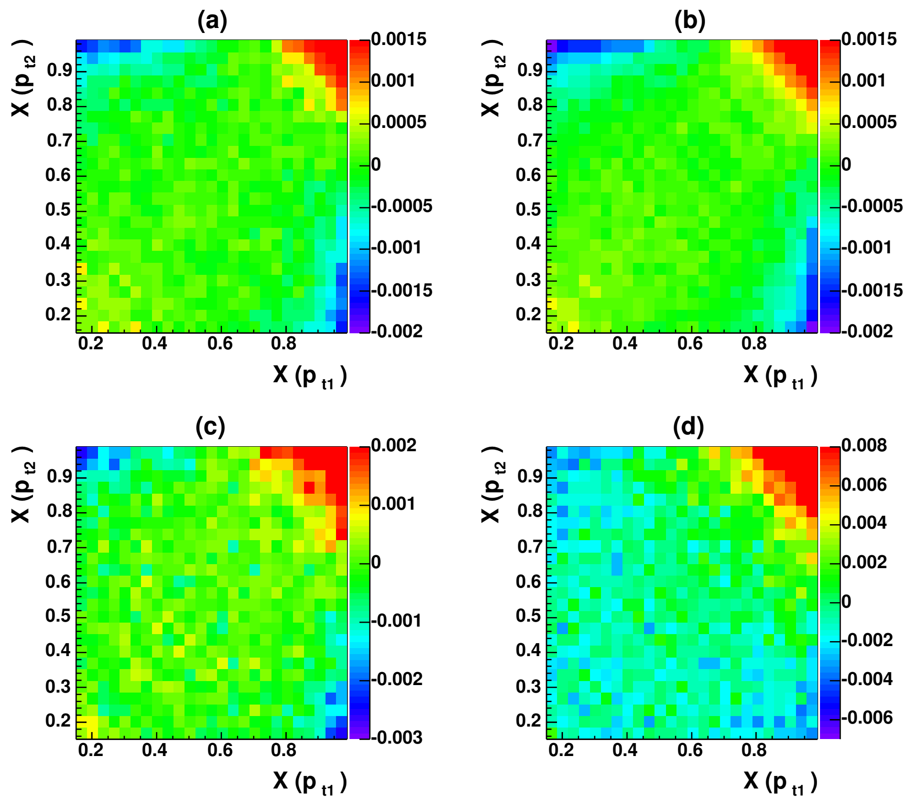

Figure 6.1: Centrality dependence of CI transverse two-particle density ratio in Au-Au collisions at $\sqrt{s_{NN}} = 130$ GeV for (a) most-central (b) mid-central (c) mid-peripheral and (d) peripheral centrality bins.

a) ***Two-dimensional Fit***

The large-momentum-scale saddle shape structure composed of a concave upward along the sum axis and a concave downward along the difference axis is observed. With increasing centralities the negative saddle curvature along the difference direction increases in magnitude, the positive curvature along the sum direction decreases, and the magnitude of the peak at large $x(p_t)$ also decreases. A similar analysis of Pb-Pb collisions by NA49 experiment at the CERN SPS observed no significant CI correlations in the different rapidity acceptance of $1.1 \leq y_{cm} \leq 2.6$ [42].

The large-momentum-scale feature can be compared with the two-particle density ratio from the Monte Carlo simulation (Fig. 6.2) in which a gaussian event-by-event mean temperature fluctuation of $\sigma_T/\overline{T} = 1.5\%$ for all particles (left-hand panel) and a half of pairs (for example only LS pairs, right-hand panel) are included. The plots show that the correlation structure resulted from the temperature fluctuation appears on two-particle transverse momentum space is consistent with saddle-shaped structure. However the details of the structure obtained from simulation is qualitatively different, and it is expected that the details of correlation shape (curvature along sum and difference variables) to be dependent on the nature of event-by-event and event-internal fluctuations.

This observation is consistent with the use of temperature fluctuation based model introduced in Sec. 4.1 to parameterize obtained saddle-shaped feature of the CI two-particle transverse momentum correlation. The model

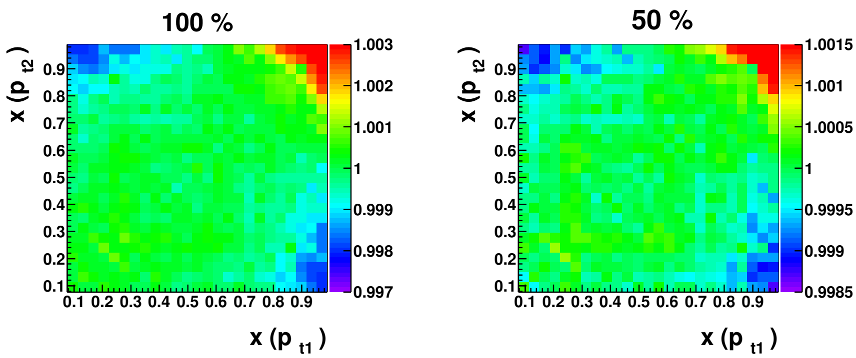

Figure 6.2: Monte Carlo simulation of transverse-momentum two-particle density ratios with event-by-event temperature fluctuation among all particles (left-hand panel) and a half of pairs (right-hand panel).

function is written as the ratio of Eq. 4.18 and Eq. 4.17 as,

$$\begin{aligned} f_{model} &= R_{model}(x_1, x_2; n, \beta_0) - 1 \\ &= \frac{(1+\frac{\beta_0 m_{t,\Sigma}}{2n_\Sigma})^{-2n_\Sigma}}{(1+\frac{\beta_0 m_{t,\Sigma}}{2n})^{-2n}} \frac{(1-(\frac{\beta_0 m_{t,\Delta}}{2n_\Delta+\beta_0 m_{t,\Sigma}})^2)^{-n_\Delta}}{(1-(\frac{\beta_0 m_{t,\Delta}}{2n+\beta_0 m_{t,\Sigma}})^2)^{-n}} - 1 + \mathcal{C}, \end{aligned} \tag{6.1}$$

with 3 fit parameters n_Σ, n_Δ, $\mathcal{C}$ and 2 fixed parameters n and $\beta_0 = \frac{1}{T_0}$, where pair transverse mass sum $m_{t,\Sigma}$ and difference $m_{t,\Delta}$ are written in terms of x as, $m_{t,\Sigma} \equiv m_{t1} + m_{t2} = -0.4\ln(1-x_1)(1-x_2) + 2m_0$ and $m_{t,\Delta} \equiv m_{t1} - m_{t2} = -0.4\ln\frac{(1-x_1)}{(1-x_2)}$. Pion masses are assigned for all particles, m_0 =140 GeV/c^2.

The denominator in Eq. 6.1 which represents a model function for the mixed-pair distributions is written as a product of two single-particle distributions each of which includes fixed parameters n and β_0. The inverse temperature parameter $\beta_0 = \frac{1}{T_0}$ is obtained by fitting single-particle distribution for the range $0.2 < x(p_t) < 0.9$ with Lévy (Eq. 6.2) and Maxwell-Boltzmann

(Eq. 6.3) distribution functions,

$$f_{Lévy}(m_t; n) = \frac{A}{(1 + \frac{\beta_0 m_t}{n})^n}, \tag{6.2}$$

$$f_{MB}(m_t) = \lim_{n \to \infty} f_{Lévy}(m_t; n) = A' e^{-\beta_0 m_t}, \tag{6.3}$$

as shown in Fig. 6.3. The MB fit (blue lines) gives average value of $T_0 \simeq$ 0.22 GeV and Lévy fit (red lines) gives $T_0 \simeq 0.17$ GeV width the obtained fluctuation parameter $1/n \simeq 0.13$ ($n \simeq 7.5$). The difference between the MB

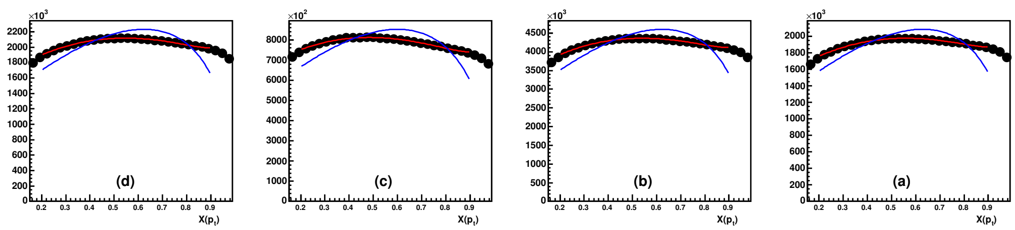

Figure 6.3: Single-particle p_t distributions for (a) most-central, (b) mid-central, (c) mid-peripheral and (d) peripheral bins are fitted with the Maxwell-Boltzmann (MB) and Lévy distribution function for the range $0.2 < x < 0.9$. Blue and red lines denote fit with MB and Lévy distribution respectively. MB distribution include inverse temperature as a fitting parameter and Lévy includes additional parameter $1/n$ which may be related to the fluctuation of inverse temperature parameter. No single-particle distribution collection for tracking efficiencies is applied in the plots.

and Lévy distributions is generally considered to be mainly due to a strong collective radial expansion and often parameterized as $\frac{1}{m_t}\frac{dN}{dm_t} \propto e^{-\frac{m_t}{T_0 + m < v_t >^2}}$ where $< v_t >$ is an average radial velocity parameter [77]. A large part of difference between data described by Eq. 6.2 and thermal model Eq. 6.3 results from radial expansion, but a smaller part may result from temperature fluctuations represented by $1/n_{thermal} = \sigma_\beta^2/\beta_0^2$. Those parameters are fixed for the purpose of Eq. 6.1 as $\beta_0 = 5$ GeV^{-1} ($T_0 = 0.2$ GeV) and $1/n_{thermal}$ in the range 0.02 - 0.04.

Obtained best-fit parameters and χ^2/DoF from the model function (Eq. 6.1) with three $1/n$ values, excluding large-sum region ($x_\Sigma \equiv x_1 + x_2 > 1.6$) from the fit are presented in Table 6.1, with the normalization factor $(\mathcal{S}\overline{N} - 1)$ (Sec. 3.4 and 5.4). Extracted parameter values assure that centrality behaviors of obtained quantities which measure and characterize curvatures of the structure, expressed as $\Delta(1/n)_\Sigma \equiv (\frac{1}{n_\Sigma} - \frac{1}{n})$, $\Delta(1/n)_\Delta \equiv (\frac{1}{n_\Delta} - \frac{1}{n})$ and $\Delta(1/n)_{total} \equiv (\frac{1}{n_\Sigma} - \frac{1}{n_\Delta})$, are not sensitive to the choice of n, although some constant shifts ($< 12\%$) of those values dependent on n are observed for the range. For further study of the fitting residual, the middle value $1/n = 0.03$, which is in agreement with simulation study [78], is used.

In Fig. 6.4, obtained parameters with $\frac{1}{n} = 0.03$ are presented as functions of centrality ($\frac{\overline{N}}{N_0}$) where N_0 is the endpoint multiplicity defined as the half-max point at the end of the minimum-bias distribution [41] of all events. In Fig. 6.5, the obtained function R_{model} (left-hand panels) and fitting residuals (right-hand panels) are shown. The residual distributions display small structure over the fitting region and a deviation at large x_Σ which depends only on sum variable. The residual structure demonstrates the adequacy of two-dimensional Lévy fitting function inspired by temperature fluctuation hypothesis in addition to a significant deviation at large x_Σ region. Fig. 6.4 illustrates that the curvature near origin along $m_{t\Delta}$-axis measured by $(\mathcal{S}\overline{N} -$

$1)|\Delta(1/n)_\Delta|$ increases, and along $m_{t\Sigma}$-axis measured by $(\mathcal{S}\overline{N} - 1)\Delta(1/n)_\Sigma$ decreases smoothly with collision centrality. The smooth transitions may exclude the possibility of that the large-momentum-scale structure are due to critical correlations, although the more detailed centrality study with more event statistics is required for the confirmation.

According to the temperature fluctuation model (Sec. 4.1), comparing the relative covariance directly to a temperature variance by a correlation coefficient $\kappa \equiv (1/n_\Sigma - 1/n_\Delta)/(1/n_\Sigma - 1/n_\Delta) \simeq \Delta(1/n)_{tot}/(2/n_{thermal})$, where n_Σ n_Δ $n_{thermal}$, could determine whether temperature fluctuations are local ($\kappa \sim 0$, fluctuation within each event) or global ($\kappa \sim 1$, event-by-event fluctuation). However because the reference $1/n$ values obtained from single-particle p_t distribution include contributions from thermal fluctuations, radial expansion and hard scattering, $1/n_{thermal}$ is not easily accessible.

The fixed-scale (full-acceptance) correlation measurement of saddle curvatures could set a lower limit on global temperature fluctuation of $\sigma_T/T_0 \geq \sqrt{\Delta(1/n)_{tot}/2} \sim 1\%$ for central events. Upper limit $\sigma_T/T_0 \leq \sqrt{1/n} \sim 30\%$ is derived from the inclusive p_t distribution.

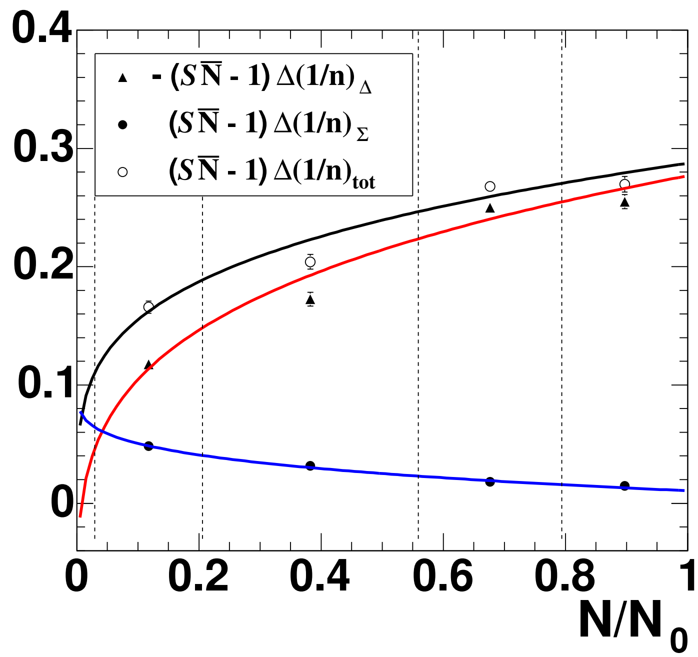

Figure 6.4: Centrality dependence of extracted parameters from two-dimensional Lévy fit to CI transverse two-particle density ratios. Parameters are $-(\mathbb{S}\overline{N}-1)\Delta(1/n)_\Delta$ (closed triangle), $(\mathbb{S}\overline{N}-1)\Delta(1/n)_\Sigma$ (closed circle) and $\Delta(1/n)_{total}$ (open circle). The solid lines indicate the linear functions of mean path length ν estimated by $(N_{part}/2)^{1/3}$, where N_{part} is the number of participant nucleons in an A-A collision according to the Glauber model.

$T_0 = 0.2$ GeV ($\beta_0 = 5$ GeV^{-1})								
	parameters				fitting error(%)			
centrality	(d)	(c)	(b)	(a)	(d)	(c)	(b)	(a)
$\overline{N}$	115.5	424.9	790.2	983.0	————			
$\mathcal{S}$	1.19	1.22	1.25	1.27	8% systematic error			
n=33 ($1/n = 0.03$)								
$(\mathcal{S}\overline{N}-1)\Delta(\frac{1}{n})_\Delta$	-0.117	-0.173	-0.250	-0.255	5.7	4.7	2.0	3.3
$(\mathcal{S}\overline{N}-1)\Delta(\frac{1}{n})_\Sigma$	0.0483	0.0316	0.0180	0.0148	5.8	10.7	11.6	24.0
$(\mathcal{S}\overline{N}-1)\Delta(\frac{1}{n})_{tot}$	0.165	0.204	0.268	0.270	4.3	4.3	2.0	3.4
$(\mathcal{S}\overline{N}-1)\mathcal{C}$	-0.158	-0.0424	0.0776	0.094	5.9	28.0	9.6	13.5
$\chi^2/DoF(286)$	$\frac{347.9}{286}$	$\frac{313.0}{286}$	$\frac{475.0}{286}$	$\frac{402.3}{286}$	————			
n=25 ($1/n = 0.04$)								
$(\mathcal{S}\overline{N}-1)\Delta(\frac{1}{n})_\Delta$	-0.131	-0.194	-0.282	-0.288	5.7	4.7	2.0	3.3
$(\mathcal{S}\overline{N}-1)\Delta(\frac{1}{n})_\Sigma$	0.0496	0.0319	0.0172	0.0137	5.8	10.9	12.5	26.5
$(\mathcal{S}\overline{N}-1)\Delta(\frac{1}{n})_{tot}$	0.181	0.226	0.299	0.301	4.4	4.3	2.0	3.4
$(\mathcal{S}\overline{N}-1)\mathcal{C}$	-0.156	-0.037	0.087	0.103	6.0	31.9	8.6	12.3
$\chi^2/DoF(286)$	$\frac{347.2}{286}$	$\frac{311.4}{286}$	$\frac{456.3}{286}$	$\frac{395.1}{286}$	————			
n=50 ($1/n = 0.02$)								
$(\mathcal{S}\overline{N}-1)\Delta(\frac{1}{n})_\Delta$	-0.104	-0.151	-0.218	-0.222	5.7	4.8	2.0	3.4
$(\mathcal{S}\overline{N}-1)\Delta(\frac{1}{n})_\Sigma$	0.0469	0.0311	0.0185	0.0155	5.7	10.5	10.9	22.0
$(\mathcal{S}\overline{N}-1)\Delta(\frac{1}{n})_{tot}$	0.151	0.182	0.237	0.238	4.3	4.3	2.1	3.5
$(\mathcal{S}\overline{N}-1)\mathcal{C}$	-0.160	-0.0477	0.0681	0.0835	5.8	24.7	10.9	15.1
$\chi^2/DoF(286)$	$\frac{348.8}{286}$	$\frac{315.4}{286}$	$\frac{498.5}{286}$	$\frac{411.4}{286}$	————			

Table 6.1: Parameters and fitting errors for two-dimensional model fits based on two-point temperature hypothesis to CI transverse-momentum two-particle density ratios for (a) most-central (b) mid-central (c) mid-peripheral and (d) peripheral centrality classes.

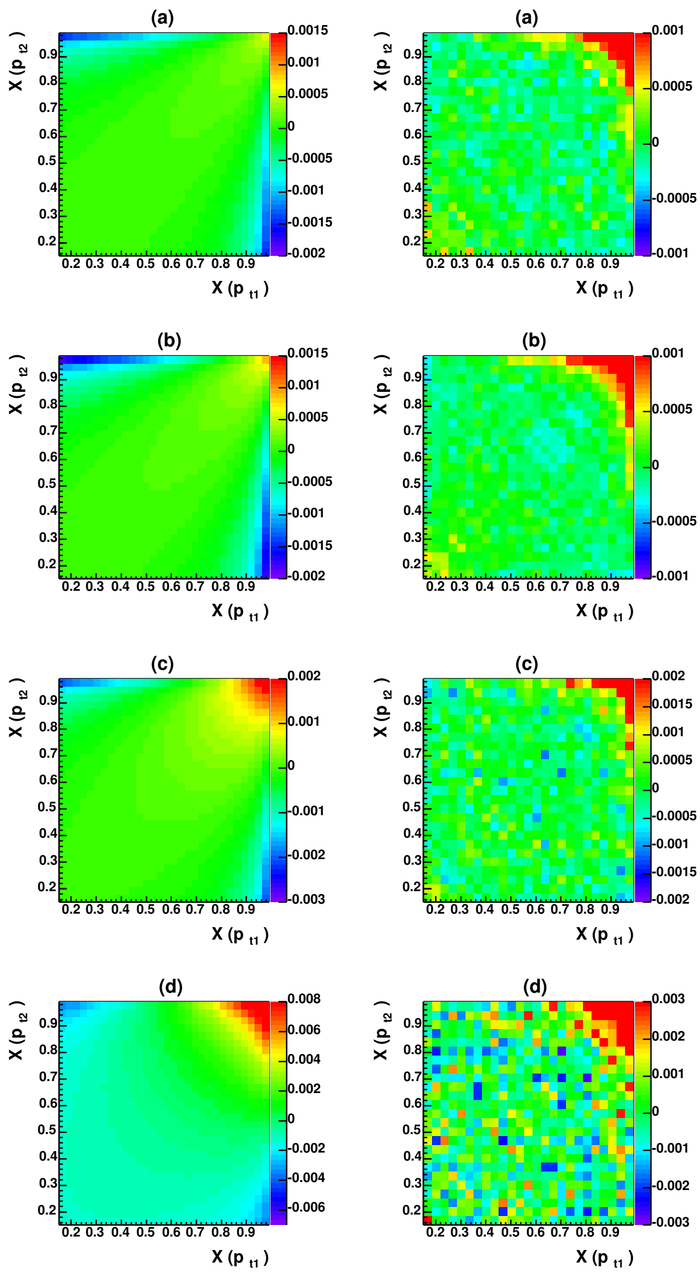

Figure 6.5: Centrality dependence of fit function R_{model} with fixed parameters $n = 33$ and $\beta_0 = 5$ (left-hand panels) and the fit residuals (right-side panels) for (a) most-central (b) mid-central (c) mid-peripheral and (d) peripheral events.

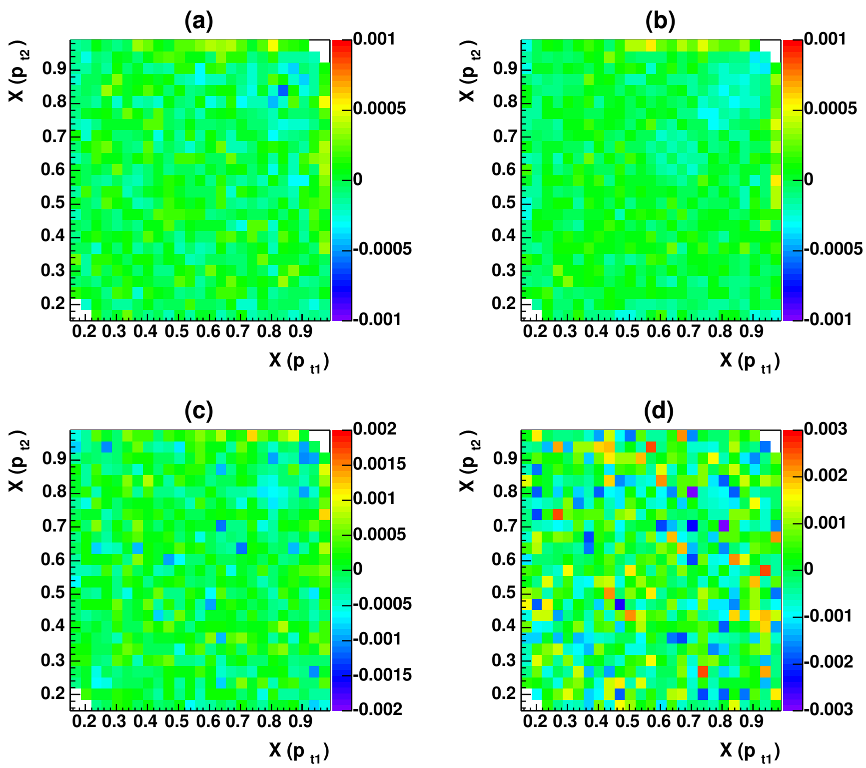

Figure 6.6: Second-residual distributions on CI transverse two-particle density ratios for (a) most-central (b) mid-central (c) mid-peripheral and (d) peripheral centrality classes.

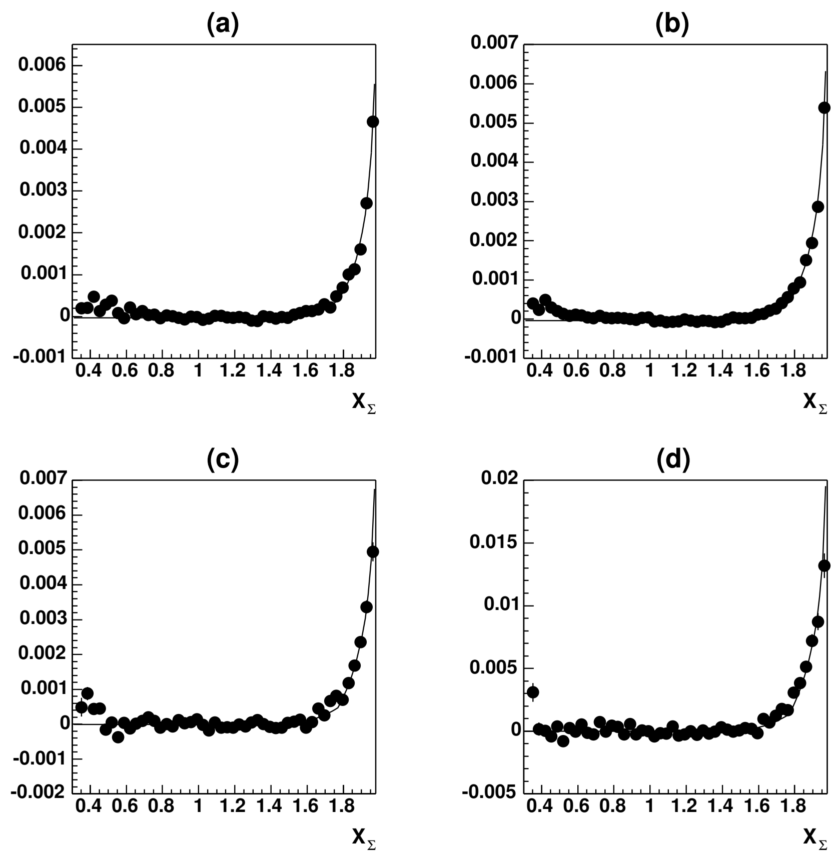

Figure 6.7: Centrality dependence of one-dimensional projections of residual for CI transverse two-particle density ratio with fitting functions for (a) most-central (b) mid-central (c) mid-peripheral and (d) peripheral centrality classes.

b) One-dimensional Residual Fit

The fit residuals obtained by subtracting fitting function R_{model} from data are shown in the right-hand panels of Fig. 6.5. It is observed that these residual distributions exhibit an approximate independence of $x_\Delta \equiv x_1 - x_2$ with its main component at the large x_Σ region of $x_\Sigma \gtrsim 1.4$. This feature suggests a compact one-dimensional representation of residuals by projecting it on the sum (x_Σ) diagonals without loss of information contained in the two-dimensional distributions. The projection is obtained by taking the average of bin contents along diagonals of constant x_Σ.

The appropriateness of this representation are consequently observed as small structure on the 'second-residual' distributions which are obtained by calculating the difference between original residual distribution (right-hand panels in Fig. 6.5) and one-dimensional projection constant in x_Σ. The second-residual are presented in Fig. 6.6 and its small structure confirms that the one-dimensional residual projections contain all remaining correlation contents carried by the two-dimensional residual plots after the saddle-shape fit. The one-dimensional projection of the fit residual distributions with $1/n = 0.3$, $\beta_0 = 5$ GeV^{-1} as function of x_Σ are presented in Fig. 6.7. We speculate the observed correlation structure observed in the one-dimensional projection peaked at large x_Σ is due to hard parton scattering (mini-jet). This conclusion is based on similar correlation structure observed in proton-proton collisions at $\sqrt{s} = 200$ GeV [79].

For the quantitative description of one-dimensional residual projection of x_Σ, we introduce *transverse rapidity* y_t similar to longitudinal rapidity y_t (Eq. 1.1) but with transverse momentum p_t and evaluated in the co-moving axial frame ($p_z = 0$),

$$y_t(p_t) = \ln\left(\frac{p_t + m_t}{m_0}\right). \tag{6.4}$$

In Fig. 6.8, the relation between y_t and p_t (left-hand panel), $x(p_t)$ (right-hand panel) are shown.

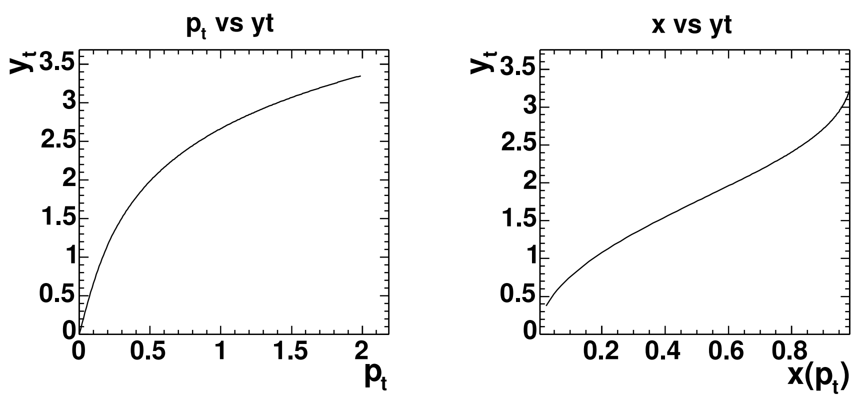

Figure 6.8: Transverse rapidity y_t vs. p_t (left-hand panel) and $x(p_t)$ (right-hand panel)

Taking into account of the fact that the particle distribution from mini-jets observed in p-p collisions are well described by peaked y_t distribution [79] of $f_{model}(y_t) = A\exp[-(\frac{y_t - y_{t0}}{W})^P]$ with $P \sim 2$, which is expected to also contribute to the particle production in Au-Au collisions in the similar way but with some modifications, we parameterize the projected residual with the model distribution mapped to x_Σ space as,

$$f_{model}(x_\Sigma/2) = A\exp\left[-(\frac{y'_{t\Sigma} - y_{t0}}{W})^P\right] \; \frac{dy'_{t\Sigma}}{d(x_\Sigma/2)} + k, \tag{6.5}$$

where $y_{t0} = 2.6$ and $W = 0.6$ are constants determined by p-p correlation analysis [79] and A, k and P denote the amplitude, offset and exponential power fit parameters respectively. The transverse rapidity $y'_{t\Sigma}$ in Eq. 6.5 corresponds to that of pair average $\frac{x_\Sigma}{2}$, $i.e.$, $y'_{t\Sigma} = \ln(\frac{m'_{t\Sigma}}{m_0} + \sqrt{\frac{m'^2_{t\Sigma}}{m_0^2} - 1})$ where $m'_{t\Sigma} = -0.4\ln(1 - \frac{x_\Sigma}{2}) + m_0$ and Jacobian $(\frac{dy'_{t\Sigma}}{dx_\Sigma/2}) = (\frac{dy'_{t\Sigma}}{dm'_{t\Sigma}})(\frac{dm'_{t\Sigma}}{d(x_\Sigma/2)}) = (\frac{1}{\sqrt{m'^2_{t\Sigma} - m_0^2}})(\frac{0.4}{2(1-\frac{x_\Sigma}{2})})$.

The function (Eq. 6.5) fitted on the one-dimensional residual distribution over $0.8 < x_\Sigma < 1.98$ are represented by solid lines in Fig. 6.7. Best-fit parameters are presented in Table 6.2 and their centrality dependencies are shown in Fig. 6.9.

Significant development of the large-x_Σ correlation structure are observed as non-constant increase in the normalized amplitude, integral of the function $I = \int_{0.4}^{0.99} f_{model}(\frac{x_\Sigma}{2}; k = 0) d(\frac{x_\Sigma}{2})$, and decrease in the power parameter P, which is consistent with the observation of large non-statistical event-by-event $< p_t >$ fluctuation (Sec. 3.5). According to the semi-hard scattering hypothesis, the one-dimensional residual shape change represented by parameter P in the fit function from higher to the lower power indices with collisions centrality is consistent with the modification of mini-jet structure in the medium created in the heavy ion collisions.

centrality	parameters				fitting error(%)			
	(d)	(c)	(b)	(a)	(d)	(c)	(b)	(a)
$\overline{N}$	115.5	424.9	790.2	983.0	———			
$\mathcal{S}$	1.19	1.22	1.25	1.27	8% systematic error			
$W = 0.6$, $y_{t0} = 3.2$								
$(\mathcal{S}\overline{N} - 1)\ A$	0.166	0.219	0.399	0.445	3.9	3.2	1.1	1.7
P	3.23	3.07	2.41	2.33	14.6	10.6	3.6	5.5
$(\mathcal{S}\overline{N} - 1)\ k$	-0.003	-0.007	0.039	0.050	>100	86	10	14
χ^2/DoF	$\frac{35.8}{32}$	$\frac{42.6}{32}$	$\frac{72.4}{32}$	$\frac{48.1}{32}$	———			
$W = 0.6$, y_{t0} also determined by simultaneous fit								
$(\mathcal{S}\overline{N} - 1)\ A$	0.156	0.214	0.412	0.461	4.4	3.8	1.5	2.3
P	3.25	3.12	2.39	2.31	14.7	11.0	3.5	5.3
$(\mathcal{S}\overline{N} - 1)\ k$	-0.007	-0.009	-0.033	-0.043	72.3	70.2	12.6	16.8
y_{t0}	3.14	3.18	3.23	3.23	0.6	0.6	0.3	0.4
χ^2/DoF	$\frac{31.8}{31}$	$\frac{42.0}{31}$	$\frac{66.3}{31}$	$\frac{44.9}{31}$	———			
$W = 0.8$, $y_{t0} = 32$								
$(\mathcal{S}\overline{N} - 1)\ A$	0.141	0.194	0.463	0.510	4.3	5.7	2.0	2.8
P	3.2	2.6	0.96	0.99	13.2	21.9	5.1	7.2
$(\mathcal{S}\overline{N} - 1)\ k$	-0.025	-0.045	-0.25	-0.27	23	27	4	6
χ^2/DoF	$\frac{51.5}{32}$	$\frac{81.5}{32}$	$\frac{284.5}{32}$	$\frac{130}{32}$	———			
$W = 0.4$, $y_{t0} = 32$								
$(\mathcal{S}\overline{N} - 1)\ A$	0.213	0.277	0.506	0.561	3.8	3.1	1.1	1.6
P	1.27	1.44	1.30	1.30	9.1	7.7	2.8	4.3
$(\mathcal{S}\overline{N} - 1)\ k$	-0.0065	-0.0012	-0.025	-0.033	>100	>100	19	25
χ^2/DoF	$\frac{95.5}{32}$	$\frac{105}{32}$	$\frac{320}{32}$	$\frac{149.5}{32}$	———			

Table 6.2: Parameters and fitting errors for one-dimensional residual model fits based on the semi-hard scattering hypothesis to CI transverse-momentum two-particle density ratios for (a) most-central (b) mid-central (c) mid-peripheral and (d) peripheral centrality classes.

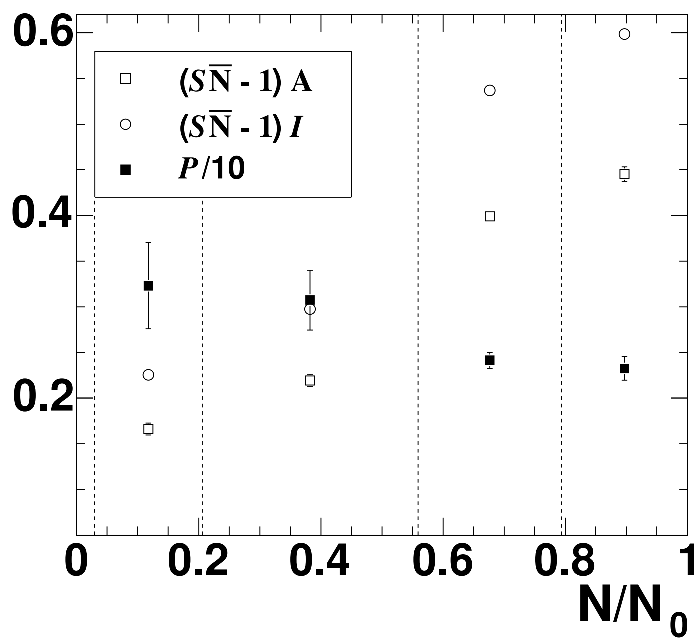

Figure 6.9: Centrality dependence of parameters from one-dimensional fits on residual projections of CI transverse two-particle density ratios. Parameters are $(\mathbb{S}\overline{N}-1)A$ (open square) and $P/10$ (closed square). $(\mathbb{S}\overline{N}-1)I$ (open circle) denote normalized integrated value of fit function without offset values over $0.4 < x_\Sigma/2 < 0.99$.

6.2 Dependence on (η, ϕ) Scales

From the study on the CI two-particle transverse momentum spaces of large axial momentum acceptance ($-1.3 < \eta < 1.3$, $-\pi < \phi < \pi$), we observed centrality dependencies of the large momentum scale correlation structure described by two-dimensional Lévy distribution and excess correlation structures appeared at higher p_t regions. Each correlation structure exhibited characteristic dependence on the centrality, and in this section, the axial momentum scale dependence are considered for the further source study of such correlations.

Azimuth and pseudorapidity differences ($\phi_\Delta \equiv \phi_1 - \phi_2$, $\eta_\Delta \equiv \eta_1 - \eta_2$) each are divided into two parts such that each acceptance bins include approximately the same half number of pairs: for azimuth angle differences (i) same-side pairs ($|\phi_\Delta| < \pi/2$), (ii) away-side pairs ($|\Delta\phi| > \pi/2$) and for pseudorapidity differences, (iii) small pseudorapidity difference pairs ($|\eta_\Delta| < 0.9$) and (iv) large pseudorapidity difference pairs ($0.9 < |\eta_\Delta| < 2.6$).

In Fig. 6.10, centrality dependence of the CI transverse-momentum two-particle density ratio for (i) same-side, (ii) away-side, (iii) small $|\eta_\Delta|$ and (iv) large $|\eta_\Delta|$ pairs are presented. The large-momentum-scale correlation structures are observed for all acceptance and centrality bins. The fitting procedures are the same as full acceptance results in the previous section and the data are parameterized with two-dimensional Lévy distribution model function (Eq. 6.1). Obtained parameters which characterize the large-scale curvature on the two-particle transverse momentum spaces are given in Table 6.3 and its

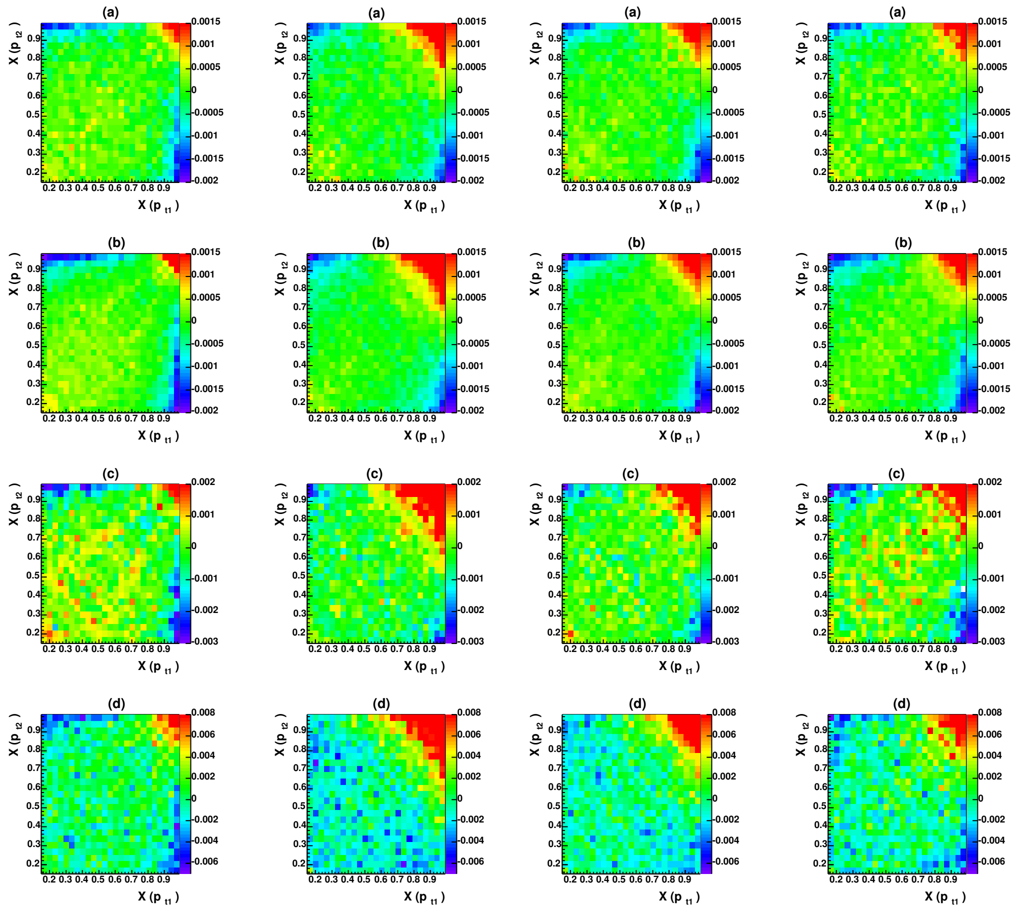

(i) $|\phi_\Delta| < \pi/2$ (ii) $|\phi_\Delta| > \pi/2$ (iii) $|\eta_\Delta| < 0.9$ (iv) $0.9 < |\eta_\Delta| < 2.6$

Figure 6.10: Centrality dependence of CI transverse-momentum two-particle density ratios in (i) same-side, (ii) away-side, (iii) small pseudorapidity difference ($|\eta_\Delta| < 0.9$) and (iv) large pseudorapidity difference ($0.9 < |\eta_\Delta| < 2.6$) for (a) most-central, (b) mid-central, (c) mid-peripheral and (d) peripheral centrality classes from the top to the bottom panels.

centrality dependencies are illustrated in Fig. 6.11 for each acceptance bins. Centrality development of parameters in all four acceptance regions show similar centrality dependence of increasing the negative saddle curvature along the difference direction $|(\mathcal{S}\overline{N}-1)\Delta(1/n)_\Delta|$ and the positive curvature along the sum direction $|(\mathcal{S}\overline{N}-1)\Delta(1/n)_\Sigma|$ decreases, however details changes significantly in each acceptance bin. The parameters depend on both axial momentum difference variables, but there is larger difference between parameters in different ϕ_Δ acceptance than in different η_Δ acceptance with defined acceptance bins. $|\Delta(1/n)_\Delta|$ values from different η_Δ acceptance show approximately constant ($\sim 10\%$) reduction for $|\eta_\Delta| < 0.9$ (Fig. 6.11, (iii)) and increase for pairs in $0.9 < |\eta_\Delta| < 2.6$ (Fig. 6.11, (iv)) from the value in full acceptance for four centrality classes, while $\Delta(1/n)_\Sigma$ does not show significant difference. In contrast, parameters obtained from away- and same-side azimuth difference acceptance presented in Fig. 6.11 (i, ii) show relatively large change in $\Delta(1/n)_\Sigma$ compare to $|\Delta(1/n)_\Delta|$ values.

The one-dimensional projection of fitting residuals onto x_Σ-axis are obtained and presented with the model function (Eq. 6.5) based on the semi-hard scattering hypothesis in Fig. 6.12. Best-fit parameters, χ^2/DoF and integrated values of fit function without offset are listed in the Table 6.4. The one-dimensional projection of residual structure also exhibit a common structure for all acceptance bins but significant difference in details. η_Δ dependence of the residual projections show the amplitude reduction for the large pseudorapidity pairs compare to the small η_Δ pairs and the difference is larger in

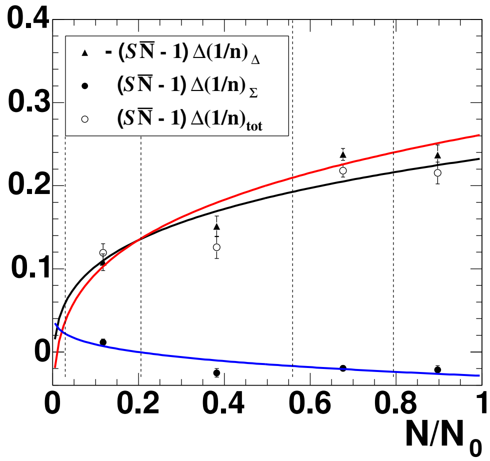

(i) Same-side ($|\phi_\Delta| < \pi/2$)

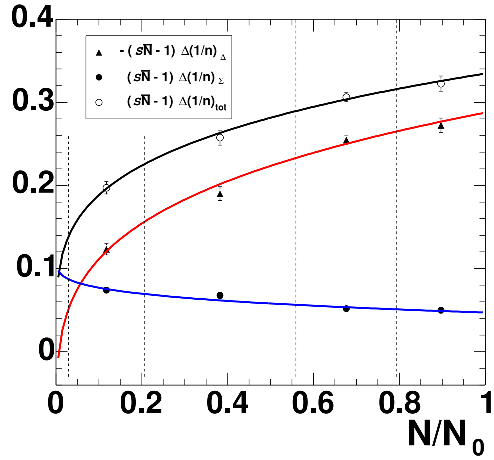

(ii) Away-side ($|\phi_\Delta| > \pi/2$)

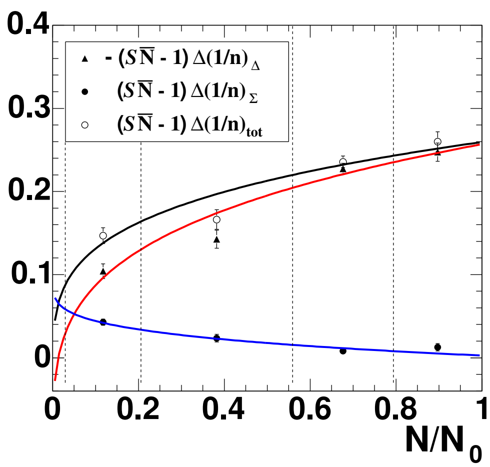

(iii) $|\eta_\Delta| < 0.9$

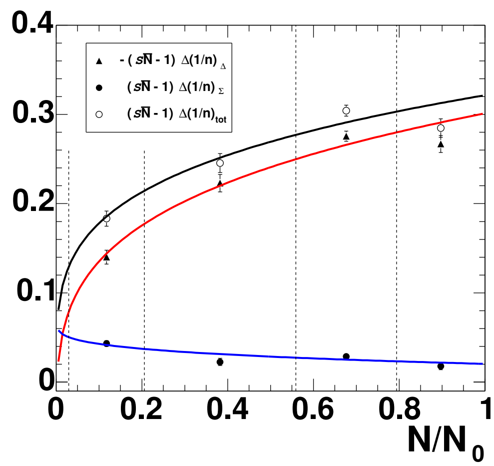

(iv) $0.9 < |\eta_\Delta| < 2.6$

Figure 6.11: Centrality dependence of extracted parameters from two-dimensional Lévy fit on the CI transverse two-particle density ratios in each acceptance bin. Parameters are $-(\mathcal{S}\overline{N} - 1)\Delta(1/n)_\Delta$ (closed triangle), $(\mathcal{S}\overline{N} - 1)\Delta(1/n)_\Sigma$ (closed circle) and $\Delta(1/n)_{total}$ (open circle), for (i) same-side ($|\phi_\Delta| < \pi/2$), (ii) away-side ($|\phi_\Delta| > \pi/2$), (iii) small pseudorapidity difference ($|\eta_\Delta| < 0.9$) and (iv) large pseudorapidity difference ($0.9 < |\eta_\Delta| < 2.6$) pairs.

peripheral events. However small difference between the residuals of the same- and away-side pairs is observed for all centrality classes. This study of axial momentum dependence of the CI transverse momentum correlation structure requires the finer acceptance bins with larger data statistics to conclude the correlation sources. But the observation of large acceptance dependence of correlation structure suggests that the more study of discrimination between hard and soft particle via its correlation contents with finer centrality classes and acceptance bins may reveal the precise correlation structure shifts associated with equilibration processes in heavy ion collisions to the lower pt region or to the larger axial momentum acceptances.

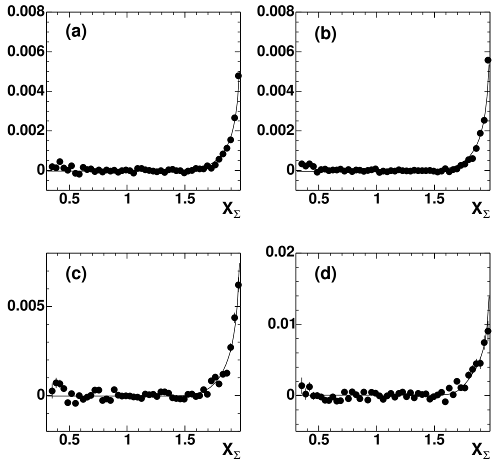

(i) Same-side ($|\phi_\Delta| < \pi/2$)

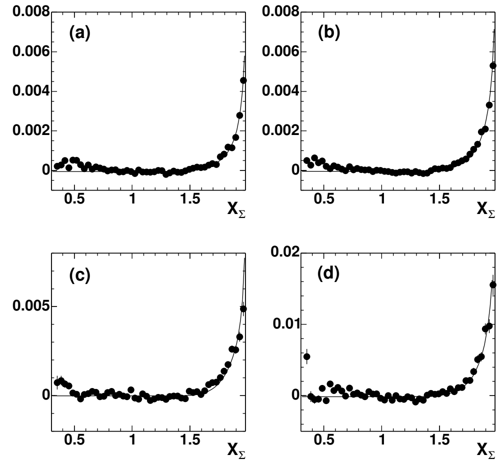

(ii) Away-side ($|\phi_\Delta| > \pi/2$)

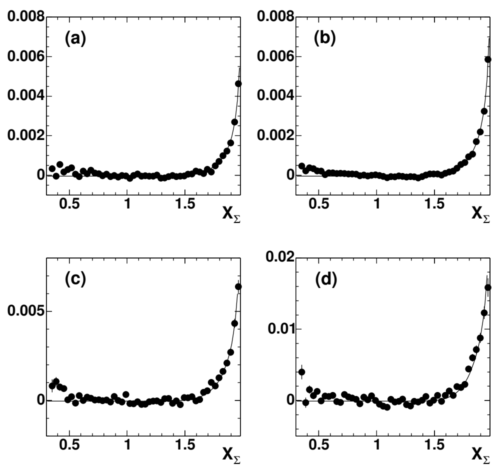

(iii) $\eta_\Delta < 0.9$

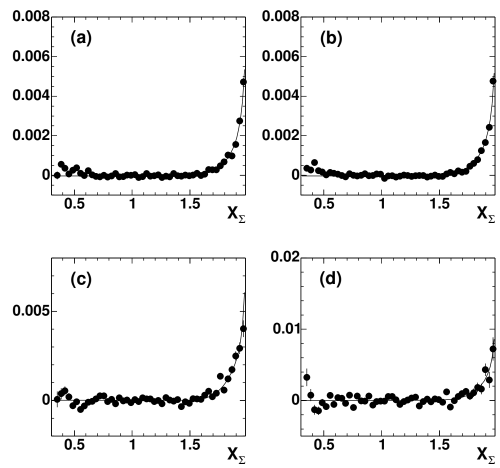

(iv) $0.9 < \eta_\Delta$

Figure 6.12: Centrality dependence of one-dimensional projections of residuals for CI transverse two-particle density ratios with fitting functions for different acceptance regions for (i) same-side ($|\phi_\Delta| < \pi/2$), (ii) away-side ($|\phi_\Delta| > \pi/2$), (iii) small pseudorapidity difference ($|\eta_\Delta| < 0.9$) and (iv) large pseudorapidity difference ($0.9 < |\eta_\Delta| < 2.6$) pairs. Each set include plots for (a) most-central, (b)mid-central, (c)mid-peripheral and (d) peripheral centrality classes.

centrality	parameters (d)	(c)	(b)	(a)	fitting error(%) (d)	(c)	(b)	(a)
$\overline{N}$	115.5	424.9	790.2	983.0	————			
$\mathcal{S}$	1.19	1.22	1.25	1.27	8% systematic error			
same-side, $\lvert\phi_\Delta\rvert < \pi/2$								
$(\mathcal{S}\overline{N}-1)\Delta(\frac{1}{n})_\Delta$	-0.108	-0.151	-0.238	-0.237	9.3	8.2	3.0	5.1
$(\mathcal{S}\overline{N}-1)\Delta(\frac{1}{n})_\Sigma$	0.011	-0.025	-0.020	-0.022	36.7	20.0	15.2	23.4
$(\mathcal{S}\overline{N}-1)\Delta(\frac{1}{n})_{tot}$	0.119	0.126	0.218	0.215	9.1	10.7	3.6	6.1
$(\mathcal{S}\overline{N}-1)\mathcal{C}$	0.020	0.244	0.297	0.291	68.9	7.5	3.6	6.2
χ^2/DoF	$\frac{286.3}{286}$	$\frac{325.7}{286}$	$\frac{341.4}{286}$	$\frac{329.9}{286}$	————			
away-side, $\lvert\phi_\Delta\rvert > \pi/2$								
$(\mathcal{S}\overline{N}-1)\Delta(\frac{1}{n})_\Delta$	-0.123	-0.190	-0.255	-0.272	7.8	6.2	2.8	4.4
$(\mathcal{S}\overline{N}-1)\Delta(\frac{1}{n})_\Sigma$	0.074	0.068	0.052	0.050	5.4	7.2	5.7	9.9
$(\mathcal{S}\overline{N}-1)\Delta(\frac{1}{n})_{tot}$	0.197	0.258	0.306	0.322	5.4	7.2	5.7	9.9
$(\mathcal{S}\overline{N}-1)\mathcal{C}$	-0.283	-0.235	-0.128	-0.097	4.7	7.2	8.2	18.2
χ^2/DoF	$\frac{371.9}{286}$	$\frac{331.2}{286}$	$\frac{514.4}{286}$	$\frac{382.1}{286}$	————			
small η_Δ, $\lvert\eta_\Delta\rvert < 0.9$								
$(\mathcal{S}\overline{N}-1)\Delta(\frac{1}{n})_\Delta$	-0.104	-0.143	-0.227	-0.247	8.5	7.6	2.9	4.4
$(\mathcal{S}\overline{N}-1)\Delta(\frac{1}{n})_\Sigma$	0.043	0.024	0.008	0.013	8.6	19.2	33.1	36.4
$(\mathcal{S}\overline{N}-1)\Delta(\frac{1}{n})_{tot}$	0.147	0.166	0.236	0.260	6.5	7.1	3.0	4.6
$(\mathcal{S}\overline{N}-1)\mathcal{C}$	-0.153	-0.041	0.099	0.099	8.1	38.4	9.8	16.5
χ^2/DoF	$\frac{340.5}{286}$	$\frac{351.0}{286}$	$\frac{454.3}{286}$	$\frac{377.5}{286}$	————			
large η_Δ, $\lvert\eta_\Delta\rvert > 0.9$								
$(\mathcal{S}\overline{N}-1)\Delta(\frac{1}{n})_\Delta$	-0.140	-0.223	-0.276	-0.267	7.9	6.2	2.9	5.1
$(\mathcal{S}\overline{N}-1)\Delta(\frac{1}{n})_\Sigma$	0.043	0.023	0.029	0.018	10.7	25.5	11.6	31.5
$(\mathcal{S}\overline{N}-1)\Delta(\frac{1}{n})_{tot}$	0.183	0.246	0.304	0.285	6.6	6.1	2.9	5.1
$(\mathcal{S}\overline{N}-1)\mathcal{C}$	-0.097	0.051	0.057	0.087	15.7	39.2	20.7	22.9
χ^2/DoF	$\frac{332.4}{286}$	$\frac{323.4}{286}$	$\frac{343.9}{286}$	$\frac{346.6}{286}$	————			

Table 6.3: Parameters and fitting errors for two-dimensional model fits to CI scale-dependent transverse-momentum two-particle density ratios with fixed parameters $T_0 = 0.2$ GeV and n=33 ($1/n = 0.03$) for (a) most-central (b) mid-central (c) mid-peripheral and (d) peripheral centrality classes.

centrality	parameters (d)	(c)	(b)	(a)	fitting error(%) (d)	(c)	(b)	(a)
$\overline{N}$	115.5	424.9	790.2	983.0	————			
$\mathcal{S}$	1.19	1.22	1.25	1.27	8% systematic error			
same-side, $\|\phi_\Delta\| < \pi/2$								
$(\mathcal{S}\overline{N}-1)\ A$	0.123	0.252	0.349	0.413	7	4	2	3
P	4.5	2.9	2.4	2.6	26	14	7	9
$(\mathcal{S}\overline{N}-1)\ k$	0.009	-0.012	-0.040	-0.034	75	77	16	29
χ^2/DoF	$\frac{76}{32}$	$\frac{111}{32}$	$\frac{315}{32}$	$\frac{140}{32}$	————			
$(\mathcal{S}\overline{N}-1)I$	0.556	0.469	0.341	0.170	————			
away-side, $\|\phi_\Delta\| > \pi/2$								
$(\mathcal{S}\overline{N}-1)\ A$	0.208	0.262	0.464	0.479	4	4	1	2
P	2.6	3.1	2.4	2.2	12	14	4	7
$(\mathcal{S}\overline{N}-1)\ k$	-0.020	-0.004	-0.038	-0.065	35	>100	15	16
χ^2/DoF	$\frac{76}{32}$	$\frac{144}{32}$	$\frac{292}{32}$	$\frac{127}{32}$	————			
$(\mathcal{S}\overline{N}-1)I$	0.644	0.625	0.355	0.280	————			
small η_Δ, $\|\eta_\Delta\| < 0.9$								
$(\mathcal{S}\overline{N}-1)\ A$	0.225	0.290	0.451	0.449	4	3	1	2
P	3.1	2.7	2.4	2.3	15	11	4	7
$(\mathcal{S}\overline{N}-1)\ k$	-0.012	-0.018	-0.044	-0.058	53	48	12	16
χ^2/DoF	$\frac{128}{32}$	$\frac{116}{32}$	$\frac{122}{32}$	$\frac{114}{32}$	————			
$(\mathcal{S}\overline{N}-1)I$	0.604	0.607	0.391	0.305	————			
large η_Δ, $\|\eta_\Delta\| > 0.9$								
$(\mathcal{S}\overline{N}-1)\ A$	0.076	0.204	0.336	0.441	14	6	2	3
P	3.0	3.4	2.5	2.3	43	17	7	9.5
$(\mathcal{S}\overline{N}-1)\ k$	0.002	0.004	-0.032	-0.039	>100	>100	20	30
χ^2/DoF	$\frac{64}{32}$	$\frac{74}{32}$	$\frac{121}{32}$	$\frac{86}{32}$	————			
$(\mathcal{S}\overline{N}-1)I$	0.593	0.452	0.279	0.103	————			

Table 6.4: Parameters and fitting errors for one-dimensional residual model fits to scale-dependent transverse-momentum two-particle density ratios for (a) most-central (b) mid-central (c) mid-peripheral and (d) peripheral centrality classes with fixed parameters $W = 0.6$ and $y_{t0} = 3.2$. Fitting range is $0.8 < x_\Sigma < 1.98$. Integrated values over the fit range are given in the last row.

6.3 Charge Dependent (CD) Correlations

The Charge Dependent (CD) two-particle density ratio is constructed by subtracting unlike-sign (US) two-particle density ratio from like-sign (LS) distribution ($R^{CD} = R^{LS} - R^{US}$). In Fig. 6.13, centrality dependence of CD two-particle density ratios as function of $x(p_t)$ after normalization by the mean multiplicity in each centrality bin are presented. The small-momentum-scale correlations are eliminated according to Sec. 5.7.

The large-momentum-scale correlation structure on the CD two-particle transverse momentum spaces includes a concave downward shape along x_Σ diagonal observed for all centrality classes. With the observation of small dependence on x_Δ, the dimension of the data can be reduced by projecting the two-dimensional space onto x_Σ diagonal axis by taking average of bin contents along difference variable direction without information loss. Obtained projected CD correlations are shown in Fig. 6.14 with a fitting function,

$$f_{CD}(x_\Sigma) = \mathcal{E}(\frac{x_\Sigma}{2}) \exp(\frac{\frac{x_\Sigma}{2} - 1}{\mathcal{W}}) + \mathcal{D}. \tag{6.6}$$

Obtained best-fit parameters are listed in Table 6.5. A small centrality dependence of amplitude parameter is observed in the CD transverse two-particle correlation consistent with the charge dependent event-by-event $< p_t >$ fluctuation study (Sec. 3.5). The CD structure at the large x_Σ is suggestive of charge configuration in the high-p_t particles or minijets. The study of a slight correlation shape change requires the more data statistics and left for the future study.

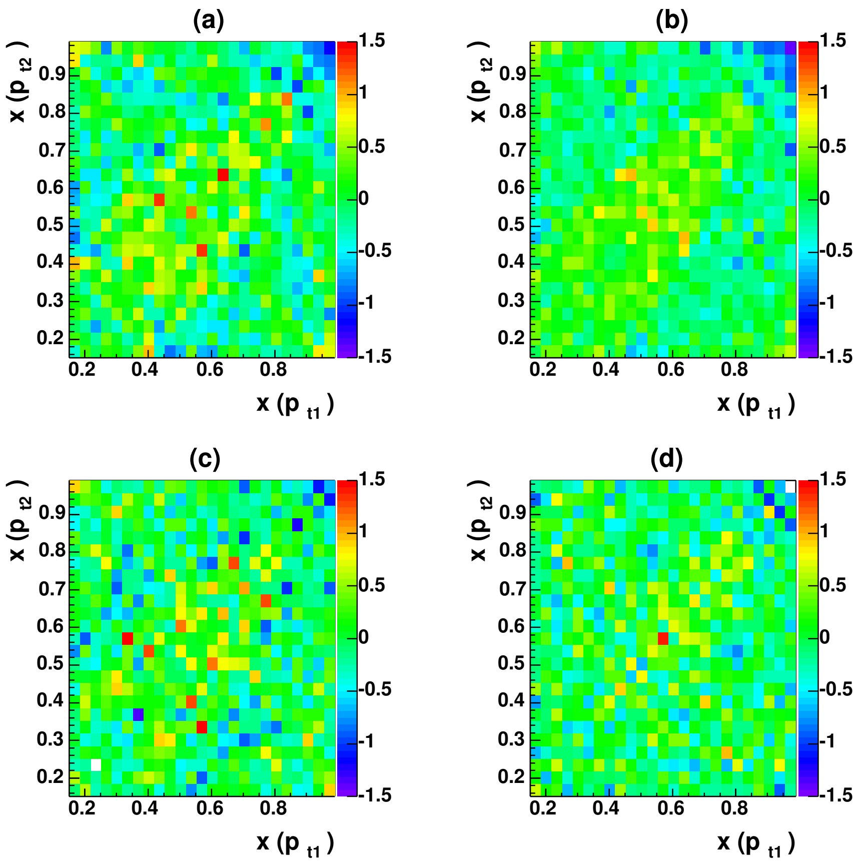

Figure 6.13: Centrality dependence of CD transverse two-particle density ratios in Au-Au collisions at $\sqrt{s_{NN}}$ = 130 GeV for (a) most-central (b) mid-central (c) mid-peripheral and (d) peripheral centrality bins.

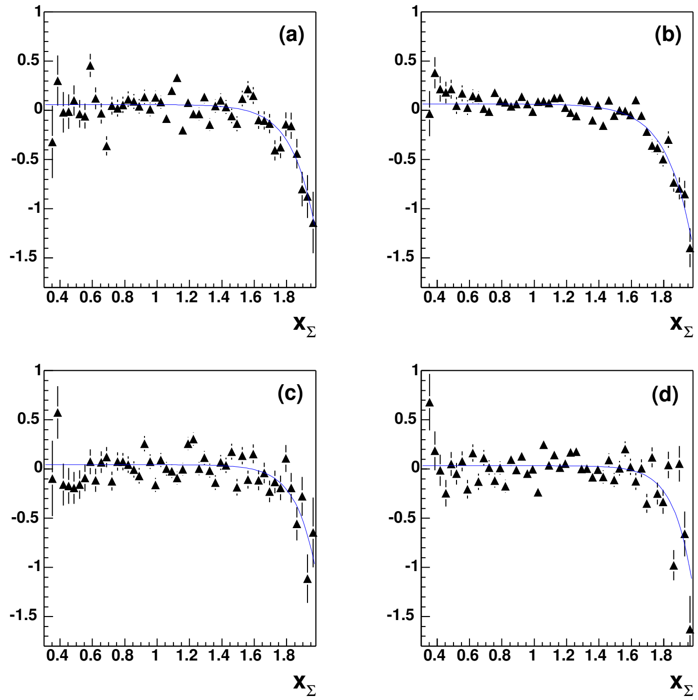

Figure 6.14: Projections of normalized CD transverse two-particle density ratios in Au-Au collisions at $\sqrt{s_{NN}} = 130$ GeV for (a) most-central (b) mid-central (c) mid-peripheral and (d) peripheral centrality bins.

centrality	parameters				fitting error(%)			
	(d)	(c)	(b)	(a)	(d)	(c)	(b)	(a)
$\overline{N}$	115.5	424.9	790.2	983.0	————			
$\mathcal{S}$	1.19	1.22	1.25	1.27	8% systematic error			
$(\mathcal{S}\overline{N}-1)\ \mathcal{E}$	-1.46	-1.27	-1.64	-1.50	36.5	34.1	13.5	6.2
$\mathcal{W}$	0.062	0.066	0.088	0.076	32.5	38.2	14.1	8.5
$(\mathcal{S}\overline{N}-1)\ \mathcal{D}$	0.034	0.044	0.065	0.059	57.4	66.9	24.4	36.8
χ^2/DoF	$\frac{70.4}{32}$	$\frac{44.5}{32}$	$\frac{45.7}{32}$	$\frac{50.5}{32}$	————			

Table 6.5: Parameters and fitting errors for model fits to one-dimensional projections of CD transverse-momentum two-particle density ratios for (a) most-central (b) mid-central (c) mid-peripheral and (d) peripheral centrality classes.

6.4 Systematic Study

In this section, possible sources of uncertainties on the transverse-momentum two-particle density ratios are considered and evaluated.

6.4.1 Reconstruction Effects

Particle momentum is determined by event reconstruction software. Size of uncertainty associated with this reconstruction process is estimated by comparing two-particle density ratios of events from pure event-generating simulation and from after detector-response simulation and offline event reconstruction.

The transverse two-particle density ratios $R_{sim}(x(p_{t1}), x(p_{t2}))$ from the simulation which reproduces realistic single-particle p_t distribution similar to Fig. 5.9 with null two-particle correlation signal is shown in Fig. 6.15. The upper right panels in Fig. 6.15 (i) and (ii) show R_{sim} before and after offline event reconstructions respectively. It is observed that there is no apparent correlation structure on both plots with a small change in fluctuations around 1. The upper left panels in the figures, distributions of standard deviation $\sigma_{R_{sim}}$ or statistical error based on the number of pairs in each bin are presented. The relative variance and pair entry in each bin for CI two-particle density ratio, for example, is expressed as $\frac{\sigma^2_{R_{CI}}}{R^2_{CI}} = (\frac{1}{N_{sib}} + \frac{1}{N_{mix}})$ where N_{sib} and N_{mix} indicate the number of sibling and mixed CI pairs in the bin, and thus the statistical error changes bin-by-bin as the pair entry vary. Difference in the statistical error distributions of (i) and (ii) implies that less number of particles

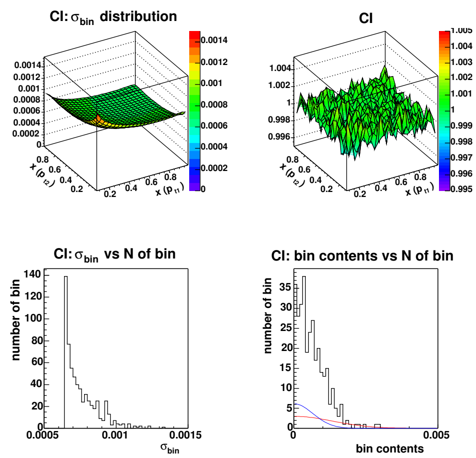

(i) Input simulation data

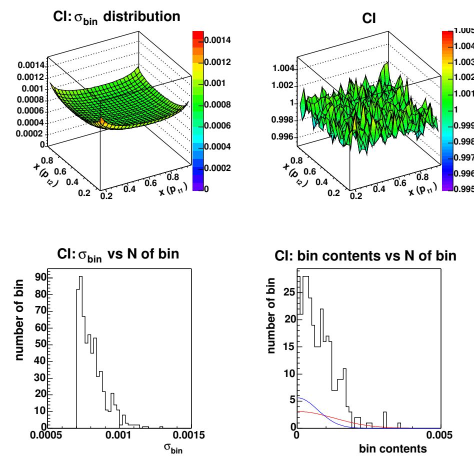

(ii) Reconstructed simulation data

Figure 6.15: Comparison of CI transverse two-particle density ratios from 1000 simulation events (i) before and (ii) after offline event reconstructions without correlation signals. Upper right panel: two-particle density ratio, upper left panel: statistical error distribution, lower right panel: bin contents vs. number of bins and lower right panel: statistical error vs. number of bins.

contribute to (ii) which causes the increased fluctuations on reconstructed pair density ratios. But it confirms that it does not affect correlation structure in two-particle density ratio spaces. The lower plots represent corresponding bin-number distributions of $\sigma_{R_{sim}}$ (left-hand panels) and R_{sim} (right-hand panels), solid lines indicate gaussian functions with the maximum (blue) and minimum (red) bin variances $\sigma_{R_{sim}}$.

The maximum standard error in real data before normalization are 1.2×10^{-4}, 1.0×10^{-4}, 2.8×10^{-4} and 8.5×10^{-4} from most-central to peripheral centrality classes respectively at the lower left or upper right corner of the transverse two-particle density ratio and the minimum standard errors are 0.8×10^{-4}, 0.8×10^{-4}, 2.2×10^{-4} and 6.0×10^{-4} near center ($x(p_{t1}) \sim x(p_{t2}) \simeq 0.5$) for CI correlation space. The standard errors for CD correlation are about twice of the error sizes in CI correlation space.

6.4.2 Charge Symmetry

Study of CI and CD two-particle correlation structures by combining and subtracting LS and US distributions presupposes charge symmetry of correlations, *i.e.*, invariance of correlation structure under exchange of charge sign of particles in each LS and US two-particle density ratio. The assumption of charge-symmetry is confirmed in this section.

Transverse two-particle density ratio of each LS and US charge combinations are shown in Fig. 6.16 (i) and (ii). The right-hand panels represent the difference distributions of the two-particle density ratio of each charge sign combinations. The bottom plots (iii, iv) are bin-number distributions of differences. Small correlation structure on the difference distribution plots and the bin-number histograms which agree with statistical distribution show that the charge-combination symmetry is achieved in both LS and US transverse two-particle correlations.

6.4.3 Pair Inefficiency Corrections

The pair reductions due to overlap or closeness of reconstructed hit positions in the TPC volume are categorized into *track-splitting* and *pair-*

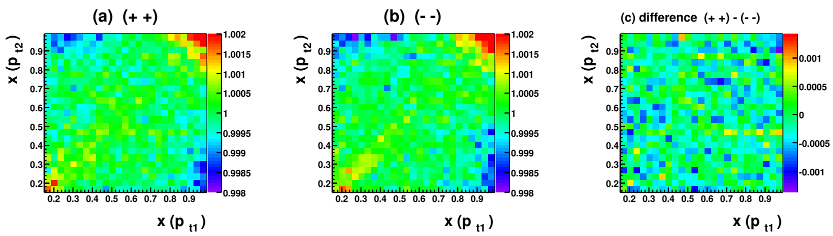

(i) $(+,+)$ and $(-,-)$ pair-charge combinations and their difference

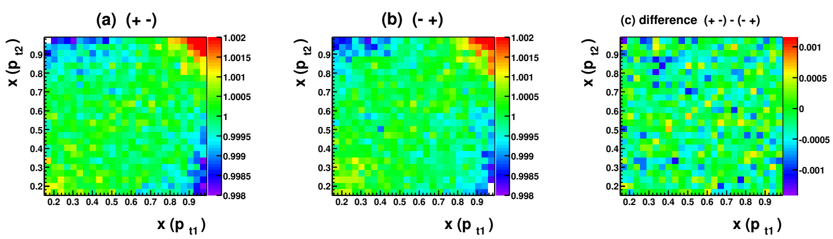

(ii) $(+,-)$ and $(-,+)$ pair-charge combinations and their difference

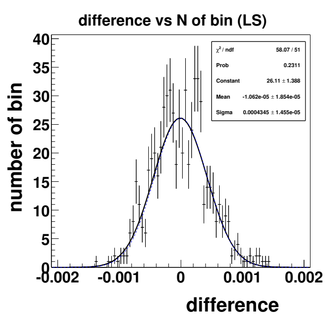

(iii) Difference vs number of bins (LS)

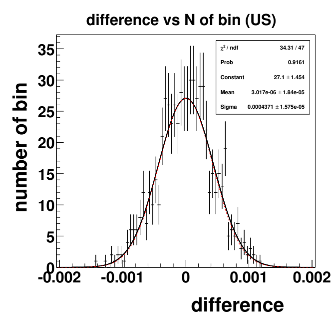

(iv) Difference vs number of bins (US)

Figure 6.16: Transverse two-particle density ratios of (i,a) $(+,+)$, (i,b) $(-,-)$, (ii,a) $(+,-)$ and (ii,b) $(-,+)$ charge combinations. Distributions of bin content difference for each charge combinations (i,ii-c) are also presented. In bin-number distributions of difference (iii,iv), solid lines denote fitted gaussian functions. The obtained variances are compared with average statistical error in the density ratios $\overline{\sigma}_{LS} \simeq \overline{\sigma}_{US} = 0.00043$.

merging, and are corrected according to the pair separations (Sec.5.3). In this section, appearance of such effects and the appropriateness of the correction in the transverse two-particle density ratio are reviewed.

The region of two-particle transverse momentum space in which track-splitting or pair-merging occur and its magnitude are estimated by Monte Carlo simulation. The result from the pair inefficiency simulation for central events modeled with pair geometrical separations [74] is shown in Fig. 6.17. The anti-correlation near the diagonal is observed. It is due to pair-merging

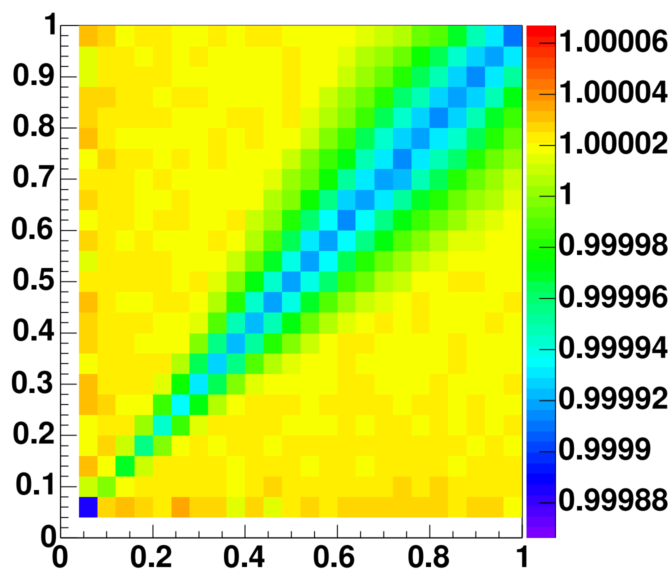

Figure 6.17: Contributions from pair-merging and track-splitting effects in CI transverse two-particle density ratios estimated by Monte Carlo simulations as a function of $x(p_{t1})$ (x-axis) and $x(p_{t2})$ (y-axis).

and caused by pairs with similar track geometry and thus have the small p_t

differences. It is expected that a weak anti-correlation due to track-splitting which is not much dependent on p_t difference but occurs only with crossing geometry, distributes over a wide range in the plot. The magnitude of pair-merging effect is estimated to be about -1.0×10^{-4} at the largest along the diagonal, and that of due to track-splitting is unclear because it distributes constantly over full p_t range.The track-splitting effect transverse two-particle density ratio for real data are seen by comparing R of the pairs which have and do not have crossing geometries.

In the left-hand panels of Fig. 6.18, the two-particle distributions of (+,+) and (−,−) pair-charge combinations with only positive $\Delta\phi$ are shown. For positive ϕ_Δ pairs, crossing geometry is only formed with negative $p_{t,\Delta}$ for (+, +) charged pairs and with positive $p_{t,\Delta}$ for (−, −) charged pairs. The difference between positive and negative $p_{t,\Delta}$ region, above and below x_Σ diagonals, on the two-particle density ratios are observed. The contrast is shown on the middle plots. The middle plots are obtained by subtracting two-particle density ratio (left-hand panel) reflected about x_Σ diagonal from the two-particle density ratio before the reflection. The projections of the contrast plots (middle panels) on the difference (x_Δ) diagonal axis are given in the right-hand panels. It is observed that the splitting effect increase with x_Δ from -1.0×10^{-4} at $x_\Delta = 0.1$ to -4.0×10^{-4} at $x_\Delta = 0.8$ for the most-central class. The effect in full x_Δ is the half of the observed value ($\sim -1.7 \times 10^{-4}$).

The track-splitting contributions are removed by pair-wise cut described in Sec. 5.3. The same plots after the track-crossing cut are shown in Fig. 6.19.

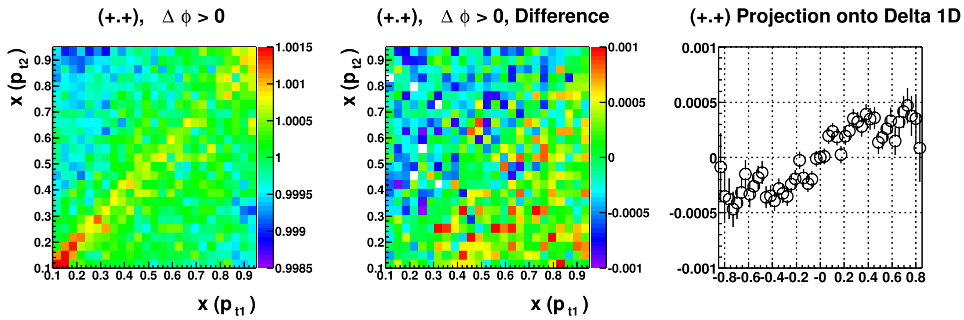

(i) $(+,+)$ pair charges

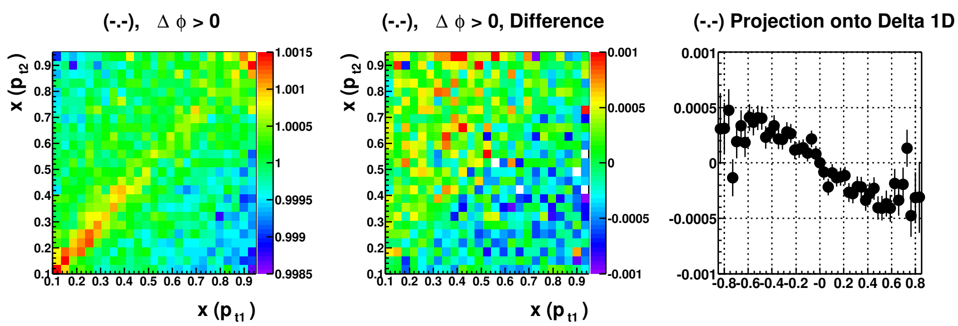

(ii) $(-,-)$ pair charges

Figure 6.18: Two-particle distributions of (i) $(+,+)$ and (ii) $(-,-)$ pair-charge combinations with positive ϕ_Δ (left-hand panels). The difference in positive and negative $p_{t,\Delta}$ indicates the track-crossing effect before the pair-wise track-splitting cut is applied. The middle plots shows difference distribution in positive and negative $p_{t,\Delta}$ sign regions, and are obtained by subtracting two-particle density ratio (left-hand panel) reflected about x_Σ diagonal from the two-particle density ratio. The projections of the difference plots (middle plots) on the difference (x_Δ) axis are given in the right-hand panels.

It is observed that the difference dependent on x_Δ is removed by the cut and distribute around zero with some fluctuations. Comparing the right-hand panels in Fig. 6.18 and Fig. 6.19, we observe that the cut successfully removes the pair-crossing effect however uncertainty associated with track-splitting removal of a quarter of effect at the maximum, *i.e.*, $\frac{1.0}{4} \times 10^{-4}$ for $|x_\Delta| < 0.05$, $\frac{2.0}{4} \times 10^{-4}$ for $0.05 < |x_\Delta| < 0.3$ and $\frac{3.5}{4} \times 10^{-4}$ for $0.3 < |x_\Delta| < 0.8$.

The evaluation of merging effect removal which only associated with the small $p_{t,\Delta}$ pairs, is difficult because the momentum region are affected by the small-momentum-scale Bose-Einstein and Coulomb correlations of the opposite correlation direction. However it is roughly estimated by making use of comparison among the two-particle density ratios with different merging-pair cut parameters for LS and US pairs, because pair-merging occurs with the pair with similar shape, LS pairs are mainly affected. In Fig. 6.20, upper 5 plots show two-particle density ratio with the average pair separation cut parameters of, from left to right, 0, 5, 7.5, 10 and 12.5 cm for LS (i) and US (ii). In the plots, track-splitting are already removed and the cut also reduces the merging effect. Each lower plot displays the difference between the two-particle density ratios with different parameters, which is obtained by subtracting bin-by-bin contents of two-particle density ratio with the larger merging cut parameter from the two-particle density ratios using the next smaller cut parameter.

The lower left plot in Fig. 6.20 (i), difference between the two-particle density ratio without merging cut and 5 cm average separation cut for LS

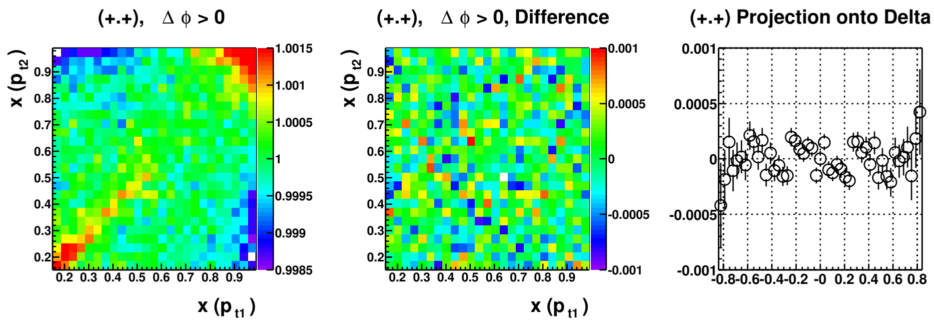

(i) $(+,+)$ pair-charge combination

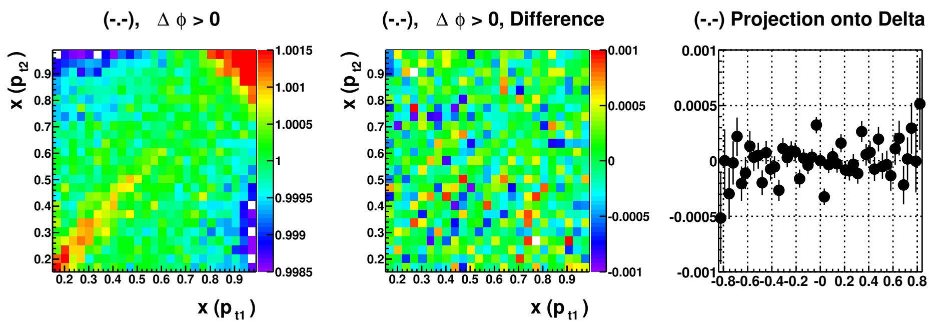

(ii) $(-,-)$ pair-charge combination

Figure 6.19: Two-particle distributions of (i) $(+,+)$ and (ii) $(-,-)$ pair-charge combinations with positive ϕ_Δ, after track-crossing separation cut of $d_t^{mid} > 30$ cm and $d_z^{mid} > 10$ cm for pairs which have crossing geometries. The middle plots shows the contrast of different $p_{t,\Delta}$ sign regions, and are obtained by subtracting two-particle density ratio (left-hand panel) reflected about x_Σ diagonal from the two-particle density ratio before the reflection. The projections of the contrast plots (middle plots) on the difference (x_Δ) diagonal axis are given in the right-hand panels

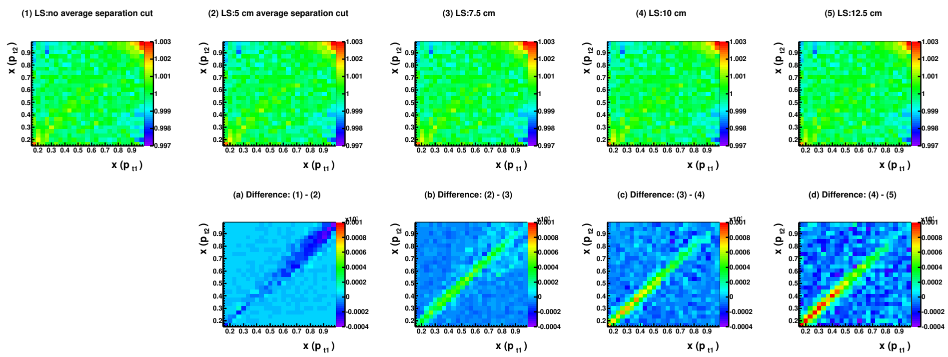

(i) LS

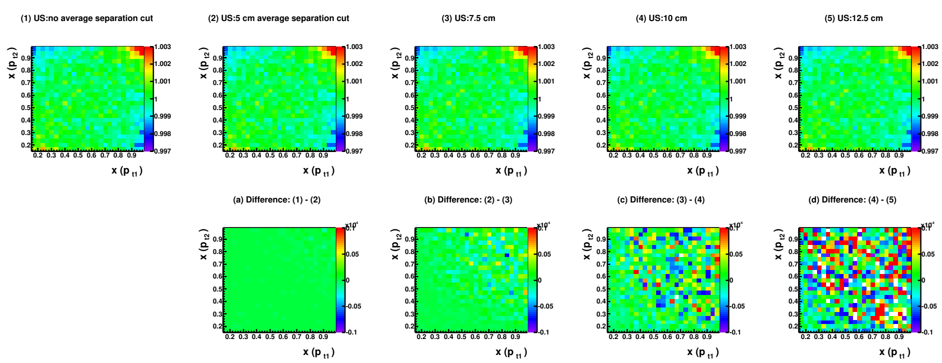

(ii) US

Figure 6.20: Effect of merging-cut appeared on transverse two-particle density ratios for (i) LS and (ii) US pairs. Upper plots present the transverse two-particle density ratio with different merging-cut parameter, from left to the right merging-pair cut parameters are increased. Lower plots display the removed effect by increasing cut parameters (see the texts).

pairs, shows the merging affected region of the size $\sim -4.0 \times 10^{-5}$ by dark blue color of negative correlation. The negative structure and observation that no structure appears for US pair spaces (ii) are consistent with the picture that the negative structure for the LS pairs are due to pair-merging removed by 5cm track average separation anti-merging pair cut. With cut parameter increase, the effect are canceled by the larger positive correlations due to small-momentum-scale correlations.This picture also agrees with the region shown in the result from Monte Carlo simulation (Fig. 6.17). The anti-merging average separation of 10 cm are used in the actual analysis, which is sufficient to remove the pair-merging effect without sacrificing a large number of good pairs. The LS lower difference plots showing the effect due to increased merging-pair cut parameters confirms that the cut dose not affect large-scale correlation structure except a slight removal of positive correlation along diagonal line due to the BE/Coulomb positive correlations.

6.4.4 Small-Momentum-Scale Correlation Correction

Contributions from the Bose-Einstein and Coulomb correlations are estimated by Monte Carlo simulation [74] and shown in Fig. 6.21 for central CI transverse two-particle momentum space as function of $x(p_{t1})$ (x-axis) and $x(p_{t2})$ (y-axis). However most of the Bose-Einstein and Coulomb correlations are expected to be already removed by the merging/splitting pair-wise cuts.In Fig. 6.22, the transverse two-particle density ratios before (left-hand panels) and after (middle panels) the small-momentum-scale correlation cut described

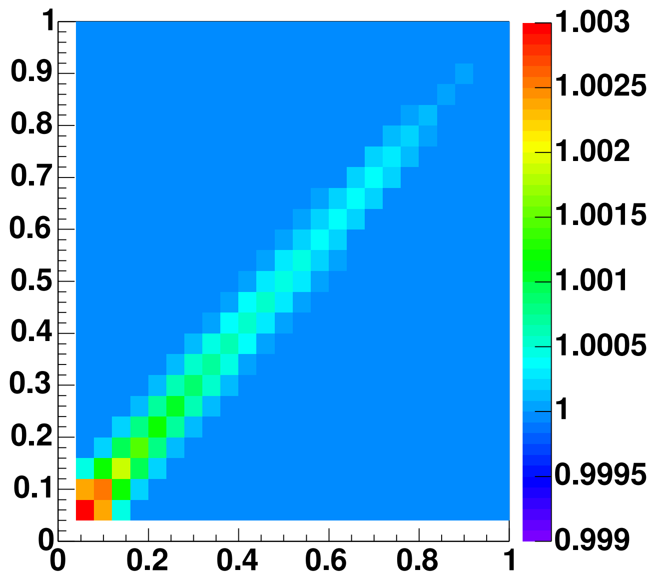

Figure 6.21: Effect of small-momentum-scale correlation on the CI transverse two-particle density ratio estimated by Monte Carlo simulation as function of $x(p_{t1})$ (x-axis) and $x(p_{t2})$ (y-axis).

in Sec. 5.7 and difference distribution (a)$-$(b) (right-hand panels) are presented.

The figure confirms that most of small-momentum-scale correlations are removed by anti-merging cut and the cut is not affecting the large-scale structure in which we are interested. This procedure removes the small-momentum-scale correlations but we would expect the similar size of uncertainty associated with removal as observed for pair-splitting removal (Sec. 6.4.3) of a quarter of small-momentum-scale correlation estimated by Monte Carlo simulation at the maximum, the systematic error for central class, $\frac{3.0}{4} \times 10^{-3}$ for the region

$x(p_{t1}), x(p_{t2}) < 0.1$, $\frac{1.0}{4} \times 10^{-3}$ for the region $|x_\Delta| < 0.1$ and $|x_\Sigma| < 1.7$ are assigned, and negligible for the rest of part.

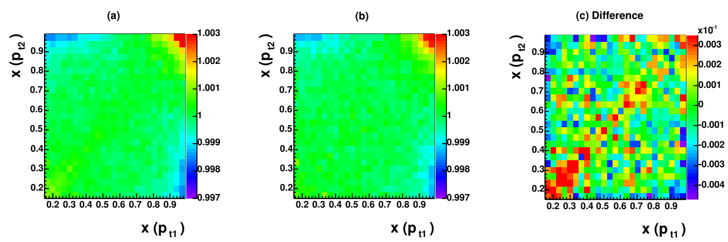

(i) CI

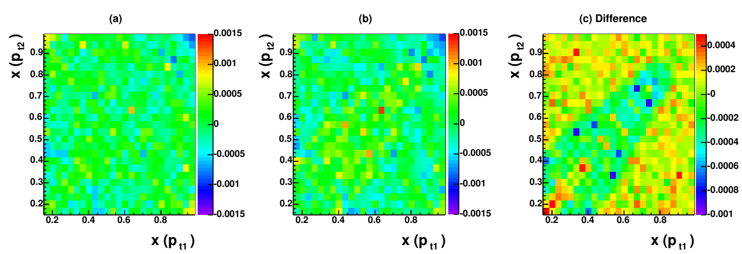

(ii) CD

Figure 6.22: Transverse two-particle density ratios (a) before and (b) after the small-momentum-scale correlation cut for CI (i) and CD (ii). The difference are presented in (c).

6.4.5 Background Contributions

There are systematic uncertainties from background contributions in a data and these contributions in the momentum acceptance under study are extensively studied for single-particle spectra analysis [68]. The main sources of background are electron background from photon conversion (Ex. π^0 (decay) $\Rightarrow \gamma + \gamma$; $\gamma + N$(detector material) $\Rightarrow e^+ + e^-$), decay products (Ex. ρ^0, ω, $K_s^0 \Rightarrow \pi^+ + \pi^-$) or the secondary particles produced by the interaction with detector material (Ex. π + N(detector material) $\Rightarrow p + \pi$).

The contribution from these backgrounds in the results of two-particle correlation analysis are estimated with Monte Carlo simulation using the estimated background to primary particle ratio in single-particle spectra [69]. The electron background to true primary ratio in year-1 data is small ($< 1\%$) for the p_t region larger than 0.4 GeV/c, and $\sim$ 10% at $p_t = 0.2$ GeV/c which decreases exponentially with increasing p_t. Thus the effect from electron contamination due to photon conversions mainly contributes at low p_t region. The hadronic background aggregates ~7% of the true primary particles for the p_t range from 0.4 to 2 GeV/c, with a small increase to about 10% at the minimum p_t value of 0.15 GeV/c for this analysis.

The estimation of background correlation contribution in two-particle density ratios require the correlation models among background secondaries and between parent and secondaries. With known single-particle background-particle to primary-particle ratio A, the contribution to the two-particle spaces are estimated from the background-pair to primary-pair ratio A^2 and background-primary-pairs $2A$.

The e^+e^- pairs emerge at very small opening angles ($< 1°$) [80] which are partially removed by pair-merging cuts of average pair separation and the small-momentum-scale correlation correction of pair p_t differences. The transverse momentum correlation among background- pairs and background-primary pairs are modeled by Bethe-Heitler differential cross section [80, 81]. The contribution from correlation among e^+e^- pairs are negligible in the two-particle transverse momentum space because of the smallness of e^+e^- to primary-pair ratio which is less than 1% at the maximum. The contribution from the correlation between primary-parent and background-daughter particles is also negligible in two-particle transverse momentum space because of small correlation among primary particles and between primary π^0, for example, to the observed electrons in low p_t range. These expectations are also confirmed by the Monte Carlo simulation [81]. The knock-out protons from the beam pipe and other detector material could contribute to two-particle correlation for $(+,+)$ charged-pair but not $(-,-)$ pairs. Thus the negligible difference between LS two-particle correlation of different charges (Sec. 6.4.2) indicate that the proton knock-out contamination is negligible for present purpose.

The main contribution are expected from the transverse momentum correlations among hadronic secondary decay products. Similar to the consideration of electron contamination, the contribution from correlation between daughters is negligible due to the relatively small number of such pairs in the sibling pair sample. If the decay particles are completely uncorrelated with the other primaries, the contribution from parent and 7% daughter particles introduces dilution of the correlation signal by $(1-0.07)^2$. On the other hand, if the contaminants remain fully correlated with the primaries, then adding in this 7% background has no effect on the correlation signal. Because of the uncertainly associated with unknown parent-daughter correlation in the hadronic background, we assign a half of difference between these two extreme cases as the systematic error. For two-particle correlations this procedure leads to a 16% error $x(p_t) < 0.4$ and 7% systematic uncertainty elsewhere. Based on the spectra analysis, we assume the same contamination fraction for all centralities.

The contribution from resonance decays (ρ^0, ω, η) are estimated by Monte Carlo simulation [82] and presented in Fig. 6.23. It is shown that the effect, the positive correlation at $|x_\Delta| > 0.8$ and negative contribution $|x_\Sigma| < 1.2$, have a tendency to decrease the large-scale saddle-shaped structure.

6.4.6 Mixed-Event Selections

The reference two-particle distributions, the mixed-pair distributions are constructed from the pairs taken from events of close properties as described in Sec. 5.5. The effect from incomplete construction of reference mixed-pair distribution are considered by comparing two-particle density ra-

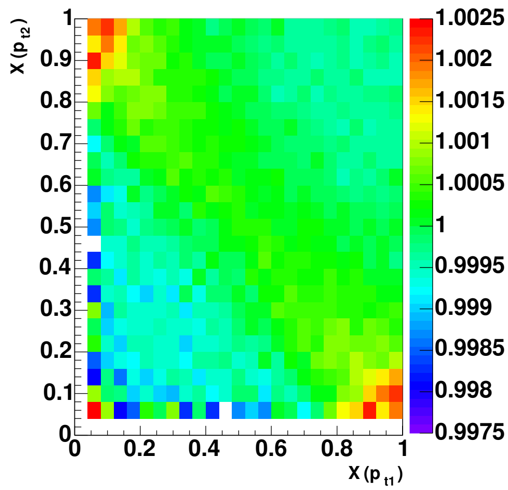

Figure 6.23: Resonance contribution on the CI transverse two-particle density ratio estimated by Monte Carlo simulation.

tios constructed from different mixed-pair selections of multiplicity difference and vertex position along the beam-axis difference. The black points in Fig. 5.8 indicates the selection used to construct mixed-pair distribution in this analysis and red points indicates the tighten selection. If the mixed-event selection used in this analysis is inferior to the tighten selection, the effect appears as the difference between two-particle density ratios with different selections.

In Fig. 6.24, two-particle density ratios obtained with different mixed-pair conditions on the multiplicity difference (upper panels) and vertex position difference (lower panels). In the left-hand panels, the transverse-momentum two-particle density ratios with the mixed-pair construction used in this study are shown and in the middle, the results with tighten condition are shown. The two-dimensional differences are shown in the right-hand panels. Small structure on the difference plots indicates that the conditions used in this analysis are sufficient. Uncertainty associated with this procedure are assigned to be 4.0×10^{-4} for $x(p_{t1}) \sim x(p_{t2}) > 0.9$ and negligible otherwise.

6.4.7 TPC Central Membrane Crossing

The STAR TPC is constructed with two cylinders of independent TPC separated in the center (z = 0 cm) by a high-voltage membrane (Sec. 2.4). The mis-reconstruction of track caused by crossing of the central membrane were studied and its contribution to the two-particle correlation spaces are estimated by comparing positive pseudorapidity two-particle density ratios from events with positive and negative collision positions along z-axis, because only negative collision z-position include effect of central membrane for positive η particles. The comparison is presented in Fig. 6.25 and uncertainty of 1.0×10^{-3} for $x_1, x_2 < 0.2$ and 0.5×10^{-3} for $x_1, x_2 > 0.9$ and 0.3×10^{-3} for elsewhere, are assigned, in which uncertainty associated with event vertex position variation along z-axis are also included.

6.4.8 Total Systematic Error

Total systematic error on the transverse two-particle correlation space is obtained by adding the preceding non-negligible errors of each bin quadratically. Other contributions such as from TPC hardware, momentum resolution,

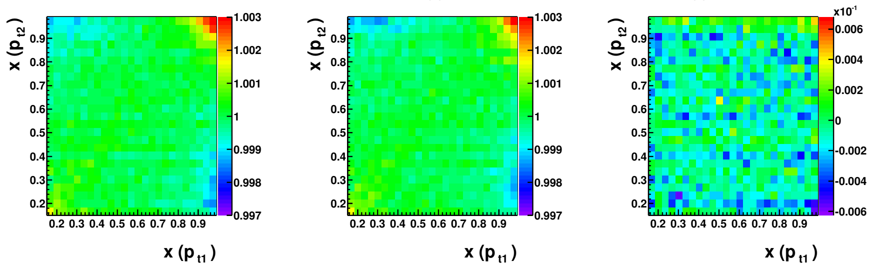

(i) Multiplicity difference 50 to 30 cm

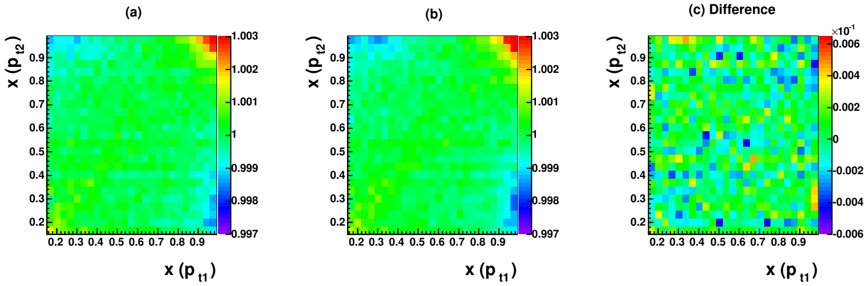

(ii) Vertex z-position difference 5 to 3 cm

Figure 6.24: Comparison between two-particle density ratio with different mixed-event constraints: (i) multiplicity difference, (ii) vertex z-position difference. Left-hand panels show the two-particle density ratio with the mixed-pair selection used in the data analysis and middle plots show with mixed-pairs constructed with the tighter conditions.

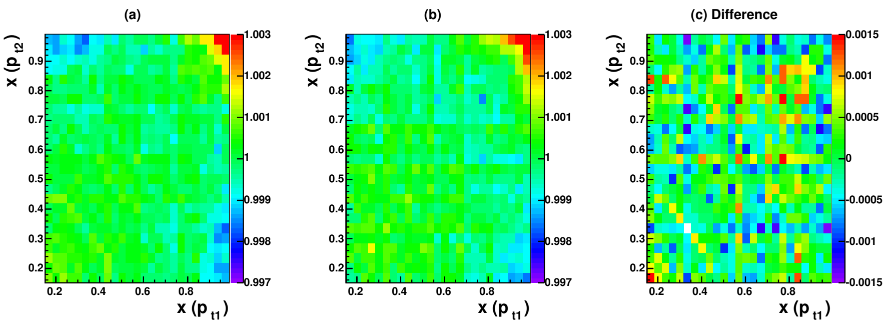

Figure 6.25: Comparison between the two-particle density ratios of the positive pseudorapidity acceptance (a) positive z-vertex position, (b) negative z-vertex position and (c) the difference. Only negative z-vertex position include effect from central membrane crossing of tracks.

time dependence of detector, azimuthal/psudorapidity dependence are considered separately and found to be negligible in this analysis. The final systematic error distribution is shown in 6.26 for central events and approximately the same systematic error to signal ratio are applicable for all centrality classes.

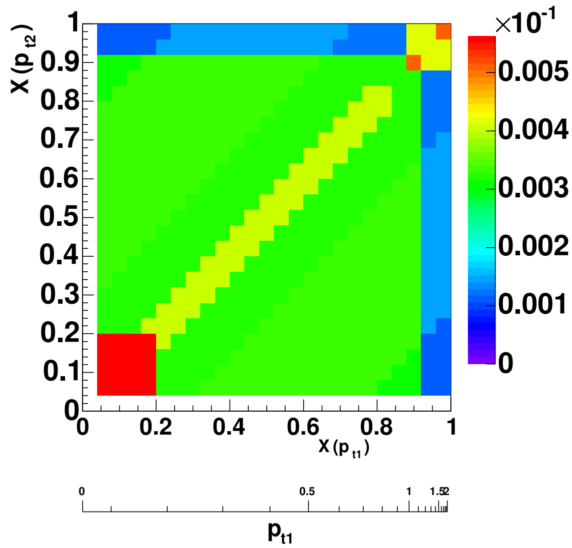

Figure 6.26: Total systematic error distributions in transverse two-particle momentum space. Approximately the same sigma to signal ratio apply for all centralities.

6.5 Summary

The transverse-momentum two-particle correlation structure through the two-particle number-density ratio analysis of Au-Au collisions are studied for the first time at RHIC energy of $\sqrt{s_{NN}} = 130$ GeV. We have observed the major correlation structures which is not anticipated by existing theoretical models, in the CI two-particle transverse momentum space; (1) the large-momentum-scale saddle-shaped structure and (2) the high-x_Σ, x_Δ independent components (3) small-momentum-scale correlations (the Bose-Einstein and Coulomb correlations). The last is eliminated by cuts and the first two are the main subjects of interest in this study.

The observation of saddle-shaped large-momentum scale correlation structure is qualitatively and quantitatively described by the model based on two-particle transverse-momentum distributions which are in turn represented by two-point temperature distributions (Sec. 4.1). The residual high-x_Σ component of correlation structure from the two-dimensional temperature model fit have approximate independence of x_Δ and its projection onto x_Σ diagonal are obtained. Projected residuals are fitted with the model function inspired by semi-hard scattering particle production in p-p collisions.

The overall correlation structure can be interpreted as the result of initial-state semi-hard parton scattering and subsequent fragmentation (mini-jet) in which partons are strongly modified by in-medium dissipation in the more central Au-Au collisions, leading to a complex temperature/velocity structure in the pre-hadronic medium which is reflected in the observed two-particle p_t correlations revealed by this work.

The scale dependence of those correlation structures are also observed, however for the study of the correlation-scale in axial momentum spaces, the more investigation of soft+hard correlation components with larger event sample statistics are desired for the future study. Also, the particle identification in the studied detector acceptance is anticipated to step into the local and global temperature fluctuation for the future study.

The charge dependent part of correlation structure exhibits the approximate independence of x_Δ direction and the one-dimensional projection onto x_Σ diagonal is constructed. Correlation structures in the CD transverse two-particle density ratios show a small centrality dependence in amplitude and a slight shape changes. These CI and CD two-particle correlation observations are consistent with the behaviors of event-by-event $< p_t >$ fluctuation analysis.

Chapter 7

Charge-Dependent Axial-Momentum Correlations

Measurements of charge-dependent (CD) two-particle axial momentum joint autocorrelations in Au-Au collisions at $\sqrt{s_{NN}}$ =130 GeV are presented in this chapter. Joint autocorrelations are formed for axial-momentum difference variables, pseudorapidity difference $\eta_\Delta \equiv \eta_1 - \eta_2$ and azimuth difference $\phi_\Delta \equiv \phi_1 - \phi_2$. Study of correlations and fluctuations has access to the dynamics in the early stages of heavy ion collisions and the color medium produced in the collisions. Specifically, in-medium modification of color-string fragmentation and hard partonic scattering in heavy ion collisions affect large-momentum-scale correlations. String fragmentation models account for axial (η, ϕ) correlations in high-energy p-p collisions in terms of local conservation of transverse momentum and net charge (Sec. 4.2) and thus produce CD correlations. Charge-dependent part of correlation structures are obtained by subtracting unlike-sign (US) joint autocorrelation from like-sign (LS). In this chapter, we consider charge-dependent or isovector aspects of correlations related to charge conservation at hadronization.

Events, tracks and pairs used in this analysis are selected according to

Sec. 5.1 - 5.3, and associated systematic uncertainties are considered following the result (Sec. 7.3). In this study, total of 340k events (217k central and 123k minimum-bias triggered event samples) are analyzed and divided into four centrality bins defined in Sec. 5.4 according to event multiplicities. The small-momentum-scale correlations in CD axial-momentum two-particle space are corrected as described in Sec. 5.7 unless noted.

7.1 Two-Particle Density Ratio

Like-sign (LS) and unlike-sign (US) two-particle density ratios of axial momentum $(\mathcal{S}\overline{\mathcal{N}}-1)(R(\eta_1,\eta_2)-1)$ and $(\mathcal{S}\overline{\mathcal{N}}-1)(R(\phi_1,\phi_2)-1)$ for four centrality classes without small-momentum-correlation correction are shown in Fig. 7.1. In pseudorapidity two-particle space, a dominant large-scale positive correlations for US pairs (Fig. 7.1 (i)) and a small correlation structures for LS pairs (Fig. 7.1 (ii)) besides small-momentum-scale correlation near $\eta_\Delta \sim 0$ diagonal are observed. Observed correlation structures resemble pseudorapidity correlations in p-p collisions and are suggestive of charge-ordering in color-string fragmentation. In azimuthal two-particle space, a quadrupole influential structure for both LS and US pairs often characterized by the second-harmonic coefficient v_2 arising from an anisotropy of initial collision geometry (Sec. 4.3) are observed. In addition to the v_2 component, the large-scale structure similar to that is observed in pseudorapidity space, a strong positive peak in the same-side (Fig. 7.1 (iii)) and small anti-correlation for the away-side pairs (Fig. 7.1 (iv)) are also found.

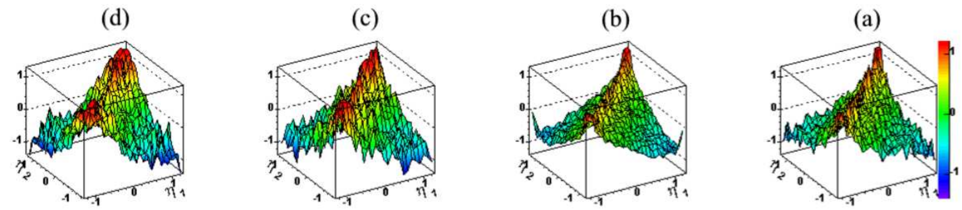

(i) US, $\eta \otimes \eta$

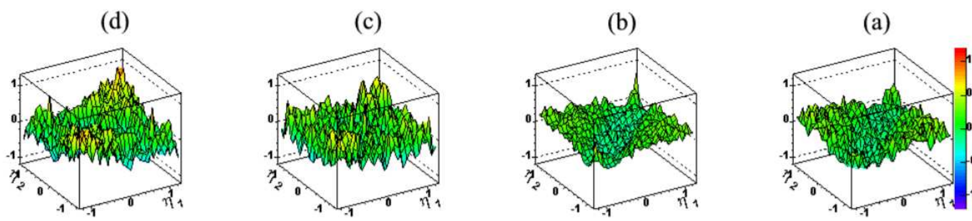

(ii) LS, $\eta \otimes \eta$

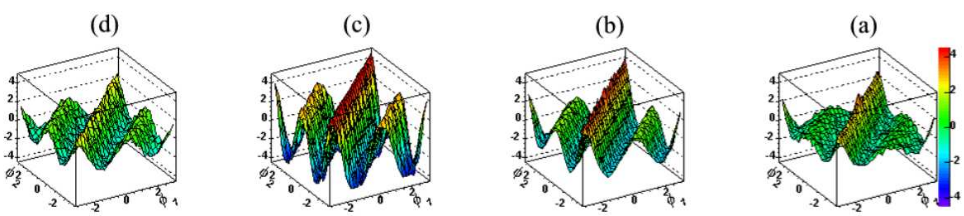

(iii) US, $\phi \otimes \phi$

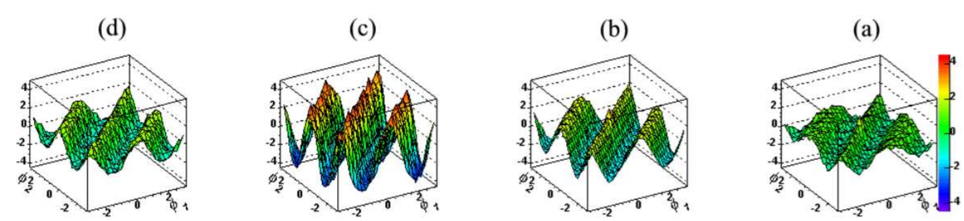

(iv) LS, $\phi \otimes \phi$

Figure 7.1: Perspective views of LS and US axial-momentum two-particle density ratios $(\mathcal{S}\overline{\mathcal{N}}-1)(R(\eta_1,\eta_2)-1)$ and $(\mathcal{S}\overline{\mathcal{N}}-1)(R(\phi_1,\phi_2)-1)$ in Au-Au collisions at $\sqrt{s_{NN}} = 130$ GeV for (a) most-central (b) mid-central (c) mid-peripheral and (d) peripheral centrality bins. Small-momentum-scale correlation correction is not applied.

7.2 Joint Autocorrelation

Motivated by an approximate independence of correlation structures of the axial-momentum sums $\phi_\Sigma \equiv \phi_1+\phi_2$ and $\eta_\Sigma \equiv \eta_1+\eta_2$, we obtain projections of two-particle density ratios onto the difference ($\phi_\Delta \equiv \phi_1 - \phi_2$, $\eta_\Delta \equiv \eta_1 - \eta_2$) diagonals to create one-dimensional autocorrelations (Sec. 3.2) without loss

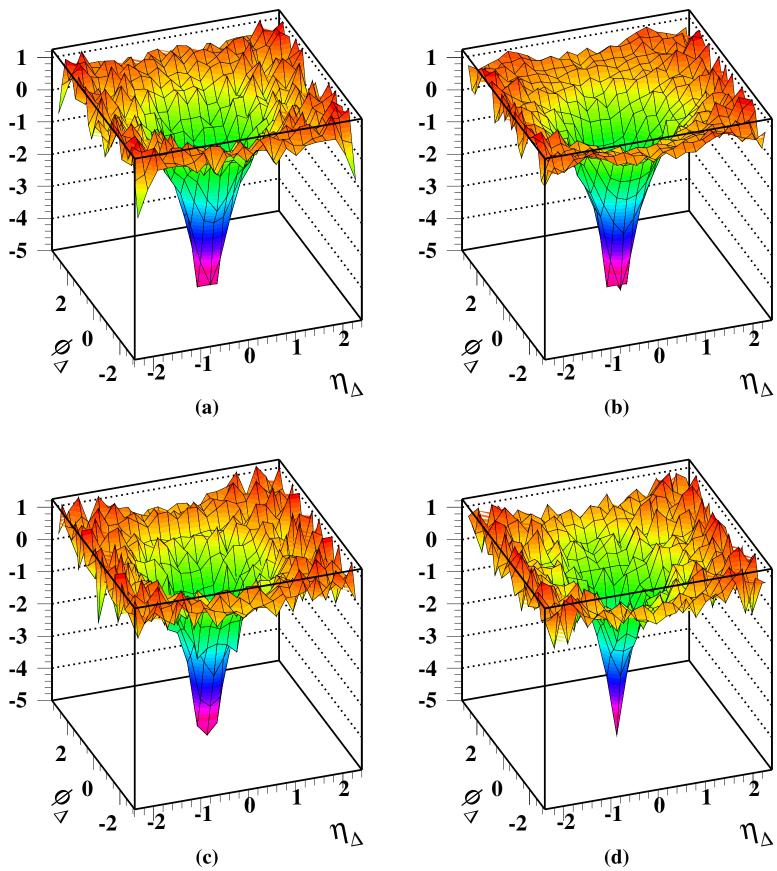

Figure 7.2: Normalized centrality dependence of CD axial-momentum joint autocorrelations $(\bar{\mathcal{S}}\bar{\mathcal{N}}-1)(R_{CD}(\eta_\Delta, \phi_\Delta)-1)$ in Au-Au collisions at $\sqrt{s_{NN}} = 130$ GeV for (a) most-central (b) mid-central (c) mid-peripheral and (d) peripheral centrality bins.

of information. Two-dimensional joint autocorrelations on difference-variable pair (η_Δ, ϕ_Δ) then compactly represent all correlation information on axial momentum space (η, ϕ). In Fig. 7.2, perspective views of charge dependent (CD = LS − US) joint autocorrelations of axial momentum variables $(\mathcal{S}\overline{\mathcal{N}}-1)(R(\eta_\Delta, \phi_\Delta)-1)$ for four centrality classes are presented.

A strong negative peaked structure of which amplitude and shape significantly change with collision centrality is observed. In both pseudorapidity and azimuth difference directions the correlation length change with centrality. Different centrality developments in each direction are clearly observed by contrasting one-dimensional η_Δ, ϕ_Δ autocorrelation projections obtained by taking average of joint autocorrelation over the other difference variables. Projections from different averaged ranges are plotted in Fig. 7.3. Projections from partial averages over $|\eta_\Delta| < 1.5$ onto ϕ_Δ-axis (black points) and η_Δ projections from region $|\phi_\Delta| < \pi/2$ (blue points) are shown in Fig. 7.3 (i), and full range average projection onto ϕ_Δ-axis ($|\eta_\Delta| < 2.6$) and onto η_Δ-axis ($|\phi_\Delta| < \pi$) are plotted in Fig. 7.3 (ii). The amplitude of two-dimensional central peaks are reduced in 1D projections by the averaging procedure. The major two-dimensional negative peak are broader and elliptical for peripheral collisions, transitioning smoothly to a narrower and deeper peak nearly symmetric on (η_Δ,ϕ_Δ) for central collisions.

Obtained two-dimensional CD joint autocorrelations shown in Fig. 7.2

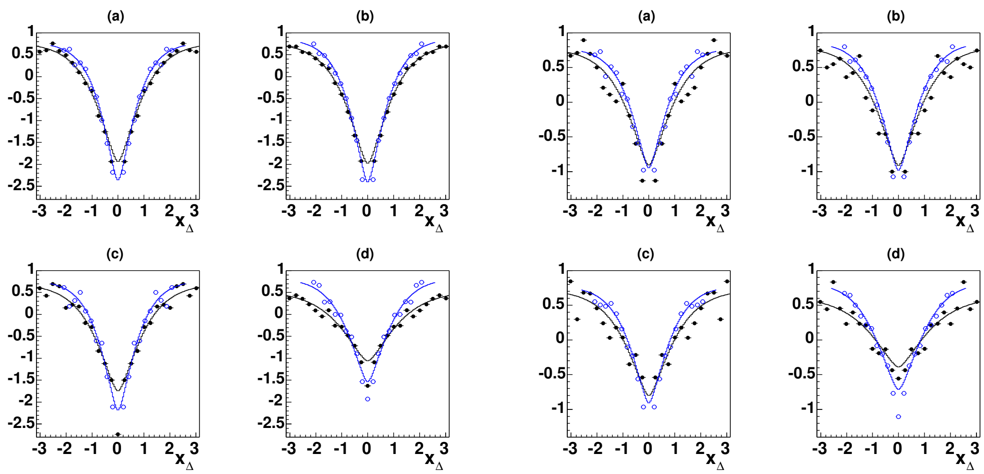

(i) Partial projection (ii) Full projection

Figure 7.3: Centrality dependence of one-dimensional projections of normalized CD axial momentum joint autocorrelations for (a) most-central (b) mid-central (c) mid-peripheral and (d) peripheral centrality bins. Projections are obtained by taking (i) partial and (ii) full averages. Blue points indicate the projection onto η_Δ axis and black points correspond to the ϕ_Δ projections.

are parameterized with a model function,

$$F(\eta_\Delta, \phi_\Delta) = \mathcal{A}_1 e^{\left[-\left(\frac{\eta_\Delta}{\sqrt{2}\sigma_{\eta_{\Delta,1}}}\right)^2 + \left(\frac{\phi_\Delta}{\sqrt{2}\sigma_{\phi_{\Delta,1}}}\right)^2\right]^{\frac{\mathcal{P}_1}{2}}} + \mathcal{A}_2 e^{\left[-\frac{1}{2}\left(\frac{\eta_\Delta}{\sigma_{\eta_{\Delta,2}}}\right)^2\right]^{\frac{\mathcal{P}_2}{2}}} + \mathcal{A}_0, \quad (7.1)$$

with 5 fit parameters and 3 fixed parameters of $\mathcal{P}_1$, $\mathcal{P}_2$ and $\sigma_{\eta_{\Delta,2}}$. The first term in Eq. 7.2 expresses the major central peak structure, the second term account for the correlation structures observed in p-p collisions which suggests an asymptotic behavior in very peripheral Au-Au collisions, and an offset. A single central bin ($|\eta_\Delta| \leq 0.1$, $|\phi_\Delta| \leq 0.1$) was excluded from model fit because of a contribution from contamination of $e^{\pm}$ pairs due to photon conversions.

Best-fit parameters and χ^2/DoF are given in Table 7.1. Obtained correlation model functions are shown in Fig. 7.4 and corresponding one-dimensional projections of the model functions are denoted by black and blue solid lines over ϕ_Δ and η_Δ projections respectively in Fig. 7.3.

centrality	(d)	(c)	(b)	(a)	fitting error(%)			
					(d)	(c)	(b)	(a)
$\overline{N}$	115.5	424.9	790.2	983.0	———			
$\mathcal{S}$	1.19	1.22	1.25	1.27	8% systematic error			
$(\mathcal{S}\overline{N}-1)\ \mathcal{A}_1$	-4.2	-6.8	-7.7	-7.7	6.0	4.9	2.5	3.8
$\sigma_{\eta_\Delta,1}$	0.46	0.42	0.41	0.41	9.6	6.4	3.2	4.8
$\sigma_{\phi_\Delta,1}$	0.66	0.54	0.51	0.51	11.3	7.1	3.4	5.2
$\mathcal{P}_1$	1	1	1	1	fixed			
$(\mathcal{S}\overline{N}-1)\ \mathcal{A}_2$	-0.51	-0.11	-0.15	-0.02	33.5	>100	61.5	>100
$\sigma_{\eta_\Delta,2}$	1.5	1.5	1.5	1.5	fixed			
$\mathcal{P}_2$	2	2	2	2	fixed			
$(\mathcal{S}\overline{N}-1)\ \mathcal{A}_0$	0.98	0.80	0.91	79	11.4	15.4	7.6	12.3
χ^2/DoF	$\frac{379.9}{315}$	$\frac{315.0}{315}$	$\frac{313.8}{315}$	$\frac{328.6}{315}$	———			

Table 7.1: Parameters and fitting errors for model fits to CD axial-momentum joint autocorrelations for (a) most-central (b) mid-central (c) mid-peripheral and (d) peripheral events.

The structures are compared with p-p axial momentum two-particle correlations. We observe that CD correlations for central Au-Au collisions differ markedly from p-p observations. Quantitative trends of 2D peak widths with centrality are shown in Fig. 7.5, along with p-p limiting cases. In p-p collisions, charge-ordering or local charge conservation of transverse momentum and net charge via color-string fragmentation along beam-axis (Sec. 4.2) were observed as two-particle (pseudo-)rapidity autocorrelations. In Au-Au

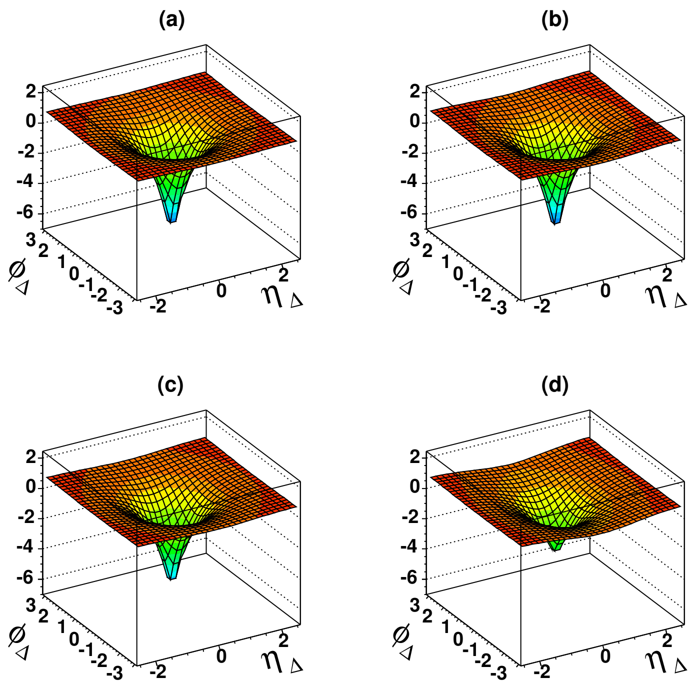

Figure 7.4: Centrality dependence of model functions from fits on the two-dimensional CD axial momentum joint autocorrelations for (a) most-central (b) mid-central (c) mid-peripheral and (d) peripheral centrality bins.

collisions, a large amplitude two-dimensional peak approximately exponential in form dominates the correlation structures, with similar widths on η_Δ and ϕ_Δ much reduced from p-p collisions. For the most-peripheral centrality class, we observe a change in the CD correlation structures suggesting an asymptotic trend toward p-p collisions as increased ϕ_Δ width and the emergence of a single gaussian peak on η_Δ.

We speculate that the phenomenon driving CD correlations in Au-Au collisions remains local-in-coordinate space charge ordering, but that the

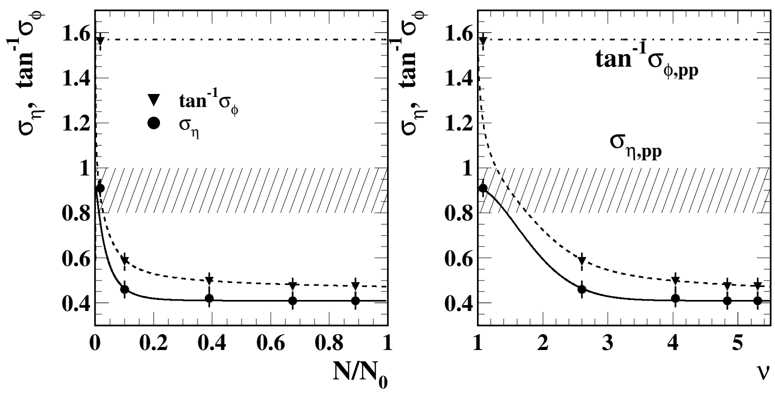

Figure 7.5: Centrality trends of parameters, fitted widths for 2D model peaks on η_Δ (σ_{η_Δ}) and on ϕ_Δ (σ_{ϕ_Δ}) to CD axial-momentum joint autocorrelations from Table 7.1 plotted on total multiplicity (left) and on estimated mean path length ν estimated by $(N_{part}/2)^{1/3}$, where N_{part} is the number of participant nucleons in an A-A collision according to the Glauber model. Hatched regions show p-p values. Curves guide the eye.

hadronization geometry changes from 1D to 2D with increasing A-A centrality and that a hadron-opaque medium forms in central Au-Au, or the string fragmentation in p-p collisions develops toward the fragmentation of the bulk medium in the central Au-Au collisions. Charge ordering becomes two-dimensional already for the peripheral class in the present centrality definition with $\nu = 2 - 3$. Because the CD correlations are detected only if both particles in the pair are not absorbed or scattered in the medium, the shape of correlation structures, close to the exponential in the central Au-Au collisions and having small and equal correlation lengths on η_Δ and ϕ_Δ, indicate the pair survival probability as function of pair angle differences or opening angle, thus expected to be dependent on the hadron mean free path.

7.3 Systematic Study

The uncertainty associated the two-particle axial momentum correlation constructions are considered in this section similar to that for transverse-momentum space (Sec. 6.4).

7.3.1 Reconstruction Effect

Axial-momentum variables of particles are reconstructed by tracking space-time positions of reconstructed hits obtained from ADC values measured by the STAR TPC. The effects arising from the tracking procedure are estimated by comparing two-particle ratios of simulated signals before and after detector response calculations.

In Fig. 7.6, the left-side panels (a) present joint autocorrelation from simulated events which passed through the detector response simulations and the offline tracking. The middle plots (b) show the results from input simulation data without the detector response simulation for CI (upper panels) and CD (lower panels) two-particle density ratios. In the simulated model, only CI correlation of an equal LS and US correlation is included. The absence of correlation structures in the difference distribution in the right-hand panels (c) obtained by subtracting two-dimensional distribution shown in the middle panel from the left-hand panel, indicate that the axial momentum variables are appropriately reconstructed and do not introduce the artificial effects on the axial two-particle momentum spaces. Also no observed CD correlation structures in the lower panels confirms that no pair-charge dependent offline-tracking effect are introduced. Bin content histograms of the difference distribution in the right-hand panels are shown at the bottom (iii, iv) of which variances agree within statistical error and the effect are considered to be negligible for current study.

The statistical error distributions in the CI and CD joint autocorrelation distributions based on pair entries are shown in Fig. 7.7. In each two-particle spaces, the statistical error is approximately constant along η_Σ, ϕ_Σ and ϕ_Δ directions but quadratically increase with $|\eta_\Delta|$. The standard errors on the CD and CI spaces differ by a factor of two except for a small difference variable region due to different small-momentum-scale correlation cut parameters (Sec. 5.7).

7.3.2 Charge Symmetry

The formation of CI and CD two-particle correlation space are based on the assumption of charge symmetry property of correlation structures. Deviation from the assumption are estimated by comparing two-particle density ratios from pairs with each charge combination of (+,+), (−,−) for LS and (+,−), (−,+) for US pairs.

In the right-hand panels of Fig. 7.8 (c), the difference between axial joint autocorrelations of each charge combination for LS (i) and US (ii) are shown. The absence of correlation structure on the difference distributions confirms that the assumption of charge symmetry properties of two-particle correlations are valid and the size of contents fluctuation indicate that the

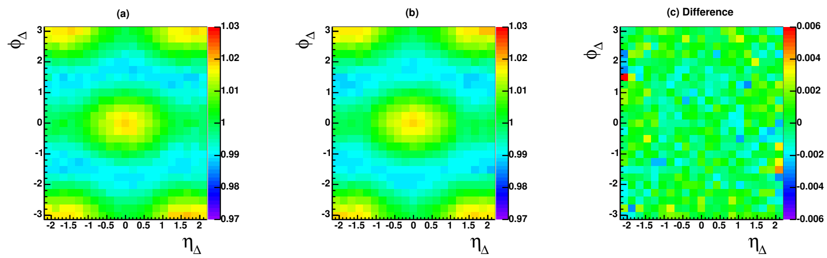

(i) CI

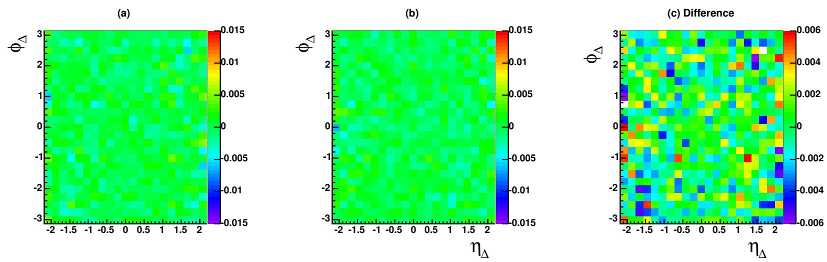

(ii) CD

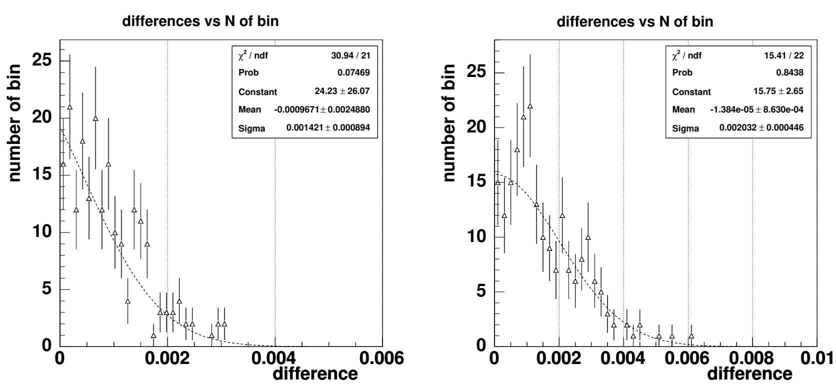

(iii) CI (iv) CD

Figure 7.6: Comparison of CI (i) and CD (ii)axial joint autocorrelations from 1000 simulated events before and after offline event reconstruction. (iii, iv) CI and CD bin-number distribution of bin contents differences fitted with gaussian function indicated by dashed line. The average of bin variances over region -1.56 $< \eta <$ 1.56 are $\sqrt{<\sigma^2_{CI}>} = 0.001$ and $\sqrt{<\sigma^2_{CD}>} = 0.002$.

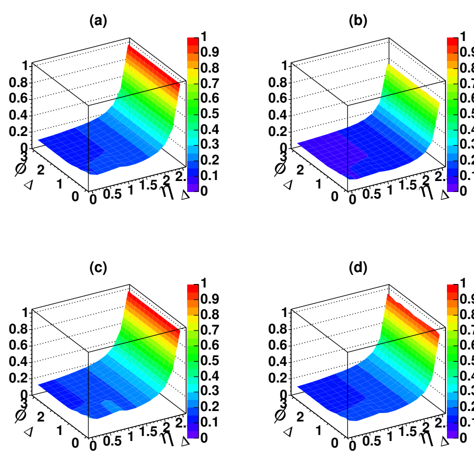

(i) CI

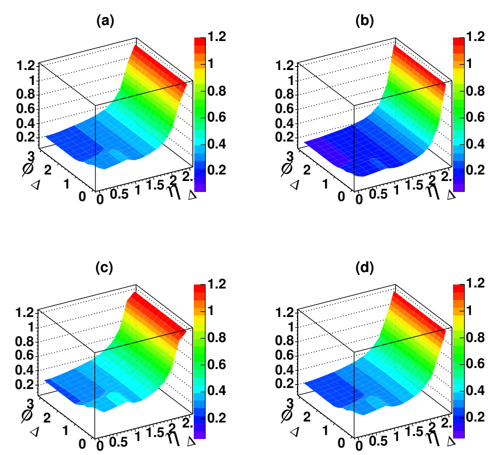

(ii) CD

Figure 7.7: Statistical error distributions for CI and CD axial joint autocorrelations for (a) most-central (b) mid-central (c) mid-peripheral and (d) peripheral centrality bins.

deviations are negligible for this study.

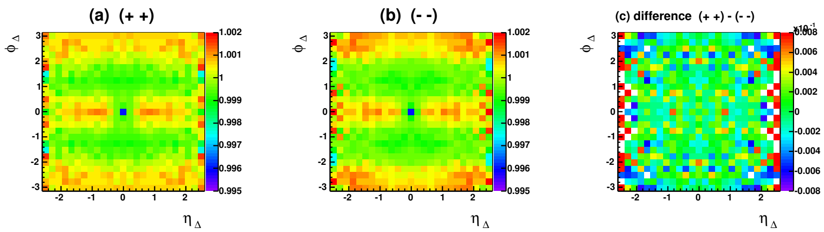

(i) LS

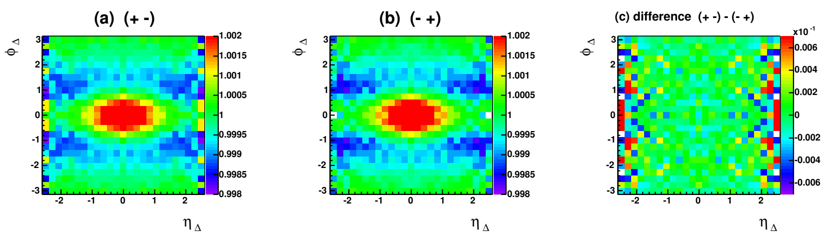

(ii) US

Figure 7.8: Axial-momentum joint autocorrelations of (i,a) $(+,+)$, (i,b) $(-,-)$, (ii,a) $(+,-)$ and (ii,b) $(-,+)$ pair-charge combinations. The distribution of bin content differences for each charge combinations (i,ii-c) are also presented.

7.3.3 Pair Inefficiency Effect

The pair-wise mis-reconstruction effects described in Sec. 5.3 appear also in the axial momentum spaces and are removed according to the pair geometrical separations within TPC volume. The uncertainty associated with the pair inefficiency corrections are considered in this section.

Because the axial momentum difference variables directly related to the closeness of reconstructed hit positions, the pair inefficiency results mainly in small difference axial momentum variables (η_Δ, ϕ_Δ) region. The upper panels shown in Fig. 7.9 is the results of MEVSIM Monte Carlo simulation [74]. The panels which represents CI, CD, LS and US two-particle spaces from left-hand to right-hand panels, display the two-particle axial momentum region in which pairs are reduced by pair-wise tracking inefficiency by larger than 1×10^{-4} as a white and red area. The magnitude of effect are shown for central and peripheral event classes in the lower panels. The region suffered by the pair-merging effect less than 1×10^{-4} are negligible. The simulation results show that pairs with $|\eta_\Delta| < 0.1$ (central 1 bin) and $|\phi_\Delta| < 0.7$ rad are subject of pair inefficiency for both CI and CD correlation study. Because the pair-merging occur only with similar tracking shape and thus mainly occur for LS with small ϕ_Δ, only the central bin of $|\eta_\Delta| < 0.08$ and $|\phi_\Delta| < 0.125$ rad are suffered by pair-merging effect and the other components are considered to be due to track-splitting effect.

The track-splitting effects appeared on two-particle axial momentum spaces in data are shown in Fig. 7.10 by comparing the azimuthal two-particle density ratio and axial joint autocorrelations from pair which include and exclude the crossing geometries. In the left-hand panels of Fig. 7.10, $\phi \otimes \phi$ two-particle density ratios of positive $p_{t,\Delta}$ for (i) (+,+) and (ii) (−,−) charge combination pairs are shown. With the positive transverse momentum difference, the crossing geometry is only formed for (+,+) pairs with negative ϕ_Δ

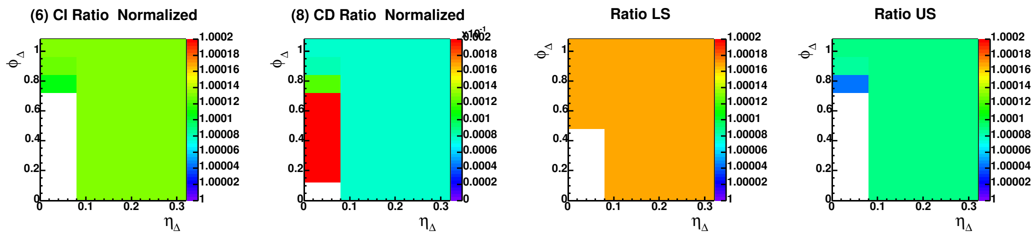

(i) Region

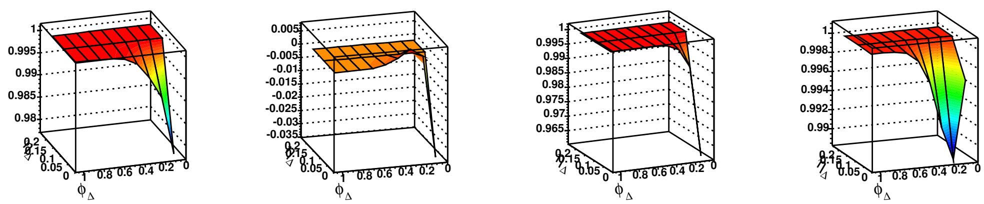

(ii) Magnitude, Central

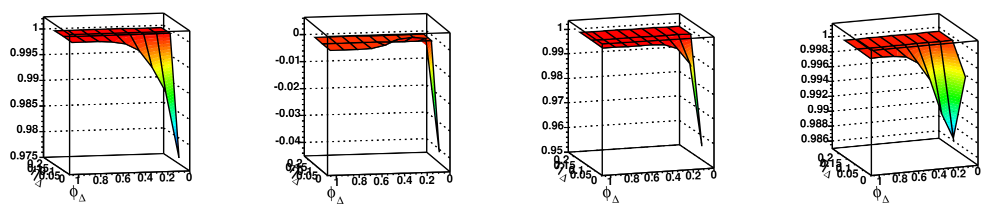

(iii) Magnitude, Peripheral

Figure 7.9: Contribution from pair-merging and track-splitting on axial-momentum joint autocorrelations estimated by Monte Carlo simulation. In the upper panel (i), possible pair inefficiency affected area are indicated by white and red region for CI, CD, LS and US from the left-hand to the right-hand panels, magnitude of the effect for central and peripheral events are shown in the lower panes of (ii) and (iii) respectively.

and (−,−) pairs with positive ϕ_Δ. Thus the upper half part above the main diagonal in the left-hand panel of (i) and the lower half part below the main diagonal in the left-hand panel of (ii), are the track-splitting candidate region.

The middle panels in the upper plots (i) and (ii) present the correlation structure distribution difference between positive and negative ϕ_Δ region. The difference plots are obtained by creating each correlation plots of left-hand panels of (i) and (ii) except these are symmetric about main diagonal and subtract the symmetrized correlation distribution from the original plots. Its one-dimensional projection onto ϕ_Δ axis are shown at the right-hand side.

Track-splitting effect are observed at just above and below the main diagonals for (+,+) and (−,−) respectively as blue bins next to the main diagonal line. The appearance of effect at the region of opposite ϕ_Δ signs are consistent with the expectation but only in the small azimuth difference region of $|\phi_\Delta| < 0.38$ rad.

The similar plots of the joint autocorrelations are shown in the bottom panels. The joint autocorrelations on the left-hand side of (iii) and (iv) show consistent results of the effect appeared on negative ϕ_Δ region for (+,+) pairs and positive ϕ_Δ for (−,−) pairs as a white bin at the center and blue bin below and above the central bin respectively. The different plots shown in the right-hand panels are obtained by subtracting the reflected joint autocorrelation of the right-hand panels about $\phi_\Delta = 0$ from the original joint autocorrelation plots, the white lines along $\phi_\Delta = 0$ indicate zero difference values by construction.

The pair-wise cut described in Sec. 5.3 based on pair separation at mid-TPC radius remove the crossing candidate pairs in both sibling- and mixed-pairs. The same plots after splitting cut are presented in Fig. 7.11. Absence of the structural difference between negative and positive ϕ_Δ region in the difference plots shown in the middle panels in (i, ii) confirms that the geometry dependent effect are removed by the cut. It is also consistent with the observation that the white and blue bin appeared at the center and the next to center on the joint autocorrelation before the track-splitting cut (left-hand panels of Fig. 7.10 (iii, iv)) are disappeared on the same plots after the cut (left-hand panels of Fig. 7.11 (iii, iv)). The central red bin appeared on the joint autocorrelation after the track-splitting cut shown in the left-hand panels of Fig. 7.11 (iii, iv) are due to the contribution from small-momentum-scale correlations and also from electron background contaminations.

The pair-merging effect removed by anti-merging cut of average separations are shown in Fig. 7.12. Upper 4 plots of each set for (i) CD, (ii) LS and (iii) US pairs present the joint autocorrelation with different average pair separation parameters of 0 (no merging cut), 5, 10 (used in this analysis) and 15 cm from left to the right.

Each of lower 3 plots displays the difference between joint autocorrelations with different anti-merging average separation parameters to see the effect of increased cut parameters, and is obtained by subtracting bin-by-bin contents of joint autocorrelations with the larger merging cut parameter from joint autocorrelation with the next smaller cut parameter.

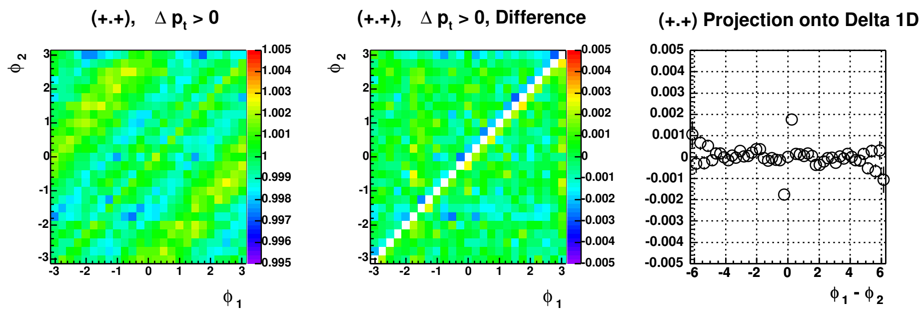

(i) positive-positive (+.+) pair charges

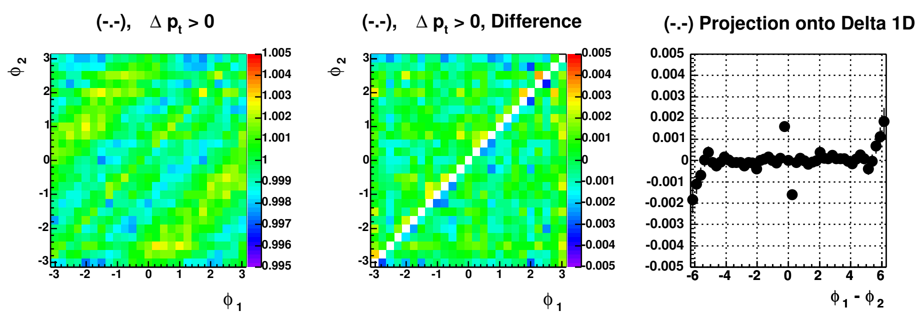

(ii) negative-negative (−.−) pair charges

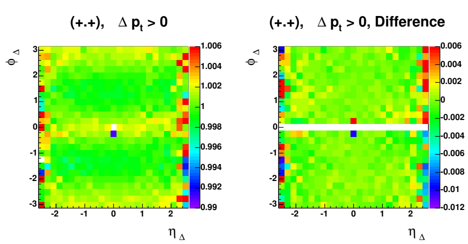

(iii) positive-positive (+.+) pair charges

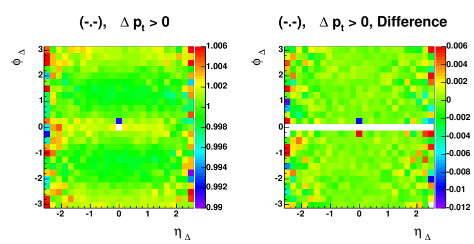

(iv) negative-negative (−.−) pair charges

Figure 7.10: Axial two-particle distributions and joint autocorrelations of (i, iii) $(+,+)$ and (ii, iv) $(-,-)$ pair-charge combinations with positive $p_{t,\Delta}$. The difference between the region of different ϕ_Δ signs indicate the effect from track crossing before the pair-wise track-splitting cut.

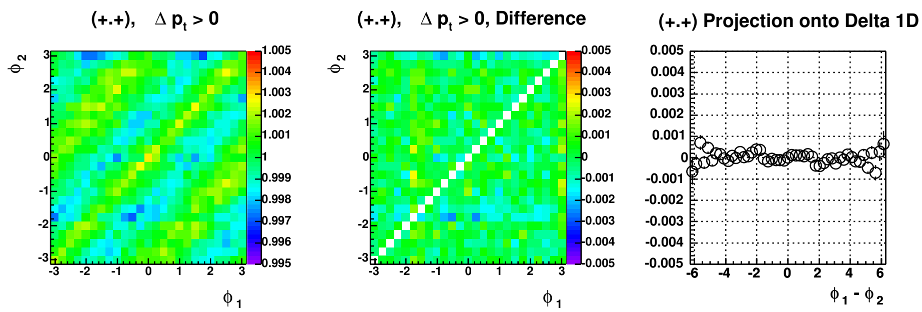

(i) positive-positive (+.+) pair charges

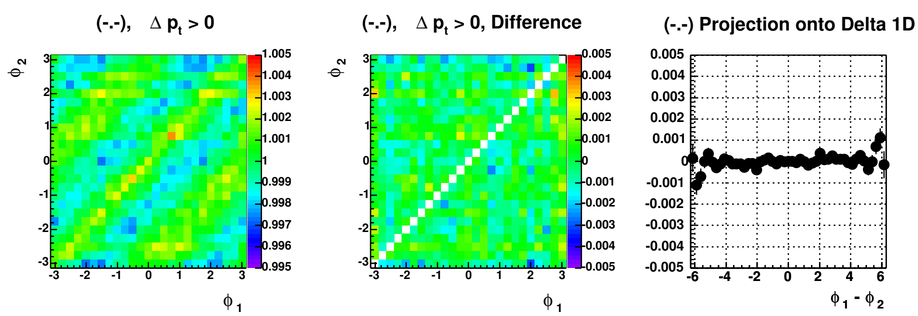

(ii) negative-negative (−.−) pair charges

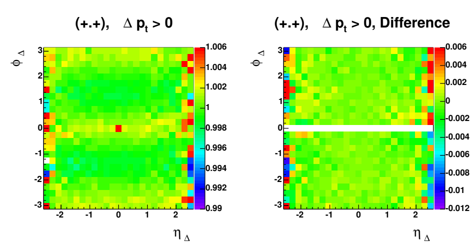

(iii) positive-positive (+.+) pair charges

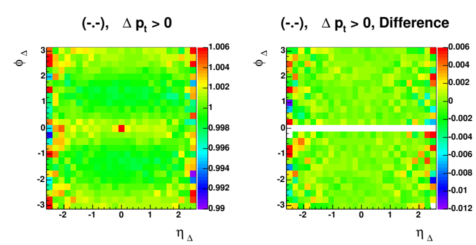

(iv) negative-negative (−.−) pair charges

Figure 7.11: Two-particle axial momentum distributions and joint autocorrelations for (i, iii) $(+,+)$ and (ii, iv) $(-,-)$ pair-charge combinations with positive $p_{t,\Delta}$, after track-crossing separation cut of $d_t^{mid} > 30$ cm and $d_z^{mid} > 10$ cm for accepted pairs which have crossing geometries.

The removal of merged pairs are seen in the lower left panels of Fig. 7.12 (ii) for LS pairs by observing blue colored bin on the center and are not seen for US pairs as expected by that LS pairs with similar shapes is more likely to suffered from pair-merging effect. We observe the effect appears only on central 1 bin in the joint autocorrelation space and with increased cut parameter the small-momentum-scale BE correlation surpass the merging effect. Thus the anti-merging average separation of 10 cm used in the actual analysis is considered to be sufficient to remove the pair-merging effect without sacrificing a large number of good pairs.

Excepting the central bin of $|\eta_\Delta| < 0.104$, $|\phi_\Delta| < 0.126$ rad where excluded from fit mainly because of large background electron contaminations, the total uncertainty associated with the pair inefficiency correction are assigned a quarter of estimated effect by Monte Carlo simulation. For CI, the systematic uncertainty associated with track-splitting and pair-merging correction corresponds to 2.5×10^{-3} for $|\eta_\Delta| < 0.1$ and $0.1 < |\phi_\Delta| < 0.3$ rad. For CD 1.0×10^{-3} for $|\eta_\Delta| < 0.1$ and $0.3 < |\phi_\Delta| < 0.7$ rad and 1.0×10^{-3} over $|\eta_\Delta| < 0.1$ and $|\phi_\Delta| < 0.7$ rad. The systematic errors are negligible elsewhere.

7.3.4 Small-Momentum-Scale Correlation Correction

Appearance of the Bose-Einstein and Coulomb small-momentum-scale correlations on the two-particle axial momentum space are presented in Fig. 7.13. The effects are estimated by Monte Carlo simulation [74] for CI, CD, LS and US pairs from left-hand to the right-hand panes for the central (i) and periph-

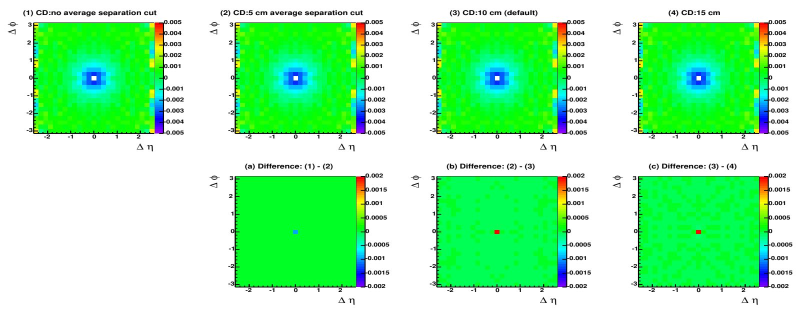

(i) CD

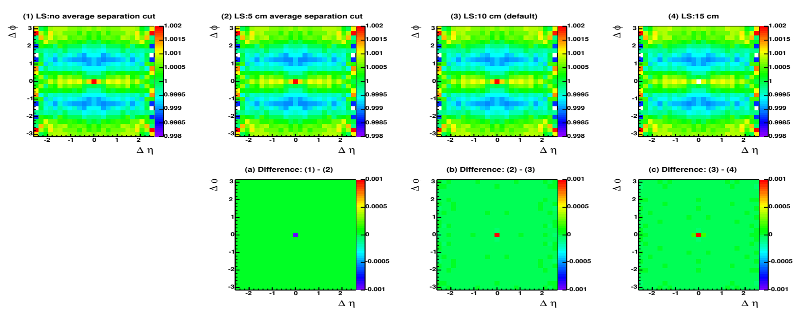

(ii) LS

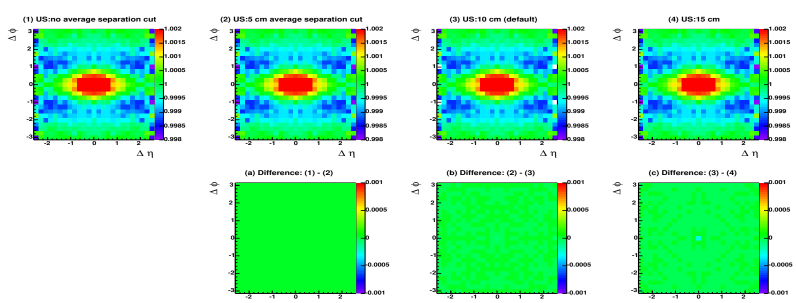

(iii) US

Figure 7.12: Effect of merging-cut appeared on axial momentum joint autocorrelations for (i) CD, (ii) LS and (iii) US pairs. Upper plots present joint autocorrelations with different merging-cut parameters, from left to the right merging-pair cut parameters are increased from 0 cm to 15 cm with 5 cm interval. Lower plots display the effects of close track pair removal as a function of increasing cut parameters.

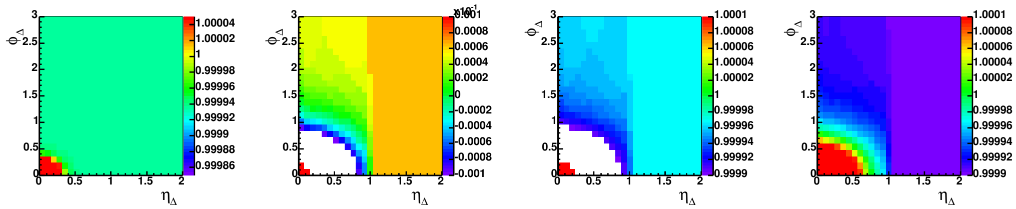

(i) central for CI, CD, LS and US pairs from left

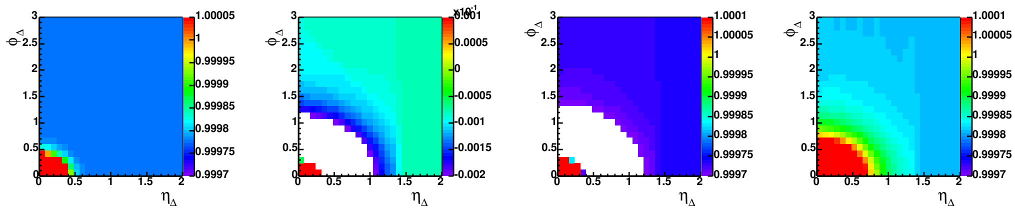

(ii) peripheral for CI, CD, LS and US pairs from left

Figure 7.13: Effect of the Bose-Einstein and Coulomb small-momentum-scale correlation on axial joint autocorrelations estimated by Monte Carlo simulation. Effects are shown for (i) central and (ii) peripheral events, from left-hand to right-hand panes for CI, CD, LS and US pairs.

eral (ii) events. The red region appeared on small momentum difference region ($\eta_\Delta \sim 0$ and $\phi_\Delta \sim 0$) for all plots are due to the Bose-Einstein correlation and the surrounding negative structure for CD and LS pairs and positive correlation for US pair plot correspond to the Coulomb correlations. The region suffered from the small-momentum-scale correlations in the two-particle axial momentum spaces are, for CI, $|\phi_\Delta| < 0.5$ rad and $|\eta_\Delta| < 0.5$, and for CD, about $|\phi_\Delta| < 1.0$ rad and $|\eta_\Delta| < 1.0$, considering only the range in which the correlation exceed $\sim 1 \times 10^{-4}$. The difference in the small-momentum-scale

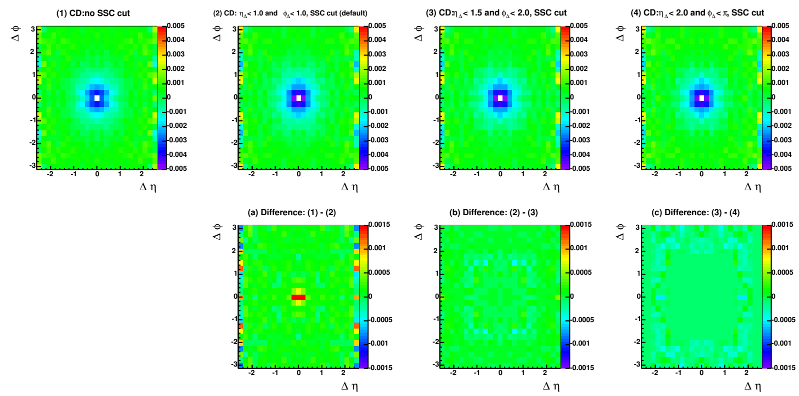

Figure 7.14: Effect of increased small-momentum-scale correlation cut parameters appeared on axial joint autocorrelations for CD pairs. Upper plots present the axial joint autocorrelations with different small-momentum-scale correlation correction parameters of η_Δ and ϕ_Δ, from left-hand to right-hand panels the cut parameters are increased from no cut, short-momentum-scale correlation cut are applied for $|\eta_\Delta| < 1.0$ and $|\phi_\Delta| < 1.0$ (used in this analysis), for $|\eta_\Delta| < 1.5$ and $|\phi_\Delta| < 2.0$ and for $|\eta_\Delta| < 2.0$ and $|\phi_\Delta| < \pi$. Lower plots are 2D difference histograms displaying the effect of short-momentum-scale correlation removal as a function of increasing cut parameters.

correlation for CI and CD comes from the Coulomb interaction.

In Fig. 7.14, the dependence on the small-momentum-scale correlation cut parameters of η_Δ, ϕ_Δ are presented for CD pairs. The upper panels show the CD joint autocorrelations with different small-momentum-scale correlation cut parameters of η_Δ and ϕ_Δ. From left-hand to right-hand panels the cut parameters are increased from no cut, short-momentum-scale correlation cut applied for $|\eta_\Delta| < 1.0$ and $|\phi_\Delta| < 1.0$, for $|\eta_\Delta| < 1.5$ and $|\phi_\Delta| < 2.0$ and for $|\eta_\Delta| < 2.0$ and $|\phi_\Delta| < \pi$. Lower panels present the effect due to the cut parameter increase. Small structure observed on the lower two right-hand panels is consistent with the choice of small-momentum-scale correlation cut for the axial momentum range $|\eta_\Delta| < 1.0$ and $|\phi_\Delta| < 1.0$.

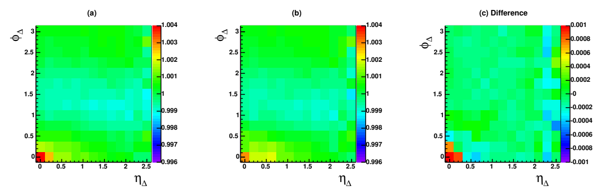

(i) CI

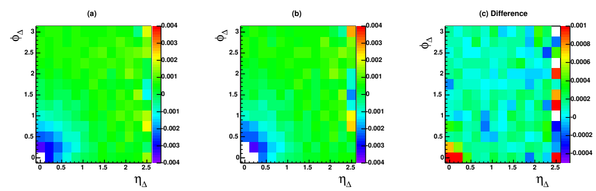

(ii) CD

Figure 7.15: Axial joint autocorrelations (a) before and (b) after the small-momentum-scale correlation cut for CI (i) and CD (ii). The difference are presented in (c) and indicate that the small-momentum-scale correlation cut does not affect the large-scale correlation structures.

In Fig. 7.15, the joint autocorrelation structures before (left-hand panels) and after (middle panels) the small-momentum-scale correlation cut are compared for (i) CI and (ii) CD. The difference between correlation structures before and after the small-momentum-scale correlation correction are shown in the right-hand panels. Note that small-momentum-scale correlation cut parameters are different for CI and CD (Sec. 5.7). The plots confirm that the small-momentum-scale correlation cut does not affect the large-scale correlation structures appeared for both CI and CD correlation spaces. Because of the track-splitting and pair-merging cuts, large part of small-momentum-scale correlations are expected to be already removed.

The uncertainty associated with the small-momentum-scale correlation removal (not associated with the short-momentum-scale correlation in the data itself) are assigned to be a quarter of expected correlation amplitude estimated by Monte Carlo simulation shown in Fig 7.13, *i.e.* for CI, 2×10^{-4}, over $|\phi_\Delta| <$ 0.5 rad and $|\eta_\Delta| < 0.5$ and negligible other area, and for CD, 2×10^{-4}, over $|\phi_\Delta| < 1.0$ rad and $|\eta_\Delta| < 1.0$, 2.0×10^{-5} over $|\phi_\Delta| > 1.0$ rad and $|\eta_\Delta| < 1.3$ and negligible elsewhere.

7.3.5 Background Contributions

The contribution from non-primary background particles to the two-particle axial momentum correlations are considered following the discussion given for the transverse momentum correlations (Sec. 6.4.5) The e^+e^- pairs from photon conversion emerge at very small opening angles of less than 1°) [80] and these are partially removed by pair-merging cuts of average pair separation and the small-momentum-scale correlation correction of pair p_t differences. We avoid the effect from the electron background from photon conversion by excluding the central single bin of axial joint autocorrelations defined by $|\eta_\Delta| < 0.1$ and $|\phi_\Delta| < 0.1$ from model fits. The knock-out protons from the beam pipe and other detector material could contribute to two-particle correlation for $(+,+)$ charged-pair but not $(-,-)$ pairs. Thus the negligible difference between LS two-particle correlation of different charges (Sec. 7.3.2) indicate

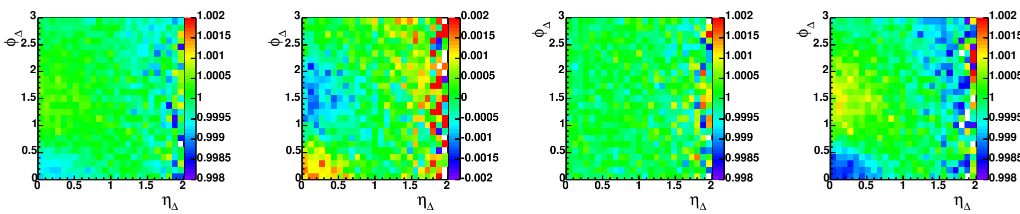

Figure 7.16: Resonance contribution on the axial joint autocorrelations estimated by Monte Carlo simulation, from left-hand to right-hand panels, for CI, CD, LS and US pairs.

that the proton knock-out contamination is negligible in this study. Thus the main contribution from background non-primary particles (Sec. 6.4.5) to the study of two-particle axial-momentum correlations are the hadronic secondary decay products.

Because the parent primary and daughter, and two daughters correlation in the axial momentum space is unknown, the contribution from hadronic background in the axial momentum space is calculated for two extreme cases of 100% correlation, *i.e.* the daughters are in the same direction as the parent, and 0% correlation, *i.e.* the directions of daughters are independent of parent directions. Following the similar consideration as in Sec. 6.4.5 for the uncertainty associated with unknown parent-daughter correlation in the hadronic background, the uncertainty in the two-particle axial momentum space is assigned to be $\sim 7\%$ for the dilution correction.

The contribution from resonance decays (ρ^0, ω, η) are estimated by Monte Carlo simulation [82] and presented in Fig. 7.16. It is estimated that the effect exists in US pairs as the negative correlation for $|\phi_\Delta| < 0.5$ rad,

$|\eta_\Delta| < 0.7$ and a small positive correlation near $|\phi_\Delta| \sim \pi/2$ with $|\eta_\Delta| < 0.5$. It appears as the opposite sign effect in CD and the same sign effect in CI two-particle spaces.

7.3.6 Mixed-Event Selections

The mixed-pair reference distributions are constructed from the pairs taken from different events of close properties as described in Sec. 5.5. Construction of mixed-pairs from events of insufficient close properties leads undesirable effects [70]. Appropriateness of the mixed-event selections are tested by comparing joint autocorrelations constructed from different mixed-pair selections of multiplicity difference and vertex position along beam-axis difference.

In Fig. 7.17, the CD (i, ii) and CI (iii, iv) axial joint autocorrelation formed with different selections of mixed-pair construction are presented. The results with the mixed-pair distributions used in this study (left-hand panels) and with the tighten selection (middle panels) and the two-dimensional difference are presented in the right-hand panels. The different selections are shown as black and red points in Fig. 5.8. Small structure on the difference plots confirms that the conditions used in this analysis are sufficient and effects from mixed-pair distributions are negligible.

7.3.7 Total Systematic Error

Total systematic error on the axial two-particle correlation space is obtained by adding the preceding non-negligible errors of each bin quadratically.

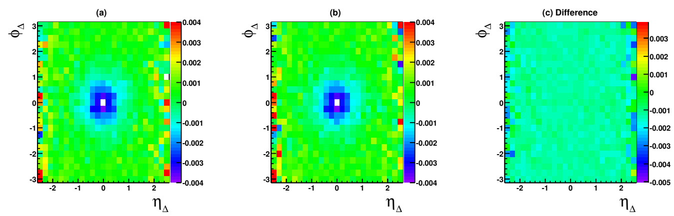

(i) CD:Multiplicity difference 50 to 30 cm

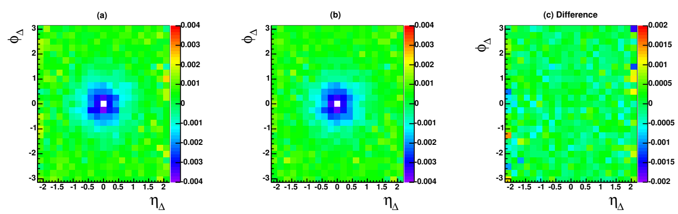

(ii) CD:Vertex z-position difference 5 to 3 cm

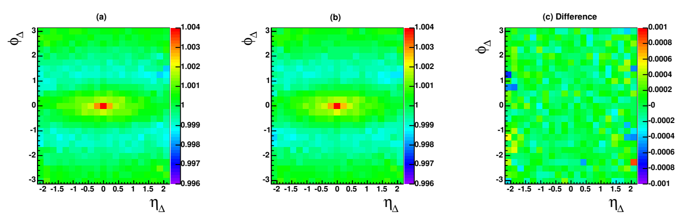

(iii) CI:Multiplicity difference 50 to 30 cm

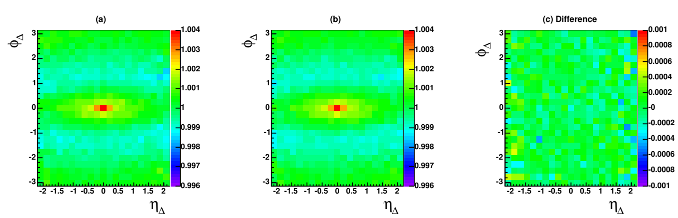

(iv) CI:Vertex z-position difference 5 to 3 cm

Figure 7.17: Comparison between axial joint autocorrelations with different mixed-event constraints for CD and CI: (i, iii) multiplicity difference, (ii, iv) vertex z-position difference. Left-hand panels show the axial joint autocorrelation with the mixed-pair selection used in the data analysis and middle plots show with mixed-pairs constructed with the tighter conditions.

Other contributions from TPC, z-vertex location dependence, momentum resolution, time dependence of detector, azimuthal/psudorapidity dependence are considered separately and found to be negligible in this analysis. The main systematic uncertainty source on the axial momentum space are the 7% uncertainty associated with the signal dilution from unknown hadronic background correlations in the data.

The final systematic error distribution is shown in Fig. 7.18 for central events and approximately the same systematic error to signal ratio are applicable for all centrality classes.

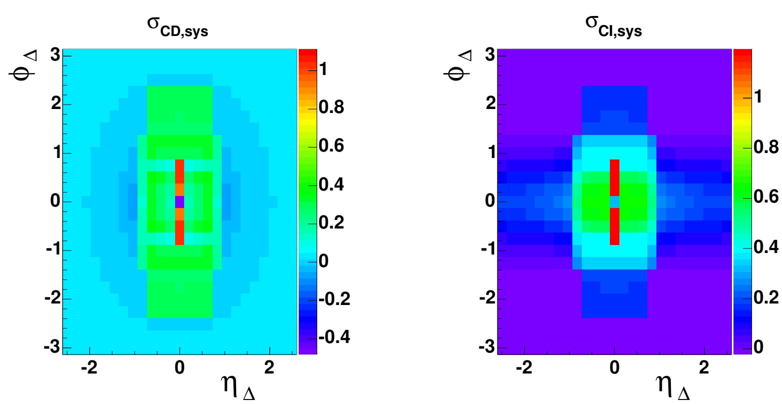

(i) CD

(ii) CI

Figure 7.18: Total systematic error distributions in axial joint autocorrelations for (i) CD and (ii) CI central events. Main contribution is 7% uncertainty associated with hadronic background correlations. Approximately the same sigma to signal ratio apply for all centralities.

7.4 Summary

The first measurement of charge-dependent (CD) joint autocorrelations on difference variables η_Δ and ϕ_Δ for Au-Au collisions at $\sqrt{s_{NN}} = 130$ GeV are presented. We observed a strong CD correlation over the large momentum difference scale comparable to TPC acceptance and its development with collision centrality.

The structure are dominated by a two-dimensional negative peak. The peak is broader and elliptical for peripheral collisions, and narrower nearly symmetric peak on η_Δ and ϕ_Δ is observed for central collisions. The centrality dependence of the strong peak exhibits a large amplitude increase, significant width reduction and transition to approximately equal width on η_Δ and ϕ_Δ direction. The CD correlation for the peripheral Au-Au events, increased ϕ_Δ width and the emergence of a single gaussian peak on η_Δ, suggests an asymptotic trend toward p-p collisions.

The CD correlation structures in Au-Au collisions are consistent with local charge conservation or canonical suppression of net charge fluctuations. However the significant centrality dependence suggests that the charge-ordering geometry is evolving from 1D color-string fragmentation observed in p-p collisions to exponentially attenuated 2D charge-ordered emission from a hadron-opaque medium formed in central Au-Au collisions. Charge-dependent autocorrelations provide unique access to the evolution of the hadron production geometry from spatially expanding bulk medium produced in the heavy ion collisions.

Chapter 8

Charge-Independent Axial-Momentum Correlations

Large-momentum-scale correlations in heavy ion collisions could result from initial-state multiple scattering of a combination of the Cronin effect [83] and minijet production [66], and fragmentation of color medium to final state hadrons (Sec. 4.2). Study of in-medium modifications or propagations of these correlation structures by two-particle number-density ratios should lead to improved understanding of color confinement and nonperturbative QCD dynamics. Charge-independent (CI) axial-momentum joint autocorrelations of unidentified charged hadrons in Au-Au collisions at $\sqrt{s_{NN}}$ =130 GeV described in this chapter sensitively measure the correlation developments in heavy ion collisions. An axial-momentum joint autocorrelations is constructed as a function of pseudorapidity difference $\eta_\Delta \equiv \eta_1 - \eta_2$ and azimuth difference $\phi_\Delta \equiv \phi_1 - \phi_2$. This form is consistent with the invariance property of two-particle correlation structures on pair-momentum sums as explicitly observed in each two-particle density ratios of (η_1, η_2) and (ϕ_1, ϕ_2) shown in Fig 7.1. Two different trigger settings of 217k central and 123k minimum-bias event samples are used in this analysis and divided into four centrality classes defined in Sec. 5.4. The small-momentum-scale correlations are corrected according to Sec. 5.7 unless noted. Data selection criteria are described in Sec. 5.1 - 5.3 and systematic errors are estimated in Sec. 7.3.

8.1 Joint Autocorrelation

Charge-independent (CI) two-particle joint autocorrelations of axial momentum variables $(\mathcal{S}\overline{\mathcal{N}}-1)(R_{CI}(\eta_\Delta, \phi_\Delta)-1)$ for four centrality classes are

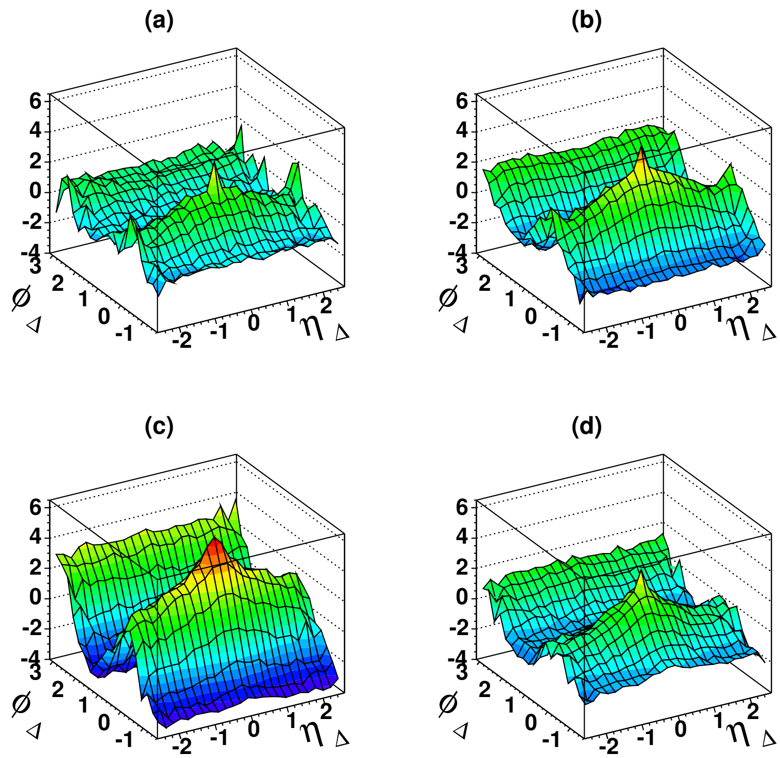

Figure 8.1: Perspective views of CI axial-momentum joint autocorrelations $(\mathcal{S}\overline{\mathcal{N}}-1)(R_{CI}(\eta_\Delta, \phi_\Delta)-1)$ in Au-Au collisions at $\sqrt{s_{NN}} = 130$ GeV for (a) most-central (b) mid-central (c) mid-peripheral and (d) peripheral centrality bins.

presented in Fig. 8.1. We observe the strong correlation structures and their significant centrality developments. The large-momentum-scale structure are dominated by a quadrupole component on ϕ_Δ and a strong peak dependent both on ϕ_Δ and η_Δ mainly at same-side azimuth difference ($\phi_\Delta \leq \pi/2$) region. The former is a correlation due to initial anisotropy of collision geometry of which centrality dependence are well studied [57–59] and the latter is the main object of present study.

In order to isolate the same-side correlation peak, away-side components are parameterized by the first 3 terms of Fourier series as,

$$F_v(\phi_\Delta) = A_{v_1} cos(\phi_\Delta) + A_{v_2} cos(2\phi_\Delta) + A'_2, \tag{8.1}$$

similar to Eq. 4.20. Parameters are obtained such that the residual structures over the range $|\phi_\Delta| < 1.2$ rad and $|\eta_\Delta| \leq 2.18$ become minimum and same-side residual structure exhibits smooth ϕ_Δ dependence. Shown in Fig. 8.2 the obtained parameterized functions for away-side anisotropic components are subtracted from data in Fig. 8.1. The isolated same-side positive peak amplitude in Fig 8.2 shows non-monotonic behavior with centrality and the peak shape is strongly broadened along η_Δ in the most-central class. A small excess in the single central bin defined by $|\eta_\Delta| < 0.1$ and $|\phi_\Delta| < 0.1$ corresponds to background electron pairs due to photon conversion (Sec. 7.3.5).

Apparent difference in the development of correlation structure along different axis, a large width increase along η_Δ and reduction in ϕ_Δ and non-monotonic amplitude variations with centrality are observed in the one-dimensional

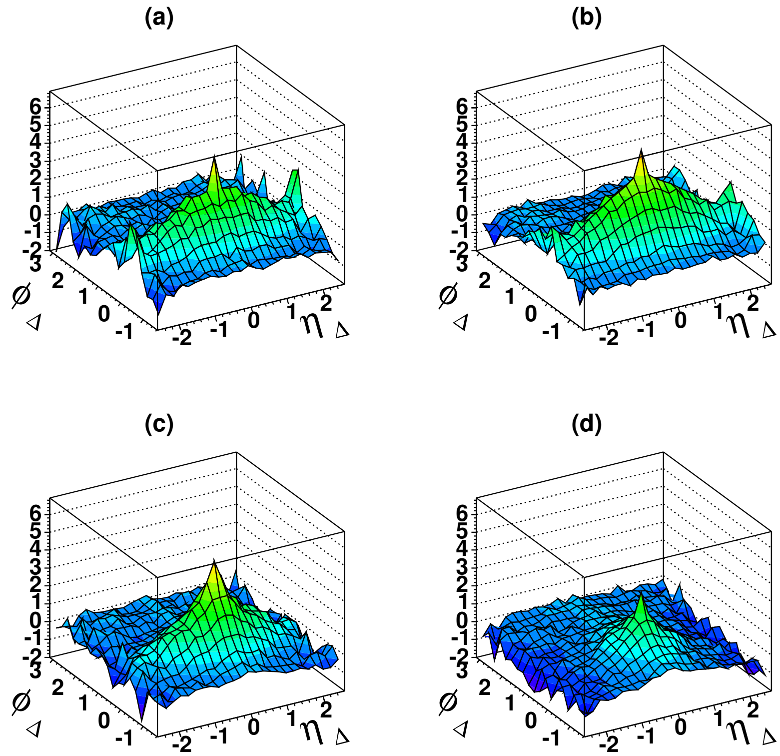

Figure 8.2: Same data as in Fig. 8.1 but η_Δ-independent the first and second harmonic components have been subtracted for (a) most-central (b) mid-central (c) mid-peripheral and (d) peripheral centrality bins.

projections of the joint autocorrelation onto each difference-variable axis (η_Δ and ϕ_Δ) separately and are shown in Fig. 8.3. The projections are obtained by taking average of correlation structure on the joint autocorrelation over the other difference variables. Two-dimensional peak amplitudes are reduced in the one-dimensional projections by the averaging process. Projections from the similar averaged region for η_Δ and ϕ_Δ, over $|\eta_\Delta| < 1.5$ onto ϕ_Δ-axis (black points) and η_Δ projections from region $|\phi_\Delta| < \pi/2$ (blue points) are shown in upper panels of Fig. 7.3 (i), and full range average projection onto ϕ_Δ-axis ($|\eta_\Delta| < 2.18$) and onto η_Δ-axis ($|\phi_\Delta| < \pi$) are plotted in lower panels of Fig. 7.3 (ii).

Two-dimensional CI joint autocorrelations after away-side v_1 and v_2 component subtraction in Fig. 8.2 are fitted with a model function which includes a two-dimensional gaussian of η_Δ and ϕ_Δ, and a one-dimensional gaussian function of η_Δ with a constant ϕ_Δ dependence, written by,

$$F_{CI}(\eta_\Delta, \phi_\Delta) = \mathcal{A}_1 e^{-\left[\left(\frac{\eta_\Delta}{\sqrt{2}\sigma_{\eta_{\Delta,1}}}\right)^2 + \left(\frac{\phi_\Delta}{\sqrt{2}\sigma_{\phi_{\Delta,1}}}\right)^2\right]} + \mathcal{A}_0 e^{-\frac{1}{2}\left(\frac{\eta_\Delta}{\sigma_{\eta_{\Delta,0}}}\right)^2} + \mathcal{A}_2. \quad (8.2)$$

Best-fit parameters and χ^2/DoF from the fit over $|\phi_\Delta| \leq \pi$ and $|\eta_\Delta| \leq 2.18$ are presented in Table 8.1 together with A_{v1}, A_{v_2} and A_0' from the away-side v_1, v_2 parameterizations. The two-dimensional model functions are shown in Fig. 8.4 and its projections are denoted over the one-dimensional projections as solid lines in Fig. 8.3. The central bin which include a contribution from background electron is excluded from the model fit.

The structures are compared with the CI axial momentum two-particle correlations from p-p collisions. Quantitative trends of 2D peak widths with centrality are shown in Fig. 8.5, along with p-p limiting cases. Same-side correlations for the peripheral centrality class are similar to the p-p result with comparable widths on η_Δ and ϕ_Δ. The same-side peak of p-p correlation structure results from mini-jet parton fragmentation process and similar correlation structure in Au-Au peripheral suggest that the close mini-jet productions in

centrality	(d)	(c)	(b)	(a)	fitting error(%)			
					(d)	(c)	(b)	(a)
$\overline{N}$	115.5	424.9	790.2	983.0	———			
$\mathcal{S}$	1.19	1.22	1.25	1.27	8% systematic error			
same-side peak (fit range: $0 \leq \phi_\Delta \leq \pi/2$)								
$(\mathcal{S}\overline{N}-1)\ \mathcal{A}_1$	1.93	3.23	3.72	3.1	4.5	2.2	1.1	2.3
$\sigma_{\eta_\Delta,1}$	0.57	1.05	1.34	1.36	4.6	3.1	1.8	3.6
$\sigma_{\phi_\Delta,1}$	0.61	0.55	0.54	0.53	4.0	2.0	1.8	3.7
$(\mathcal{S}\overline{N}-1)\mathcal{A}_0$	0.60	0.32	—	—	26.8	23.7	—	—
$\sigma_{\eta_\Delta,0}$	1.11	0.24	—	—	28.4	22.4	—	—
$(\mathcal{S}\overline{N}-1)\mathcal{A}'_2$	-0.46	-0.08	-0.07	-0.06	38.7	24.4	>100	>100
χ^2/DoF	$\frac{438.8}{315}$	$\frac{419.4}{315}$	$\frac{675.1}{315}$	$\frac{415.0}{315}$	———			
away-side structure (fit range: $1.2 \leq \phi_\Delta \leq \pi$)								
$(\mathcal{S}\overline{N}-1)\mathcal{A}_{v1}$	-0.31	-0.76	-0.97	-0.74	21.8	9.2	5.3	11.9
$(\mathcal{S}\overline{N}-1)\mathcal{A}_{v2}$	1.05	2.72	1.30	0.32	3.9	1.7	2.5	16.9
$(\mathcal{S}\overline{N}-1)\mathcal{A}_2$	-0.21	-0.46	-0.60	-0.51	19.0	8.3	5.1	10.2
χ^2/DoF	$\frac{282.2}{186}$	$\frac{265.8}{186}$	$\frac{436.2}{186}$	$\frac{273.9}{186}$	———			

Table 8.1: Parameters and fitting errors for model fits to CI axial-momentum joint autocorrelations for (a) most-central (b) mid-central (c) mid-peripheral and (d) peripheral centrality bins.

the soft-momentum region is contributed in peripheral events. In central collisions, the structure is still dominated by a 2D gaussian peak but widths on the two difference variables differ by a factor 3, with different centrality development feature of the peak structure in each direction, a factor of 2.5 increase in η_Δ width and about 10% decrease in ϕ_Δ width. The large modification of the correlation structure in the central collisions may result from strong coupling of minimum-bias partons to an axially-expanding color medium, and subsequential fragmentation to the hadrons.

Observation of large correlation peak in the central collisions is consistent with the picture that the fragmentation of parton is largely contributing the particle production of low-p_t region (p_t <2.0 GeV/c) and the structure modification suggests a strong coupling of the partons to a dissipative medium and its asymmetric in development η_Δ and ϕ_Δ with the collision centrality.

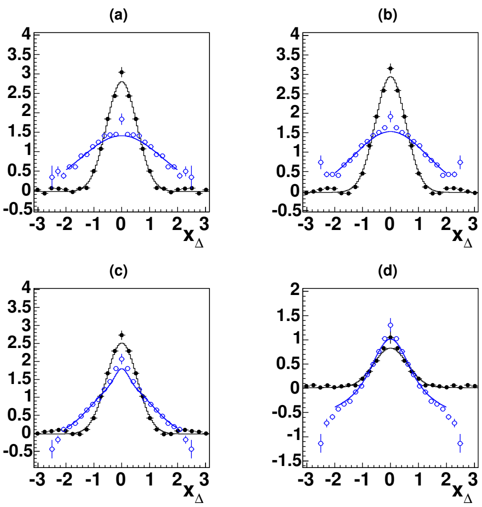

(i) Partial projection

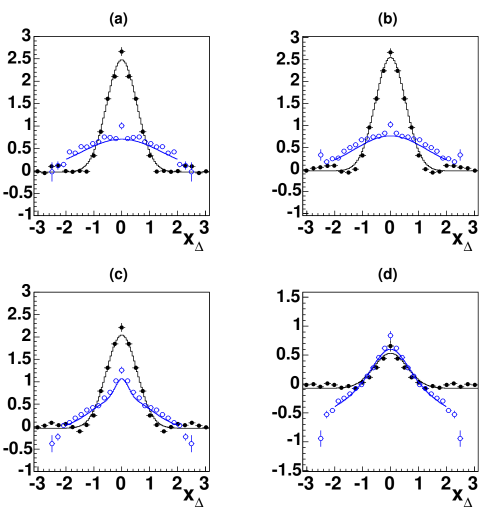

(ii) Full projection

Figure 8.3: One-dimensional projections of CI axial momentum joint autocorrelations after away-side components have been subtracted for (a) most-central (b) mid-central (c) mid-peripheral and (d) peripheral centrality bins. Projections are obtained by taking (i) partial ($|\eta_\Delta| < 1.5$,$|\phi_\Delta| < \pi/2$) and (ii) full ($|\eta_\Delta| < 2.18$,$|\phi_\Delta| < \pi$) averages. Solid lines represent the model fit functions. Blue and black points indicate the projection onto η_Δ axis and ϕ_Δ axis respectively.

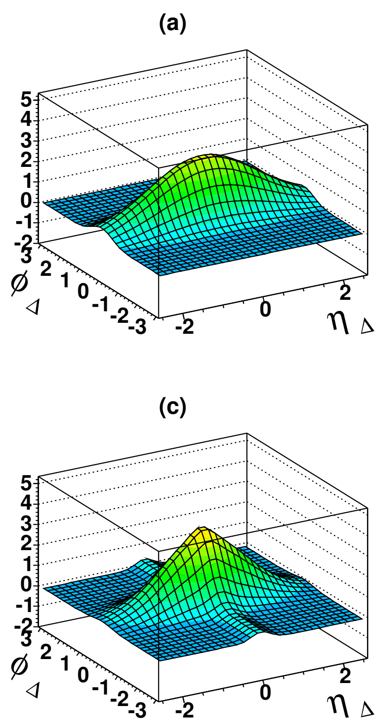

Figure 8.4: Centrality dependence of model functions fitted on the CI axial momentum joint autocorrelations after away-side subtraction for (a) most-central (b) mid-central (c) mid-peripheral and (d) peripheral centrality bins.

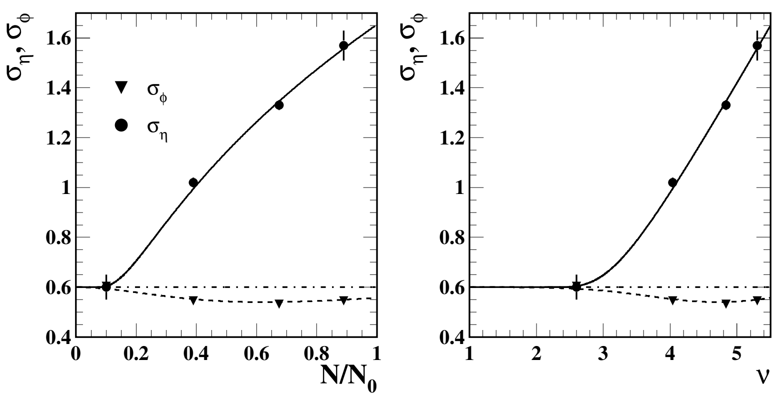

Figure 8.5: Centrality trends of parameters, fitted widths for 2D model peaks on η_Δ ($\sigma_{\eta_\Delta,1}$) and on ϕ_Δ ($\sigma_{\phi_\Delta,1}$) to CI axial-momentum joint autocorrelations from Table 8.1 plotted on total multiplicity (left) and on estimated mean path length ν estimated by $(N_{part}/2)^{1/3}$, where N_{part} is the number of participant nucleons in an A-A collision according to the Glauber model. Hatched regions show p-p values. Curves guide the eye.

8.2 Summary

We presented the first results of charge-independent (CI) joint number autocorrelation analysis on difference variables η_Δ and ϕ_Δ for Au-Au collisions at $\sqrt{s_{NN}} = 130$ GeV.

In the CI axial momentum joint autocorrelations, an one-dimensional quadrupole components on ϕ_Δ due to initial collision anisotropy and global momentum conservation is observed. In addition to the azimuthal structure, a significant same-side two-dimensional peak structure is observed. The peak structure is described by two-dimensional gaussian function and its amplitude and shape exhibit significant centrality dependence.

We observed a symmetric shape on η_Δ and ϕ_Δ in peripheral events and its highly asymmetric development in η_Δ and ϕ_Δ directions with collision centrality. The symmetric structure in η_Δ and ϕ_Δ in peripheral collisions is interpreted as hard-parton fragmentation similar to observed in p-p collisions. The trend of shape change with centrality, a large elongation of correlation structure in η_Δ direction while a small width reduction in ϕ_Δ with centrality, is consistent with the modification of parton fragmentation due to a strong coupling of the partons with color medium which is dissipative and axially expanding.

Chapter 9

Conclusion

I presented in this dissertation the first measurements of surviving correlation structures among unidentified charged hadron distributions produced in collisions of gold nuclei at $\sqrt{s_{NN}} = 130$ GeV measured by the STAR detector at RHIC. An abundant correlation structures over a large momentum scale comparable to the STAR TPC acceptance is observed in transverse momentum p_t range $0.15 \leq p_t \leq 2.0$ GeV/c, pseudorapidity range $-1.3 \leq \eta \leq 1.3$, and full azimuth angle acceptance $-\pi \leq \phi \leq \pi$. Pair-charge dependent (CD) and independent (CI) part of correlation structures are measured by means of two-particle number density ratios in transverse and axial two-particle momentum spaces.

In the CI two-particle transverse momentum number density ratios of transformed-p_t variable ($x(p_t)$), we find significant large-momentum-scale saddle shaped structures composed of a concave upward and downward along sum- and difference-axis respectively. The structures ($x(p_{t1})+x(p_{t2}) \leq 1.6$) are qualitatively and quantitatively described by a two-dimensional Lévy distribution inspired by the temperature fluctuation model. The residual structure at large x-sum exhibits an approximate independence of difference-axis, and is described by a gaussian model function of the transverse rapidity consistent with the hard scattering particle distribution in p-p collisions. The observed correlation structures are consistent with a scenario in which the particles originated from initial-state hard parton scattering and their associated fragmentation to hadrons (mini-jet) are modified by in-medium dissipation in the more central Au-Au collisions. These dynamics lead to a complex temperature/velocity structure in the pre-hadronic medium and the complex structure is reflected in the observed final-state two-particle p_t correlations revealed by this work.

In two-particle axial momentum joint autocorrelations, we observed large-momentum scale CD negatively peaked structure and CI correlations associated with elliptic flow and positively peaked structure corresponding to mini-jets. Both CD and CI correlations show the significant shape and amplitude change with increasing collision centrality.

The CD correlation in the two-particle axial momentum space observed in p-p collisions are phenomenologically described by the color-string fragmentation model in terms of local conservation of transverse momentum and net charge. The correlation structures observed in Au-Au collisions are compared with p-p axial momentum correlations, and we observe the CD correlation corresponding to the string fragmentation model to be markedly different in detail. In central Au-Au collisions, a large amplitude two-dimensional peak, approximately exponential in form, dominates the correlation structures with similar width on η_Δ and ϕ_Δ much reduced from p-p collisions. The centrality dependence of the correlation toward the most-peripheral centrality class suggests an asymptotic trend toward p-p collisions as increased ϕ_Δ width and the emergence of a single gaussian peak on η_Δ. The CD correlation observation is consistent with evolution of hadron emission geometry with increasing centrality from one-dimensional fragmentation of color strings to the two-dimensional bulk hadronization emitted from an opaque color medium.

The CI axial momentum two-particle correlation structures are dominated by a quadrupole component on ϕ_Δ and a strong positive peak at same-side azimuth difference dependent both on ϕ_Δ and η_Δ. The latter structure is extensively studied in this analysis. We observed a strong centrality development of the same-side correlation structures. In peripheral events, the structure exhibits a two-dimensional gaussian peak similar to observed in p-p collisions associated with minijet production with comparable width on η_Δ and ϕ_Δ. In central collisions the structure is still dominated by a 2D gaussian peak but widths on the two difference variables (ϕ_Δ and η_Δ) differ by a factor 3. These resulted from a quite different centrality development of the correlation along ϕ_Δ and η_Δ axis. This observation is consistent with the picture that the fragmentation of partons (minijet production) is the main contributor to particle production in the low-p_t region and the structure modification with centrality suggests a strong coupling of partons to a longitudinally-expanding color dissipative medium formed in Au-Au collisions.

We find that all correlation structures appeared on the different momentum spaces, and that the pair charge-combinations are consistent with a picture that parton and color-string fragmentation processes are largely contributing in the particle production in $p_t < 2.0$ GeV/c and that these processes are strongly coupled to a opaque or dissipative medium created in the relativistic heavy ion collisions. The medium has characteristic properties in the response to the impetus correlations. The centrality development of the correlation structures thus leads to detailed understanding of the development of the medium and heavy ion dynamics.

We confirmed by this study that the two-particle correlation structures produced in relativistic heavy ion collisions contain significant information about the color medium produced in collisions. Specifically, in-medium modification of color-string fragmentation and hard partonic scattering in heavy ion collisions are reflected in the large-momentum-scale correlation structures. This highly motivates future studies of correlation structures in heavy ion collisions, such as high-statistic correlation analysis for studies of finer centralities and acceptance dependencies and more specific correlation studies by particle identifications. Such studies should help to distinguish the particle velocity fluctuations from temperature fluctuations and lead to a further understanding about medium developments and its response. These analysis will provide critical information for understanding of color deconfined matter and descriptions of non-perturbative QCD.

Bibliography

[1] F.J. Ynduráin. *Quantum Chromodynamics.* Springer-Verlag, 1983.

[2] F. Abe et al. Measurement of the inclusive jet cross section in $\overline{p}$-p collisions at $\sqrt{s}$=1.8 TeV. *Phys. Rev. Lett.*, 62:613, 1989.

[3] M. Schmelling. Status of the strong coupling constant. *Proceedings of the XXVIII International Conference on High Energy Physics*, 1996. hep-ex/9701002.

[4] A. Chodos et al. *Phys. Rev. D*, 9:3471, 1974.

[5] G.E. Brown and M. Rho. *Phys. Lett.*, 82B:177, 1979.

[6] J.C. Collins and M.J. Perry. Superdense matter: Neutrons or asymptotically free quarks? *Phys. Rev. Lett.*, 34:1353, 1975.

[7] G. Chapline and L. Susskind. Lattice models of quark confinement at high temperature. *Phys. Rev. D*, 20:2610, 1979.

[8] T. Blum et al. beta function and equation of state for QCD with two flavors of quarks. *Phys. Rev. D*, 51:5153, 1995.

[9] F. Karsch. Lattice QCD at finite temperature and density. hep-lat/9909006, hep-lat/0106019.

[10] J.E. Elias et al. Experimental study of multiparticle production in hadron-nucleus interactions at high energy. *Phys. Rev. D*, 22:13, 1980.

[11] J.D. Bjorken. Highly relativistic nucleus-nucleus collisions: The central rapidity region. *Phys. Rev. D*, 27:140, 1983.

[12] S. Brodsky D. Sivers and R. Blankenbecler. Large transverse momentum processes. *Physics Reports*, 23C:1, 1976.

[13] S.J. Brodsky D.W. Sivers and R. Blankenbecler. Relativistic interactions between nuclei. *Phys. Rev. D*, 15:3321–3331, 1977.

[14] J.W. Harris B. Muller. The search for the Quark-Gluon Plasma. *Ann. Rev. Nucl. Part. Sci.*, 46:71–107, 1996.

[15] H. Heiselberg. Event-by-event physics in relativistic heavy ion collisions. *Physics Reports*, 315 (3):161–194, 2001. nucl-th/0003046.

[16] M. Rybczynski R. Korus, St. Mrowczynski and Z. Wlodarczyk. Transverse momentum fluctuations due to temperature variation in high-energy nuclear collisions. *Phys. Rev. C*, 64:054908, 2001. nucl-th/0106041.

[17] G. Baym and H. Heiselberg. Event-by-event fluctuations in ultrarelativistic heavy ion collisions. *Phys. Lett.*, B469:7–11, 1999. nucl-th/9905022.

[18] G. Wilk O.V. Utyuzh and Z. Wlodarczyk. The effects of nonextensive statistics on fluctuations investigated in event-by-event analysis of data. *Journal of Physics*, G26:39–44, 2000. hep-ph/9906500.

[19] L. Stodolsky. Temperature fluctuations in multiparticle production. *Phys. Rev. Lett.*, 75:1044, 1995.

[20] C.S. Lam. Entropy content of multiplicity distributions. *Phys. Lett.*, B217:530–534, 1989.

[21] A. Bialas and W. Czyz. Event by event analysis and enropy of multiparticle system. *Phys. Rev. D*, 61:074021, 2000.

[22] S. Mrowczynski. Hadronic matter compressibility from event-by-event analysis of heavy-ion collisions. *Phys. Lett.*, B430:9–14, 1998. nucl-th/9712030.

[23] S. Jeon and V. Koch. Charged particle ratio fluctuation as a signal for quark-gluon plasma. *Phys. Rev. Lett.*, 85:2076, 2000. hep-ph/0003168.

[24] U. Heinz M. Asakawa and B. Muller. Fluctuation probes of quark deconfinement. *Phys. Rev. Lett.*, 85:2072, 2000. hep-ph/0003169.

[25] L. Stodolsky. Temperature fluctuations in multiparticle production. *Phys. Rev. D*, 33:1304, 1986.

[26] K. Rajagopal M. Stephanov and E. Shurak. Event-by-event fluctuation in heavy ion collisions and the QCD critical point. *Phys. Rev. D*, 60:114028, 1999. hep-ph/9903292.

[27] H. Foelsche et al. *The Relativistic Heavy Ion Collider, RHIC.* World Scientific Publishing Co., 1993.

[28] A. Braem et al. Identification of high $p_\perp$ particles with the STAR-RICH detector. *Nucl. Instrum. Meth.*, A499:720, 2003.

[29] R. Bellwied et al. The STAR sillicon vertex tracker: A large area silicon drift detector. *Nucl. Instrum. Meth.*, A499:640, 2003.

[30] F. Bergsmaet al. The STAR detector magnet subsystem. *Nucl. Instrum. Meth.*, A499:633, 2003.

[31] M. Anderson et al. The STAR Time Projection Chamber: A unique tool for studying high multiplicity events at RHIC. *Nucl. Instrum. Meth.*, A499:659, 2003.

[32] M. Anderson et al. A readout system for the STAR Time Projection Chamber. *Nucl. Instrum. Meth.*, A499:679, 2003.

[33] E. Beuville et al. A low noise amplifier-shaper with tail correction for the STAR detector. *IEEE Transactions on Nuclear Science*, 43:1619, 1996.

[34] F.S. Bieser et al. The STAR trigger. *Nucl. Instrum. Meth.*, A499:766, 2003.

[35] C. Adler et al. The RHIC zero degree calorimeters. *Nucl. Instrum. Meth.*, A470:488–499, 2001.

[36] N.G. Kampen. *Stochastic processes in physics and chemistry.* North-Holland Personal Library, 1992.

[37] R. Bracewell. *The Autocorrelation Function. The Fourier Transform and Its Applications.* New York: McGraw-Hill, 1999.

[38] M. Gazdzicki and S. Mrowczynski. A method to study 'equilibration' in nucleus-nucleus collisions. *Z. Phys*, C54:127–132, 1992.

[39] T.A. Trainor. Event-by-Event Analysis and the Central Limit Theorem. hep-ph/0001148.

[40] M. Gazdzicki and S. Mrowczynski. Event-by-event fluctuations in collective quantities. *Phys. Rev. C*, 60:024901, 1999. nucl-th/9903060.

[41] J. Adams et al. (STAR collaboration). Event-by-event $< p >$ fluctuation in Au-Au collisions at $\sqrt{s_{NN}} = 130$ GeV. nucl-ex/0308033.

[42] J.G. Reid. *Event-by-event Analysis Methods and Applications to Relativistic Heavy-ion Collision Data.* PhD thesis, University of Washington, 2002. nucl-ex/0302001.

[43] C. Adler et al. (STAR collaboration). Disappearance of back-to-back high-p_t hadron correlations in central Au+Au collisions at $\sqrt{s_{NN}}$=200 GeV. *Phys. Rev. Lett.*, 90:082302, 2003.

[44] P. Langevin. *An introduction to stochastic processes in physics containing: On the theory of Brownian motion.* Johns Hopkins University Press, 2002.

[45] A. Lavagno W.M. Alberico and P. Quarati. Nonextensive statistics, fluctuations and correlations in high energy nuclear collisions. *Eur. Phys. J. C*, C12:499–506, 2000. nucl-th/9902070.

[46] C. Bromberg et al. Rapidity correlations in $p-p$ collisions at 102 and 400 GeV/c. *Phys. Rev. D*, 15:1215–1221, 1977.

[47] B.Y. Oh et al. Two particle correlations in the central region of pp and π^-p, interactions at 100-300 GeV/c. *Phys. Lett.*, 56B:400–404, 1975.

[48] H. Braun et al. Charge structure and correlation features in pn multiparticle final states at 195 GeV/c. *Phys. Rev. D*, 17:1260–1267, 1978.

[49] S.R. Amendolia et al. Measurement of two-particle semi-inclusive rapidity distributions at the CERN ISR. *Nuovo Cimento*, 31 A:17–53, 1976.

[50] S.R. Amendolia et al. Measurement of inclusive two-particle rapidity correlations at the isr. *Phys. Lett.*, 48 B:359, 1973.

[51] M. Pratap et al. Azimuthal correlations in pp interactions at 205 GeV/c. *Phys. Rev. Lett.*, 33:797–801, 1974.

[52] T. Kafka et al. One-, two-, and three-particle distributions in pp collisions at 205 GeV/c. *Phys. Rev. D*, 16:1261–1293, 1977.

[53] L.J. simić et al. Two-particle azimuthal correlations in light nuclei collisions at 4.2 GeV/c per nucleon. *Phys. Rev. C*, 45:2417–2422, 1992.

[54] J. Barrete et al. Two charged particle and transverse energy correlations in $Si + Pb$ collisions at 14.6A GeV/c. *Phys. Rev. C*, 49,3:1669–1683, 1994.

[55] G. Ingelman B. Andersson, G. Gustafson and T. Sjostrand. Parton fragmentation and string dynamics. *Physics Reports*, 97:31, 1983.

[56] R. Slansky. Correlations, short-range order and clustering. *Nuclear Physics B*, 73:477–496, 1974.

[57] K.H. Ackermann et al. (STAR collaboration). Elliptic flow in Au+Au collisions at $\sqrt{s_{NN}} = 130$ GeV/c. *Phys. Rev. Lett.*, 86:402, 2001.

[58] C. Adler et al. (STAR collaboration). Elliptic flow from two- and four-particle correlations in Au+Au collisions at $\sqrt{s_{NN}} = 130$ GeV/c. *Phys. Rev. C*, 66:034904, 2002.

[59] S.S. Adler et al. (PHENIX collaboration). Elliptic flow of identified hadrons in Au+Au collisions at $\sqrt{(s_{NN})} = 200$ GeV. *Phys. Rev. Lett.*, 91:182301, 2003.

[60] B.B. Back et al. (PHOBOS collaboration). Pseudorapidity and centrality dependence of the collective flow of charged particles in Au+Au collisions at $\sqrt{(s_{NN})} = 130$ GeV. *Phys. Rev. Lett.*, 89:222301, 2002.

[61] E.V. Shuryak D. Teaney, J. Lauret. Hydro+cascade, flow, the equation of state, predictions and data. *Nucl. Phys.*, A698:479–482, 2002. nucl-th/0104041.

[62] G. Arnison et al. First observation of correlations between high transverse momentum charged particles in events from the cern proton anti-proton collider. *Phys. Lett. B*, 118:173, 1982.

[63] C. Adler et al. (STAR collaboration). Centrality dependence of high p_t hadron suppression in Au+Au collisions at $\sqrt{s_{NN}}$=130 GeV. *Phys. Rev. Lett.*, 89:202301, 2002.

[64] K. Adcox et al. (PHENIX collaboration). Suppression of hadrons with large transverse momentum in central Au + Au collisions at $\sqrt{s_{NN}}$=130 GeV. *Phys. Rev. Lett.*, 88:022301, 2002.

[65] M. Gyulassy and M. Plümer. Jet quenching in dense matter. *Phys. Lett.*, B243:432, 1990.

[66] X.N. Wang and M. Gyulassy. Gluon shadowing and jet quenching in A + A collisions at $s^{1/2}$ = 200-GeV. *Phys. Rev. Lett.*, 68:1480, 1992.

[67] R. Baier et al. Induced gluon radiation in a QCD medium. *Phys. Lett.*, B345:277, 1995.

[68] C. Adler et al. (STAR collaboration). Multiplicity distribution and spectra of negatively charge hadrons in Au+Au collisions at $\sqrt{s_{NN}}$=130 GeV. *Phys. Rev. Lett.*, 87:112303, 2001.

[69] Manuel Calderon de la Barca Sanchez. *Charged Hadron Spectra in Au-Au Collisions at $\sqrt{s_{NN}}$ = 130 GeV*. PhD thesis, Yale University, 2001.

[70] J.G. Reid and T.A. Trainor. Statistical fluctuations and pair mixing in two-point correlation analysis. *Nucl. Instrum. Meth.*, A 457(2):378–383, 2001.

[71] T. Anticic et al. (NA49 Collaboration). Transverse momentum fluctuations in nuclear collisions at 158-A-GEV. hep-ex/0311009.

[72] R.M. Weiner. *Introduction to Bose-Einstein correlations and subatomic interferometry.* JOHN WILEY & SONS, LTD, 2000.

[73] C. Adler et al. (STAR collaboration). Pion interferometry of $\sqrt{(}s_{NN}) =$ 130 GeV Au+Au collisions at RHIC. *Phys. Rev. Lett.*, 87:082301, 2001.

[74] R.L. Ray. Monte Carlo Estimates of HBT, Coulomb and Two-Track Merging and Crossing Contributions to $\Delta\sigma_{p_T}$.

[75] K. Adcox et al. (PHENIX collaboration). Event-by-event fluctuations in mean p_t and e_t in $\sqrt{s_{NN}} = 130$ GeV Au+Au collisions. *Phys. Rev. C*, 66:024901, 2002. nucl-ex/0203015.

[76] S.S. Adler et al. (PHENIX collaboration). Measurement of non-random event-by-event average transverse momentum fluctuations in $\sqrt{s_{NN}} =$ 200 GeV Au+Au collisions. *Phys. Rev. Lett.*, 93:092301, 2004. nucl-ex/031005.

[77] I.G. Bearden et al. (NA44 collaboration). Collective expansion in high energy heavy ion collisions. *Phys. Rev. Lett.*, 78:2080, 1997.

[78] T.A. Trainor (University of Washington) from the Hijing simulation study, private communication.

[79] R.J. Porter (STAR collaboration). *Bull. Am. Phys. Soc.*, 48:25, 2003.

[80] L. Urban, 1993. in GEANT3 writeup, section PHYS-211, Cern Program Library.

[81] Lanny Ray. Monte Carlo Estimates of $e^{\pm}$ contamination contributions to $\Delta\sigma p_T$.

[82] R.L. Ray. Monte Carlo Estimates of Resonance Contributions to $\Delta\sigma p_T$.

[83] G. Roland M. Gaździcki, A. Leonidov. *Eur. Phys. J*, C6:365, 1999.

[84] D.H. Perkins. *Introduction to High Energy Physics.* Addison Wesley, 3rd edition, 1987.

[85] E. Vanmarcke. *Random Fields: Analysis and Synthesis.* The MIT Press, 1992.

[86] M. Gazdzicki and S. Mrowczynski. The distribution function of the event-by-event average p_t for statistically independent emission. *Phys. Lett.*, B498:29–34, 2001.

[87] G. Wilk and Z. Włodarczyk. Interpretation of the nonextensivity parameter q in some applications of Tsallis statistics and Lévy distributions. *Phys. Rev. Lett.*, 84,13:2770–2773, 2000.

[88] P.F. Kolb. Hydrodynamic flow at RHIC. *Heavy Ion Phys.*, 15:279–289, 2002. nucl-th/0104089.

[89] R.L. Ray. Monte Carlo Estimates of Resonance Contributions to $\Delta\sigma p_T$.

Vita

Aya Ishihara was born in Fujinomiya-city, Shizuoka, Japan on September 12, 1974, the daughter of Keiko Ishihara and Takashi Ishihara. After completing her study at Jiyunomori High School, Hanno-city, Saitama, Japan in 1993 she entered Science University of Tokyo in 1994. She received the degree of Bachelor of Science in Physics from Science University of Tokyo in March, 1998. She started her continued study in physics enrolling in the program of the Graduate School of the University of Texas at Austin in August, 1998.

Permanent address: 21-10-601 Inari-cho,
Hanno, Saitama 357-0037, Japan

This dissertation was typeset with LaTeX[†] by the author.

[†]LaTeX is a document preparation system developed by Leslie Lamport as a special version of Donald Knuth's TeX Program.